



Universiteit  
Leiden  
The Netherlands

## **Influence of the electrode-electrolyte interface on electrochemical CO<sub>2</sub> reduction reaction and hydrogen evolution reaction**

Ye, C.

### **Citation**

Ye, C. (2024, December 5). *Influence of the electrode-electrolyte interface on electrochemical CO<sub>2</sub> reduction reaction and hydrogen evolution reaction*. Retrieved from <https://hdl.handle.net/1887/4170871>

Version: Publisher's Version

License: [Licence agreement concerning inclusion of doctoral thesis in the Institutional Repository of the University of Leiden](#)

Downloaded from: <https://hdl.handle.net/1887/4170871>

**Note:** To cite this publication please use the final published version (if applicable).

# **Influence of the Electrode-Electrolyte Interface on Electrochemical CO<sub>2</sub> Reduction Reaction and Hydrogen Evolution Reaction**

Proefschrift

ter verkrijging van

de graad van doctor aan de Universiteit Leiden,  
op gezag van rector magnificus prof.dr.ir. H. Bijl,  
volgens besluit van het college voor promoties  
te verdedigen op donderdag 5 december 2024

klokke 11.30 uur

door

**Chunmiao Ye**

geboren te Anhui

in 1992

**Promotor:** Prof. Dr. M.T.M. Koper

**Co-promotor:** Dr. K.J.P. Schouten (Teijin Limited)

**Promotiecommissie:** Prof. Dr. M. Ubbink

Prof. Dr. K. Tschulik (Ruhr University Bochum)

Dr. R. Kortlever (Delft University of Technology)

Prof. Dr. L.J.C. Jeuken

Dr. R.V. Mom

The work presented in this thesis was supported by the European Commission, as part of the Marie Skłodowska Curie Innovative Training Network ELCOREL-722614.



*Remember to look up at the stars and not down at your feet*

*Stefan Hawking*



# Table of Contents

<b>Chapter 1 Introduction</b>	1
1.1 General Introduction	2
1.2 Electrochemical CO <sub>2</sub> Reduction Reaction	4
1.3 Hydrogen Evolution Reaction (HER)	7
1.4 Outline of This Thesis	8
 <b>Chapter 2 Enhanced Electrochemical CO<sub>2</sub> Reduction to Formate on Poly(4-vinylpyridine)-modified Copper and Gold Electrodes</b>	15
2.1 Introduction	17
2.2 Experimental Section	19
2.3 Results and Discussion	21
2.4 Conclusions	32
 <b>Chapter 3 Influence of Cations on HCOOH and CO Formation during CO<sub>2</sub> Reduction on a Pd<sub>ML</sub>Pt(111) Electrode</b>	39
3.1 Introduction	41
3.2 Experimental Section	43
3.3 Results and Discussion	47
3.4 Conclusions	59
 <b>Chapter 4 The Role of Cations in Hydrogen Evolution Reaction on a Platinum Electrode in Mildly Acidic Media</b>	65
4.1 Introduction	67
4.2 Experimental Section	69
4.3 Results and Discussion	71
4.4 Conclusions	77

<b>Chapter 5 Electrolyte Effect on the Electrochemical CO<sub>2</sub> Reduction on Copper Gas Diffusion Electrodes.....</b>	<b>81</b>
5.1 Introduction .....	83
5.2 Experimental Section .....	84
5.3 Results and Discussion.....	86
5.4 Conclusions .....	94
 <b>Appendices</b>	
<b>A</b> Supplementary Information for Chapter 2 .....	<b>99</b>
<b>B</b> Supplementary Information for Chapter 3 .....	<b>107</b>
<b>C</b> Supplementary Information for Chapter 4 .....	<b>119</b>
<b>D</b> Supplementary Information for Chapter 5 .....	<b>125</b>
 <b>Summary and Outlook.....</b>	 <b>129</b>
<b>Samenvatting en vooruitzicht.....</b>	<b>132</b>
<b>List of Publications .....</b>	<b>135</b>
<b>Curriculum vitae .....</b>	<b>136</b>
<b>Acknowledgements .....</b>	<b>137</b>

# **Chapter 1**

## **Introduction**



## 1.1 General Introduction

The imperative transition toward renewable energy is both a contemporary obligation and an enduring journey that traces its urgency to the historical industrial reliance on fossil fuels. This shift is driven by increasing global awareness of climate change, aggravated by excessive CO<sub>2</sub> emissions resulting from industrial activities. Since the beginning of the industrial era, CO<sub>2</sub> emissions have dramatically increased, leading to considerable environmental disruptions. This has prompted a global shift towards renewable energy sources that are less detrimental to our planet. Anchored by a global commitment to achieve carbon neutrality, underscored by key climate agreements such as the Kyoto Protocol and the Paris Agreement, this shift highlights the global imperative to achieve carbon neutrality within specified timelines.

Given the achievement of low-cost electricity from renewable sources like solar and wind, electrochemistry emerges as a pivotal element in this global energy transition. It is directed to a transformation of electrical energy into chemical bonds and vice versa, promoting the development of modern energy storage and conversion technologies. Ever since Galvani's discovery of "animal electricity" and Volta's pioneering battery, numerous innovations have emerged in the field of electrochemistry, pacing the rhythm of progress across centuries. A key milestone in this journey is the launch of the lithium-ion battery technology, recognized by the 2019 Nobel Prize in Chemistry. This breakthrough marked the beginning of a new era in portable electronics, electric vehicles, and efficient storage for renewable energies, thus foregrounding electrochemistry's vital role in moving towards a fossil fuel-free future.

Over the past decades, electrochemically converting carbon dioxide (CO<sub>2</sub>) into fuels, chemicals and building materials has drawn substantial attention as a strategy to "close the carbon cycle". Such a cycle is shown in Figure 1.1. By utilizing renewable electricity, this process reduces the CO<sub>2</sub>, a byproduct of industrial activities, to value-added products. If these value-added products replace fossil resources, it could indeed close the carbon cycle. Up to now, the achievements in electrochemical CO<sub>2</sub> reduction (CO<sub>2</sub>RR) have been notable,

including the successful conversion of CO<sub>2</sub> into a wide array of products, from simple molecules like carbon monoxide and formic acid to more complex multi-carbon products.<sup>1</sup> These successes demonstrate the feasibility of using CO<sub>2</sub> as a feedstock for renewable fuel and chemical production.

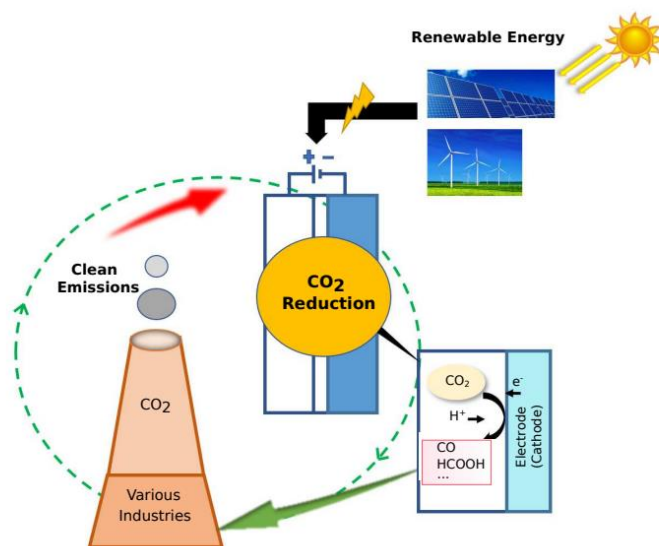


**Figure 1.1** Schematic overview of a carbon neutral cycle including the electrochemical CO<sub>2</sub> reduction reaction<sup>2</sup>

Despite these achievements, the CO<sub>2</sub>RR confronts numerous technical challenges that hinder its application on an industrial scale, including low selectivity and activity for desired products, the rapid deterioration of electrocatalysts, and low overall energy efficiency.<sup>1</sup> Therefore, the future of CO<sub>2</sub>RR rests on overcoming these technical challenges that currently limit its scalability and economic viability. This includes the developments of more efficient and selective electrocatalysts, improved understanding of reaction mechanisms, and the engineering of electrolyzers to optimize CO<sub>2</sub>RR performance. This thesis will concentrate on these challenges and explore how to optimize CO<sub>2</sub>RR performance from different aspects. In this chapter, we will first introduce some general concepts associated with the CO<sub>2</sub>RR.

## 1.2 Electrochemical CO<sub>2</sub> Reduction Reaction

The device that enables the electrochemical conversion of CO<sub>2</sub> is known as an electrolyzer, which utilizes electricity to drive a chemical reaction that would not occur spontaneously under standard conditions. Figure 1.2 illustrates a typical electrolyzer comprising a cathode and an anode submerged in an electrolyte, an electrically conducting medium containing cations and anions.<sup>3</sup> A separator, typically a membrane, may be placed between the cathode and the anode. This membrane selectively permits species to move from one electrolyte compartment to another, thereby preventing secondary reactions and separate the products generated at the two different compartments. Prior to the CO<sub>2</sub>RR, CO<sub>2</sub> is supplied to the electrolyzer, such as by dissolving it in the electrolyte, or by supplying it through the gas phase in a so-called gas diffusion electrode (GDE). Upon application of an electric potential between the cathode and the anode, electrons are provided to the cathode, while a positive charge is generated on the anode by extraction of electrons. At both electrodes, if the driving electrical energy is higher than the reaction activation energy barrier, the electrical energy is converted into chemical energy. As depicted in Figure 1.2, electron transfer at the cathode initiates an electrochemical CO<sub>2</sub> reduction reaction (Equation 1.1), whereas the electron extraction at the anode results in an electrochemical oxidation of H<sub>2</sub>O to oxygen (Equation 1.2). Simultaneously, ions in the electrolyte migrate between the cathode and the anode to balance the transfer of charges at both electrodes, thereby completing the electric circuit.

Despite the great potential of CO<sub>2</sub>RR to generate fuels and chemicals, the processes at electrodes remain kinetically limited for multi-charge transfer reactions.<sup>4</sup> To address this limitation, the introduction of an electrocatalyst is essential. In the field of electrochemistry, electrocatalysts are a specific form of catalysts that function at electrode surfaces or, most commonly, may be the electrode surface itself, which can accelerate the transfer of electrons between electrode and reactants, and/or facilitate to an intermediate chemical transformation described by an overall half-reaction. Therefore, electrocatalyzing CO<sub>2</sub> reduction is directed to chemical reactions happening at the electrode-electrolyte interface.<sup>5</sup>

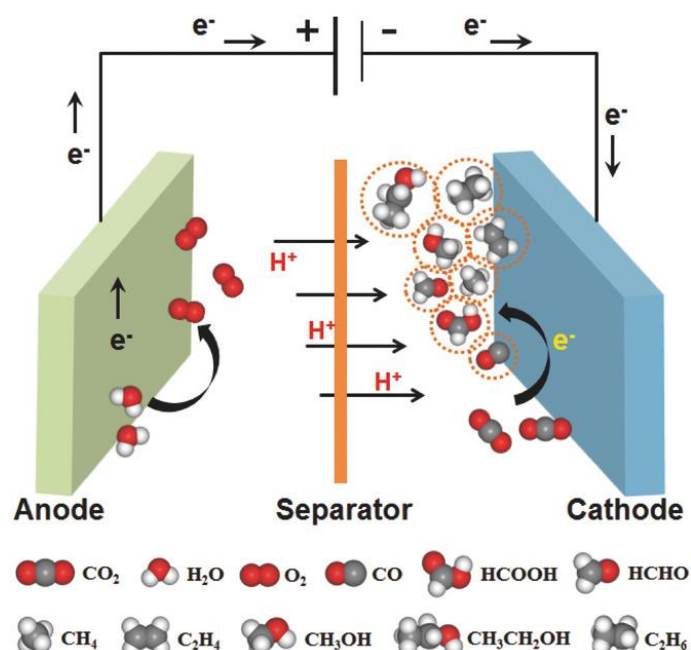
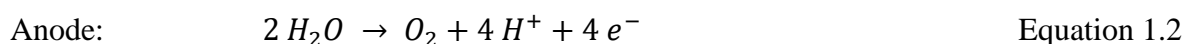
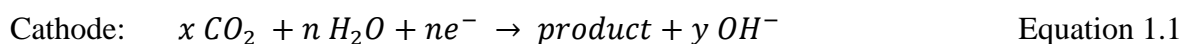


**Figure 1.2** Schematic overview of a CO<sub>2</sub> electrolyzer<sup>3</sup>

Extensive experimental and theoretical work has been dedicated to develop efficient electrocatalysts for CO<sub>2</sub>RR.<sup>1, 6-17</sup> Among these, metal-based electrocatalysts have been extensively studied due to their superior catalytic performance. The nature of the metal catalysts has an important effect on the activity and selectivity of CO<sub>2</sub>RR.<sup>6-8, 10, 12-13</sup> For instance, of the monometallic catalysts, Cu exhibits a unique selectivity to methane and various multi-carbon products such as ethylene, ethanol, and propanol.<sup>8, 12</sup> Precious metal catalysts such as Au and Ag show high selectivity toward CO.<sup>6-7</sup> Platinum group metals are also selective for CO formation but are affected by CO surface poisoning.<sup>14-17</sup> Pd-based catalysts can reach a Faradaic efficiency of 95% for CO generation at negative potentials (-0.8 V<sub>RHE</sub>),<sup>15</sup> while delivering a high Faradaic efficiency toward HCOOH (close to 99%) with a small overpotential of 0.1 V<sup>14</sup>. In addition, other factors, such as surface structure, surface morphology as well as catalyst particle size, are also crucial to the performance of the electrocatalyst for CO<sub>2</sub>RR. Up to now, many approaches including alloying, nanostructuring

as well as functionalization by organic additives, have been employed to the rational design of robust, active, and selective electrocatalysts for CO<sub>2</sub>RR.<sup>1</sup>

In addition to the electrocatalysts, electrolyte composition including cation identity, anion identity, electrolyte pH and buffer capacity have been shown to have a strong impact on the CO<sub>2</sub>RR activity and selectivity.<sup>1</sup> Earlier studies show metal cations in the electrolyte affect the electrode-electrolyte interface by modification of the local electric field, buffering of the interfacial pH or stabilization of reaction intermediates, thereby influencing the selectivity and activity of CO<sub>2</sub>RR.<sup>18-20</sup> For instance, Singh et al. propose that cations affect the CO<sub>2</sub>RR by buffering of the interfacial pH,<sup>19</sup> which is in agreement with the result of pH measurement at a gold–electrolyte interface using attenuated total reflection surface-enhanced infrared spectroscopy based on the ratio between the integrated intensity of the CO<sub>2</sub> and HCO<sub>3</sub><sup>−</sup> bands, showing that larger cations are better buffers and lead to lower pH changes at the interface.<sup>21</sup> Electrolyte pH as well as buffer capacity impacts the local dynamic equilibria of CO<sub>2</sub> (aq.) as well as other reacting species (H<sub>3</sub>O<sup>+</sup>, HCO<sub>3</sub><sup>−</sup> and H<sub>2</sub>O) near the electrode-interface,<sup>22</sup> and thereby influencing the CO<sub>2</sub>RR performance. For example, ethylene formation with high selectivity (70% faradaic efficiency) can be achieved by operating the CO<sub>2</sub>RR in an alkaline electrolyte.<sup>23</sup>

Recent efforts have shifted toward the engineering of the electrolyzer itself to improve the activity and efficiency of CO<sub>2</sub>RR.<sup>23-24</sup> In a traditional CO<sub>2</sub> electrolyzer, a known limitation is the low solubility of CO<sub>2</sub> in the electrolyte, especially in aqueous media, and consequently the low concentration of CO<sub>2</sub> at the electrode-electrolyte interface. This limitation can be overcome by utilizing a flow cell equipped with a GDE. The flow cell enables continuously electrolyte supply across the electrode surface and the porous structure of the GDE allows continuous CO<sub>2</sub> supply from the gas phase to the catalyst-electrolyte interface, therefore greatly improving local CO<sub>2</sub> concentration near the electrode during CO<sub>2</sub>RR and enabling high current densities (e.g. greater than 200 mA cm<sup>−2</sup>) even at ambient conditions.<sup>24-29</sup> However, stability of the GDE remains an issue. Rapid electrode degradation was observed in highly alkaline electrolyte,<sup>27, 30</sup> with one of the degradation mechanisms being carbonate

precipitation resulting from the reaction between  $\text{CO}_2$  and  $\text{KOH}$ .<sup>30-32</sup> To overcome this shortcoming, recently acidic electrolytes have been employed in  $\text{CO}_2\text{RR}$  electrolyzers.<sup>25, 33</sup> With the fast kinetics of proton reduction, rational design of the electrolyte/electrode interface becomes extremely important to achieve a good  $\text{CO}_2\text{RR}$  performance.

### 1.3 Hydrogen Evolution Reaction (HER)

The hydrogen evolution reaction is an electrochemical process that generates hydrogen ( $\text{H}_2$ ) from protons, water, or other proton sources. It serves not only as a half reaction in water electrolysis but also as a competing side reaction during  $\text{CO}_2\text{RR}$ . Therefore, understanding HER is fundamentally important for the development of both water and  $\text{CO}_2\text{RR}$  electrolyzers, which both play significant roles in the energy transition towards a fossil fuel-free future.

Extensive work has been dedicated to gain mechanistic insights of the HER process.<sup>18, 34-45</sup> Traditionally, the significant variations in HER rates observed across different electrodes have been correlated to differences in the free energy of hydrogen adsorption.<sup>46-47</sup> However, this adsorption energy-based descriptor fails to describe the sluggish kinetics of HER in alkaline media and does not accurately reflect the influence of electrochemical environment at the electrode-electrolyte interface on HER under these conditions,<sup>41, 48</sup> where water dissociation is a prerequisite for generating adsorbed hydrogen. As a result, other descriptors such as the interfacial field strength, the oxophilicity of the surface sites and the cation solvation energy have been identified. These descriptors contribute to a more comprehensive understanding of the HER mechanism under alkaline conditions.<sup>35, 38, 40, 49-50</sup> Among these descriptors, the interfacial electric field is recognized as an important factor due to its impact on both the structure and composition of the electric double layer, thereby affecting the electrode-electrolyte interface in multiple manners.<sup>38</sup> Nonetheless, the specific role of the interfacial electric field in tuning the HER activity remains elusive. Therefore, further studies are necessary to gain a deeper understanding of the activity trend and reaction mechanisms of HER.

## 1.4 Outline of This Thesis

The goal of this thesis is to understand how interfacial parameters, such as the addition of organic additives, bulk pH or metal cations of the electrolyte, affect the relevant electrocatalytic reactions, i.e. electrochemical CO<sub>2</sub> reduction reaction or hydrogen evolution reaction. In the following chapters, we will present in-depth studies on the role of these interfacial parameters in tuning CO<sub>2</sub>RR and HER under practical reaction conditions. Our study provides more fundamental insights of CO<sub>2</sub>RR and offers guidelines to optimize CO<sub>2</sub>RR performance for further industrial application of CO<sub>2</sub>RR.

In chapter 2, we first investigate the influence of organic additives on CO<sub>2</sub>RR activity and selectivity and explore how organic additives impact the interfacial environments during CO<sub>2</sub>RR. We show improved selectivity and activity of CO<sub>2</sub>RR towards formic acid production on poly(4-vinylpyridine) (P4VP) modified copper and gold electrodes. By using in situ ATR-SEIRAS and contact angle measurements, we attribute the altered selectivity towards formic acid over CO on both copper and gold electrodes to the hydrophobic nature of P4VP, which influences mass transport dynamics at the electrode-electrolyte interface and thereby promotes a surface hydride mechanism leading to an improved formic acid production.

In chapter 3, we closely examine the role of metal cations on CO<sub>2</sub>RR on a well-defined surface, a palladium monolayer modified Pt(111) surface (Pd<sub>ML</sub>Pt(111)), in a pH 3 electrolyte. We show the onset potential for formic acid and carbon monoxide formation shift positively with the increasing cation concentrations, with a stronger effect observed on HCOOH formation. Density functional theory simulations indicate that cations facilitate both hydride formation and CO<sub>2</sub> activation by polarizing the electronic density at the surface and stabilizing \*CO<sub>2</sub><sup>-</sup>. The simulations further suggest that high CO coverage prevents the formation of hydrides, leading to the quick decrease of HCOOH selectivity at high applied potentials. The result highlights the crucial importance of cations and the overall microenvironment design in CO<sub>2</sub>RR.

Understanding the competing HER is relevant for optimize CO<sub>2</sub>RR performance. Therefore, in chapter 4, we further study the role of metal cations on HER in pH 3 electrolytes. We show that on a polycrystalline Pt surface, while cations do not kinetically influence proton reduction at low potentials, an increase in cation concentration notably enhances water reduction, suggesting the promotional effect of cations on water dissociation. In addition, we identify a non-negligible migration current under mass transport limited conditions in electrolytes with low cation concentration. To minimize this migration current component, electrolytes with sufficient conducting cations and anions are required. We thereby employ electrolytes with mixtures of Li<sup>+</sup> and K<sup>+</sup> cations to explore specific cation-promotion effects on HER, showing that adding strongly hydrated cations (Li<sup>+</sup>) to a K<sup>+</sup>-containing electrolyte leads to a less negative onset potential of water reduction. Interfacial pH measurements show that the interfacial pH at the platinum electrode, at potential where water reduction occurs, remains consistent across different cationic electrolytes. This result indicates that the variation in the onset potential of water reduction across different cationic electrolytes does not result from interfacial pH effect caused by cation hydrolysis near the electrode. Based on these findings, we propose that this difference arises from the more favorable promotion of water dissociation by strongly hydrated cations (Li<sup>+</sup>) compared to weakly hydrated cations (K<sup>+</sup>) under our experimental conditions. Our results hint at the potential benefits of utilizing weakly hydrated cations (K<sup>+</sup>) for CO<sub>2</sub>RR on Pt based catalysts in mild acidic media, offering valuable insights for catalyst-electrolyte design in renewable energy technologies.

In chapter 5, we expand the study on CO<sub>2</sub>RR under more industrially relevant conditions. Specifically, we investigate the influence of bulk electrolyte pH on CO<sub>2</sub>RR product distribution using a copper gas diffusion electrode (Cu GDE) in both a traditional bicarbonate electrolyte and a mildly acidic electrolyte. We observe inhibited hydrogen formation in the mildly acidic electrolyte at low current densities, while the CO<sub>2</sub>RR product distribution remains consistent in both electrolytes at high current densities. In addition, SEM images, along with EDX elemental mapping, indicate a less stable catalyst layer on the Cu GDE, resulting in electrode degradation over long electrolysis in acidic media compared to the bicarbonate electrolyte. Our findings highlight the positive prospects of acidic media in the



field of CO<sub>2</sub>RR, while also indicating new challenges of employing acidic media in CO<sub>2</sub>RR electrolyzers.

## References

1. Stephens, I. E. L.; Chan, K.; Bagger, A.; Boettcher, S. W.; Bonin, J.; Boutin, E.; Buckley, A. K.; Buonsanti, R.; Cave, E. R.; Chang, X.; Chee, S. W.; da Silva, A. H. M.; de Luna, P.; Einsle, O.; Endrődi, B.; Escudero-Escribano, M.; Ferreira de Araujo, J. V.; Figueiredo, M. C.; Hahn, C.; Hansen, K. U.; Haussener, S.; Hunegnaw, S.; Huo, Z.; Hwang, Y. J.; Janáky, C.; Jayathilake, B. S.; Jiao, F.; Jovanov, Z. P.; Karimi, P.; Koper, M. T. M.; Kuhl, K. P.; Lee, W. H.; Liang, Z.; Liu, X.; Ma, S.; Ma, M.; Oh, H.-S.; Robert, M.; Cuenya, B. R.; Rossmeisl, J.; Roy, C.; Ryan, M. P.; Sargent, E. H.; Sebastián-Pascual, P.; Seger, B.; Steier, L.; Strasser, P.; Varela, A. S.; Vos, R. E.; Wang, X.; Xu, B.; Yadegari, H.; Zhou, Y., 2022 roadmap on low temperature electrochemical CO<sub>2</sub> reduction. *Journal of Physics: Energy* **2022**, 4 (4), 042003.
2. Gadgil, N. V. Modeling a Flow-Cell for Electrochemical Reduction of Carbon Dioxide to Formate. M.S. Thesis, Delft University of Technology, 2018.
3. Zhang, W.; Hu, Y.; Ma, L.; Zhu, G.; Wang, Y.; Xue, X.; Chen, R.; Yang, S.; Jin, Z., Progress and Perspective of Electrocatalytic CO<sub>2</sub> Reduction for Renewable Carbonaceous Fuels and Chemicals. *Adv. Sci.* **2018**, 5 (1), 1700275.
4. Oloman, C.; Li, H., Electrochemical processing of carbon dioxide. *ChemSusChem* **2008**, 1 (5), 385-91.
5. Boettcher, S. W.; Oener, S. Z.; Lonergan, M. C.; Surendranath, Y.; Ardo, S.; Brozek, C.; Kempler, P. A., Potentially Confusing: Potentials in Electrochemistry. *ACS Energy Lett.* **2020**, 6 (1), 261-266.
6. Cave, E. R.; Montoya, J. H.; Kuhl, K. P.; Abram, D. N.; Hatsukade, T.; Shi, C.; Hahn, C.; Nørskov, J. K.; Jaramillo, T. F., Electrochemical CO<sub>2</sub> reduction on Au surfaces: mechanistic aspects regarding the formation of major and minor products. *Phys. Chem. Chem. Phys.* **2017**, 19 (24), 15856-15863.
7. Sinha, V.; Khramenkova, E.; Pidko, E. A., Solvent-mediated outer-sphere CO<sub>2</sub> electro-reduction mechanism over the Ag111 surface. *Chem. Sci.* **2022**.
8. Kuhl, K. P.; Cave, E. R.; Abram, D. N.; Jaramillo, T. F., New insights into the electrochemical reduction of carbon dioxide on metallic copper surfaces. *Energy Environ. Sci.* **2012**, 5 (5), 7050-7059.
9. Wuttig, A.; Yaguchi, M.; Motobayashi, K.; Osawa, M.; Surendranath, Y., Inhibited proton transfer enhances Au-catalyzed CO<sub>2</sub>-to-fuels selectivity. *Proc. Natl. Acad. Sci. U.S.A.* **2016**, 113 (32), E4585-93.
10. Hori, Y.; Kikuchi, K.; Suzuki, S., Production of CO and CH<sub>4</sub> in Electrochemical Reduction of CO<sub>2</sub> at Metal Electrodes in Aqueous Hydrogencarbonate Solution. *Chem. Lett.* **1985**, 14 (11), 1695-1698.
11. Vassiliev, Y. B.; Bagotsky, V. S.; Osetrova, N. V.; Khazova, O. A.; Mayorova, N. A., Electroreduction of carbon dioxide: Part I. The mechanism and kinetics of electroreduction of CO<sub>2</sub> in aqueous solutions on metals with high and moderate hydrogen overvoltages. *J. Electroanal. Chem. Interfacial Electrochem.* **1985**, 189 (2), 271-294.
12. Hori, Y.; Kikuchi, K.; Murata, A.; Suzuki, S., Production of Methane and Ethylene in Electrochemical Reduction of Carbon Dioxide at Copper Electrode in Aqueous Hydrogencarbonate Solution. *Chem. Lett.* **1986**, 15 (6), 897-898.
13. Hori, Y.; Murata, A.; Kikuchi, K.; Suzuki, S., Electrochemical reduction of carbon dioxides to carbon monoxide at a gold electrode in aqueous potassium hydrogen carbonate. *J. Chem. Soc., Chem.*

*Commun.* **1987**, (10), 728.

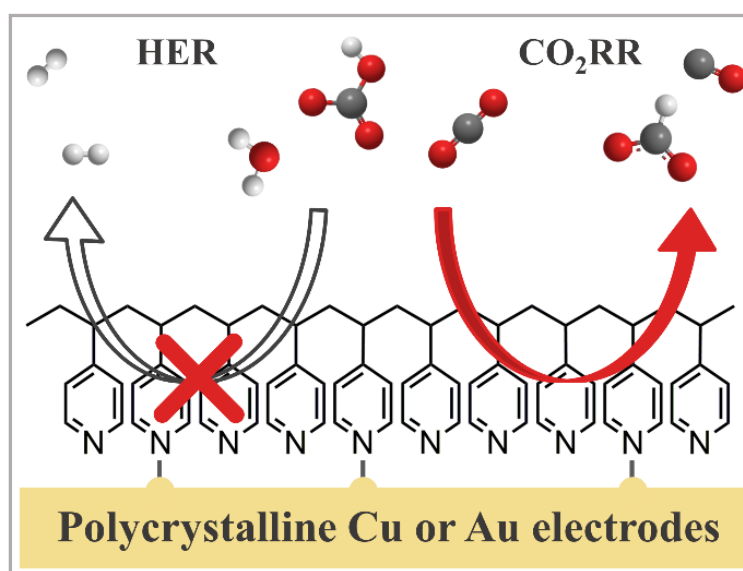
14. Min, X.; Kanan, M. W., Pd-catalyzed electrohydrogenation of carbon dioxide to formate: high mass activity at low overpotential and identification of the deactivation pathway. *J. Am. Chem. Soc.* **2015**, *137* (14), 4701-8.
15. Guo, R.-H.; Liu, C.-F.; Wei, T.-C.; Hu, C.-C., Electrochemical behavior of CO<sub>2</sub> reduction on palladium nanoparticles: Dependence of adsorbed CO on electrode potential. *Electrochem. Commun.* **2017**, *80*, 24-28.
16. Chen, X.-J.; Chen, Y.-M.; Yu, S.; Huang, T.-X.; Xie, S.; Wu, D.-Y.; Tian, Z.-Q., In Situ Spectroscopic Diagnosis of CO<sub>2</sub> Reduction at the Pt Electrode/Pyridine-Containing Electrolyte Interface. *ACS Catal.* **2021**, *11* (17), 10836-10846.
17. Chen, X.; Granda-Marulanda, L. P.; McCrum, I. T.; Koper, M. T. M., How palladium inhibits CO poisoning during electrocatalytic formic acid oxidation and carbon dioxide reduction. *Nat. Commun.* **2022**, *13* (1), 38.
18. Waegle, M. M.; Gunathunge, C. M.; Li, J.; Li, X., How cations affect the electric double layer and the rates and selectivity of electrocatalytic processes. *J. Chem. Phys.* **2019**, *151* (16), 160902.
19. Singh, M. R.; Kwon, Y.; Lum, Y.; Ager, J. W., 3rd; Bell, A. T., Hydrolysis of Electrolyte Cations Enhances the Electrochemical Reduction of CO<sub>2</sub> over Ag and Cu. *J. Am. Chem. Soc.* **2016**, *138* (39), 13006-13012.
20. Goyal, A. Role of near-surface environment in tuning electrochemical CO<sub>2</sub> reduction reaction and H<sub>2</sub> evolution reaction. 2022.
21. Ayemoba, O.; Cuesta, A., Spectroscopic Evidence of Size-Dependent Buffering of Interfacial pH by Cation Hydrolysis during CO<sub>2</sub> Electroreduction. *ACS Appl. Mater. Interfaces* **2017**, *9* (33), 27377-27382.
22. Marcandalli, G.; Villalba, M.; Koper, M. T. M., The Importance of Acid-Base Equilibria in Bicarbonate Electrolytes for CO<sub>2</sub> Electrochemical Reduction and CO Reoxidation Studied on Au(hkl) Electrodes. *Langmuir* **2021**, *37* (18), 5707-5716.
23. Dinh, C. T.; Burdyny, T.; Kibria, M. G.; Seifitokaldani, A.; Gabardo, C. M.; Garcia de Arquer, F. P.; Kiani, A.; Edwards, J. P.; De Luna, P.; Bushuyev, O. S.; Zou, C.; Quintero-Bermudez, R.; Pang, Y.; Sinton, D.; Sargent, E. H., CO<sub>2</sub> electroreduction to ethylene via hydroxide-mediated copper catalysis at an abrupt interface. *Science* **2018**, *360* (6390), 783-787.
24. Burdyny, T.; Smith, W. A., CO<sub>2</sub> reduction on gas-diffusion electrodes and why catalytic performance must be assessed at commercially-relevant conditions. *Energy Environ. Sci.* **2019**, *12* (5), 1442-1453.
25. Monteiro, M. C. O.; Philips, M. F.; Schouten, K. J. P.; Koper, M. T. M., Efficiency and selectivity of CO<sub>2</sub> reduction to CO on gold gas diffusion electrodes in acidic media. *Nat. Commun.* **2021**, *12* (1), 1-7.
26. Philips, M. F.; Gruter, G.-J. M.; Koper, M. T. M.; Schouten, K. J. P., Optimizing the Electrochemical Reduction of CO<sub>2</sub> to Formate: A State-of-the-Art Analysis. *ACS Sustainable Chemistry & Engineering* **2020**, *8* (41), 15430-15444.
27. Zhang, X.; Li, J.; Li, Y. Y.; Jung, Y.; Kuang, Y.; Zhu, G.; Liang, Y.; Dai, H., Selective and High Current CO<sub>2</sub> Electro-Reduction to Multicarbon Products in Near-Neutral KCl Electrolytes. *J. Am. Chem. Soc.* **2021**, *143* (8), 3245-3255.
28. Huang, J. E.; Li, F.; Ozden, A.; Sedighian Rasouli, A.; Garcia de Arquer, F. P.; Liu, S.; Zhang, S.; Luo, M.; Wang, X.; Lum, Y.; Xu, Y.; Bertens, K.; Miao, R. K.; Dinh, C. T.; Sinton, D.; Sargent, E.

- H., CO<sub>2</sub> electrolysis to multicarbon products in strong acid. *Science* **2021**, 372 (6546), 1074-1078.
29. Gu, J.; Liu, S.; Ni, W.; Ren, W.; Haussener, S.; Hu, X., Modulating electric field distribution by alkali cations for CO<sub>2</sub> electroreduction in strongly acidic medium. *Nat. Catal.* **2022**, 5 (4), 268-276.
30. Popović, S.; Smiljanić, M.; Jovanović, P.; Vavra, J.; Buonsanti, R.; Hodnik, N., Stability and degradation mechanisms of copper-based catalysts for electrochemical CO<sub>2</sub> reduction. *Angew. Chem.* **2020**, 132 (35), 14844-14854.
31. Rabinowitz, J. A.; Kanan, M. W., The future of low-temperature carbon dioxide electrolysis depends on solving one basic problem. *Nat. Commun.* **2020**, 11 (1), 5231.
32. Nwabara, U. O.; Cofell, E. R.; Verma, S.; Negro, E.; Kenis, P. J. A., Durable Cathodes and Electrolyzers for the Efficient Aqueous Electrochemical Reduction of CO<sub>2</sub>. *ChemSusChem* **2020**, 13 (5), 855-875.
33. Bondue, C. J.; Graf, M.; Goyal, A.; Koper, M. T. M., Suppression of Hydrogen Evolution in Acidic Electrolytes by Electrochemical CO<sub>2</sub> Reduction. *J. Am. Chem. Soc.* **2021**, 143 (1), 279-285.
34. Sheng, W.; Gasteiger, H. A.; Shao-Horn, Y., Hydrogen Oxidation and Evolution Reaction Kinetics on Platinum: Acid vs Alkaline Electrolytes. *J. Electrochem. Soc.* **2010**, 157 (11), B1529.
35. Subbaraman, R.; Tripkovic, D.; Strmcnik, D.; Chang, K. C.; Uchimura, M.; Paulikas, A. P.; Stamenkovic, V.; Markovic, N. M., Enhancing hydrogen evolution activity in water splitting by tailoring Li(+)-Ni(OH)(2)-Pt interfaces. *Science* **2011**, 334 (6060), 1256-60.
36. Stamenkovic, V. R.; Strmcnik, D.; Lopes, P. P.; Markovic, N. M., Energy and fuels from electrochemical interfaces. *Nat Mater* **2016**, 16 (1), 57-69.
37. Strmcnik, D.; Lopes, P. P.; Genorio, B.; Stamenkovic, V. R.; Markovic, N. M., Design principles for hydrogen evolution reaction catalyst materials. *Nano Energy* **2016**, 29, 29-36.
38. Ledezma-Yanez, I.; Wallace, W. D. Z.; Sebastián-Pascual, P.; Climent, V.; Feliu, J. M.; Koper, M. T. M., Interfacial water reorganization as a pH-dependent descriptor of the hydrogen evolution rate on platinum electrodes. *Nature Energy* **2017**, 2 (4).
39. Lamoureux, P. S.; Singh, A. R.; Chan, K., pH Effects on Hydrogen Evolution and Oxidation over Pt(111): Insights from First-Principles. *ACS Catal.* **2019**, 9 (7), 6194-6201.
40. McCrum, I. T.; Koper, M. T. M., The role of adsorbed hydroxide in hydrogen evolution reaction kinetics on modified platinum. *Nature Energy* **2020**, 5 (11), 891-899.
41. Goyal, A.; Koper, M. T. M., The Interrelated Effect of Cations and Electrolyte pH on the Hydrogen Evolution Reaction on Gold Electrodes in Alkaline Media. *Angew. Chem. Int. Ed. Engl.* **2021**, 60 (24), 13452-13462.
42. Goyal, A.; Koper, M. T. M., Understanding the role of mass transport in tuning the hydrogen evolution kinetics on gold in alkaline media. *J. Chem. Phys.* **2021**, 155 (13), 134705.
43. Huang, B.; Rao, R. R.; You, S.; Hpone Myint, K.; Song, Y.; Wang, Y.; Ding, W.; Giordano, L.; Zhang, Y.; Wang, T.; Muy, S.; Katayama, Y.; Grossman, J. C.; Willard, A. P.; Xu, K.; Jiang, Y.; Shao-Horn, Y., Cation- and pH-Dependent Hydrogen Evolution and Oxidation Reaction Kinetics. *JACS Au* **2021**, 1 (10), 1674-1687.
44. Monteiro, M. C. O.; Goyal, A.; Moerland, P.; Koper, M. T. M., Understanding Cation Trends for Hydrogen Evolution on Platinum and Gold Electrodes in Alkaline Media. *ACS Catal.* **2021**, 11 (23), 14328-14335.
45. Monteiro, M. C. O.; Dattila, F.; Lopez, N.; Koper, M. T. M., The Role of Cation Acidity on the Competition between Hydrogen Evolution and CO<sub>2</sub> Reduction on Gold Electrodes. *J. Am. Chem. Soc.* **2022**, 144 (4), 1589-1602.

46. Pentland, N.; Bockris, J. O. M.; Sheldon, E., Hydrogen Evolution Reaction on Copper, Gold, Molybdenum, Palladium, Rhodium, and Iron: Mechanism and Measurement Technique under High Purity Conditions. *J. Electrochem. Soc.* **1957**, *104* (3), 182.
47. Nørskov, J. K.; Bligaard, T.; Logadottir, A.; Kitchin, J. R.; Chen, J. G.; Pandelov, S.; Stimming, U., Trends in the Exchange Current for Hydrogen Evolution. *J. Electrochem. Soc.* **2005**, *152* (3), J23.
48. Rebollar, L.; Intikhab, S.; Oliveira, N. J.; Yan, Y.; Xu, B.; McCrum, I. T.; Snyder, J. D.; Tang, M. H., “Beyond Adsorption” Descriptors in Hydrogen Electrocatalysis. *ACS Catal.* **2020**, *10* (24), 14747-14762.
49. Rebollar, L.; Intikhab, S.; Snyder, J. D.; Tang, M. H., Kinetic Isotope Effects Quantify pH-Sensitive Water Dynamics at the Pt Electrode Interface. *J. Phys. Chem. Lett.* **2020**, *11* (6), 2308-2313.
50. Subbaraman, R.; Tripkovic, D.; Chang, K. C.; Strmcnik, D.; Paulikas, A. P.; Hirunsit, P.; Chan, M.; Greeley, J.; Stamenkovic, V.; Markovic, N. M., Trends in activity for the water electrolyser reactions on 3d M(Ni,Co,Fe,Mn) hydr(oxy)oxide catalysts. *Nat Mater* **2012**, *11* (6), 550-7.

## Chapter 2

### Enhanced Electrochemical CO<sub>2</sub> Reduction to Formate on Poly(4-vinylpyridine)-modified Copper and Gold Electrodes



This chapter is based on:

Ye, C.; Raaijman, S. J.; Chen, X.; Koper, M. T. M. *ACS Appl. Mater. Interfaces* **2022**, *14* (40), 45263-45271

**Abstract:** Developing active and selective catalysts converting CO<sub>2</sub> to valuable products remains a critical challenge for further application of the electrochemical CO<sub>2</sub> reduction reaction (CO<sub>2</sub>RR). Catalytic tuning with organic additives/films has emerged as a promising strategy to tune CO<sub>2</sub>RR activity and selectivity. Herein we report a facile method to significantly change CO<sub>2</sub>RR selectivity and activity of copper and gold electrodes. We found improved selectivity towards HCOOH at low overpotentials on both polycrystalline Cu and Au electrodes after chemical modification with a poly (4-vinylpyridine) (P4VP) layer. In situ ATR-SEIRAS and contact angle measurements indicate that the hydrophobic nature of the P4VP layer limits mass transport of HCO<sub>3</sub><sup>-</sup> and H<sub>2</sub>O, whereas it has little influence on CO<sub>2</sub> mass transport. Moreover, the early onset of HCOOH formation and the enhanced formation of HCOOH over CO suggests that P4VP modification promotes a surface hydride mechanism for HCOOH formation on both electrodes.

## 2.1 Introduction

The electrochemical CO<sub>2</sub> reduction reaction (CO<sub>2</sub>RR) provides a promising route to utilize carbon feedstock and store renewable electrical energy. Various products, such as formic acid, carbon monoxide, hydrocarbons and alcohols, can be obtained via the CO<sub>2</sub>RR in aqueous media. Extensive experimental and theoretical work has been dedicated to investigate the CO<sub>2</sub>RR process to different products.<sup>1-4</sup> The initial two-electron transfer products formed during the CO<sub>2</sub>RR in aqueous media are formic acid (HCOOH) and carbon monoxide (CO), with subsequent further reduced products commonly agreed upon as resulting from CO reduction (mainly on copper (Cu) catalysts).<sup>5</sup> Due to the high ratio of molecular weight per electron transferred, formic acid has been considered one of the most economically interesting products.<sup>6-7</sup> However, HCOOH-selective catalysts such as Sn, Pb and Pd either require high overpotentials (>0.8 V) or suffer from low stability,<sup>8-10</sup> which limits their application. Therefore, discovering the factors which govern the selectivity of CO<sub>2</sub>RR to HCOOH could open up the possibility of selective HCOOH synthesis from CO<sub>2</sub>RR with higher efficiency.

Despite extensive efforts of the scientific community, achieving high selectivity at low overpotentials remains a significant challenge for the CO<sub>2</sub>RR.<sup>11-14</sup> One strategy to influence product selectivity is catalyst modification with organic additives such as poly (4-vinyl pyridine) (P4VP),<sup>15</sup> N-substituted pyridinium,<sup>16</sup> poly(acrylamide) (PAM),<sup>17</sup> and N,N'-ethylene-phenanthroline dibromide<sup>18</sup>. Coating polycrystalline Cu electrodes with P4VP yields improved formic acid selectivity with maximum faradaic efficiency (FE) of ca. 40%.<sup>15</sup> Polycrystalline Cu electrodes modified with N-substituted pyridinium additives instead produce C<sub>2</sub> and C<sub>3</sub> products with total FE of ca. 70-80% (although these electrodes also show enhanced formic acid formation at low overpotential).<sup>16</sup> Cu surface modification by polyaniline results in similar behavior, improving selectivity towards C<sub>2+</sub> hydrocarbons to ca. 80%.<sup>19</sup> There are two main considerations explaining how additives affect the activity and selectivity of CO<sub>2</sub>RR catalysts: i) by influencing the catalytic activity (by stabilizing/destabilizing reaction intermediates) and/or ii) by changing the local concentration



of interfacial species involved in the reaction.<sup>20-21</sup> To illustrate, a higher CO coverage on polyaniline coated polycrystalline Cu catalysts,<sup>19</sup> an increased local pH for polycrystalline Cu electrodes modified with N-substituted pyridinium additives<sup>16</sup>, and enhanced stabilization of the CO dimer on PAM modified Cu polycrystalline catalysts<sup>17</sup> have been speculated to increase the selectivity towards C<sub>2+</sub> hydrocarbons, whereas the unfavorable H<sub>2</sub>O dissociation and limited mass transport of proton donors (H<sub>2</sub>O and HCO<sub>3</sub><sup>-</sup>) have been proposed to lead to the suppression of the hydrogen evolution reaction (HER) on alkanethiol modified Cu mesh electrodes<sup>22</sup> and cetalkonium chloride modified polycrystalline Sn electrodes<sup>23</sup>. Furthermore, recent computational studies have demonstrated a relation between changes in hydrophobicity resulting from functionalization of a Cu surface with organic molecules, and the tendency to form surface hydrides.<sup>24</sup> In the latter work, it was proposed that hydrophilic interfaces promote the formation of surface hydrides, which enhance the formation of formic acid, while hydrophobic interfaces favor CO formation instead.<sup>24</sup> These proposed explanations on the role of additives were mainly focused on multi-carbon products. More experimental evidence to elucidate the enhanced HCOOH formation is still highly desirable.

To investigate to what extent organic additives affect CO<sub>2</sub>RR activity and selectivity, we studied the CO<sub>2</sub>RR on polycrystalline Cu (poly Cu) and Au (poly Au) electrodes with and without P4VP layer coating, focusing on changes in the catalytic activity and product distribution. In agreement with the literature,<sup>15</sup> we observe an increase in selectivity of CO<sub>2</sub>RR to HCOOH on a P4VP modified polycrystalline Cu (P4VP-modified Cu) electrode. Interestingly, this same effect is also observed on a P4VP-modified polycrystalline Au (P4VP-modified Au) electrode, even though pristine Au is a highly selective catalyst for reducing CO<sub>2</sub> to CO.<sup>25-26</sup> Our results suggest that surface modification with a P4VP layer results in enhanced selectivity towards HCOOH during the CO<sub>2</sub>RR, regardless of the nature of electrocatalysts. To better understand this behavior, we employed in situ Attenuated Total Reflection Surface-Enhanced Infrared Reflection-Adsorption Spectroscopy (ATR-SEIRAS) to investigate the interfacial reaction species during the CO<sub>2</sub>RR on P4VP-modified electrodes. We show that, apart from the interaction between the P4VP layer and the metal catalysts influencing catalysis, organic layer-induced limitations in mass transport of H<sub>2</sub>O and HCO<sub>3</sub><sup>-</sup>

result in a local environment rich in CO<sub>2</sub>, which thereby increases CO<sub>2</sub>RR rate whilst suppressing the HER. Finally, the selective enhancement of HCOOH formation over CO at low overpotentials suggest a surface hydride pathway to HCOOH. Our work thereby offers a more comprehensive understanding of the role of P4VP layer in tuning CO<sub>2</sub>RR activity and selectivity.

## 2.2 Experimental Section

**Cleaning.** Milli-Q water (resistivity > 18.2 MΩ·cm, TOC < 5 ppb) was used for all experiments in this work. Prior to each experiment, all cell compartments were cleaned by soaking in an aqueous solution of 1 g·L<sup>-1</sup> KMnO<sub>4</sub> (Fluka, ACS reagent) and 0.5 M H<sub>2</sub>SO<sub>4</sub> (Fluka, ACS reagent) overnight. The solution was subsequently drained and the cell compartments were rinsed with a dilute piranha solution (1:3 v/v of H<sub>2</sub>O<sub>2</sub> (Merck, Emprove exp) / H<sub>2</sub>SO<sub>4</sub>) to remove residual KMnO<sub>4</sub> and MnOx. Afterwards, the cell compartments were cleaned by repetitively rinsing and boiling with Milli-Q water to remove all inorganic contaminants.

**Electrode preparation.** A polycrystalline Cu disk electrode (Mateck, 99.995%), a polycrystalline Au disk electrode (Mateck, 99.95%) and a pyrolytic graphite disk electrode (PY001009, Graphite Store) were used as working electrodes. Prior to each experiment, working electrodes were mechanically polished with a diamond suspension (MetaDi, 0.5 μm, Buehler) on a microcloth (Buehler), followed by rinsing with Milli-Q water to remove residual diamond suspension. Afterwards, polycrystalline copper and polycrystalline gold electrodes were electropolished as per the following procedures. Polycrystalline copper electrodes were electropolished in a 10:5:2 solution of H<sub>3</sub>PO<sub>4</sub> (Merck, 85%): H<sub>2</sub>O: H<sub>2</sub>SO<sub>4</sub> (Fluka, ACS Reagent) at +3 V vs a graphite electrode for 30 s. Polycrystalline Au electrodes were first oxidized in 0.1 M H<sub>2</sub>SO<sub>4</sub> at +10 V vs the graphite electrode for 20 s and then dipped into 6 M HCl (Merck, ACS reagent, 37%) for 30 s to remove the oxide layer. The obtained eletropolished electrodes were further rinsed with Milli-Q water and dried under compressed air flow. P4VP-modified electrodes were obtained by dropcasting 10 μL of 100 mg mL<sup>-1</sup> P4VP (Aldrich, Mw~60000) in dichloromethane (Actu-all chemicals) solution on

dried polycrystalline Cu and Au disk electrodes, and drying the electrodes in air for 30 minutes until all dichloromethane had evaporated.

**Surface characterization.** All AFM imaging was carried out in air with a JPK NanoWizard 3. A SNL (Bruker, resonance frequency: 65 kHz, spring constant: 0.35 N/m) tip was used. The AFM scan rate was 1 Hz, and the images were taken in tapping mode. All the contact angle measurements were carried out with a contact angle goniometer (Ramé-hart, model 250): 3  $\mu$ L of Milli-Q H<sub>2</sub>O was dropped onto the electrode, and the images were taken within 5 s after H<sub>2</sub>O was dropped on the electrodes. The contact angle measurements were performed three times to confirm the trend, all electrodes were freshly prepared each time.

**Electrochemistry.** All electrochemical experiments were carried out in a H-type electrochemical cell equipped with three electrodes. The cathode and anode were separated by Nafion 117 membrane (Aldrich, thickness: 0.0006 inch). A dimensionally stable anode (Magnet Special Anodes) was used as a counter electrode, and a leakless Ag/AgCl (EDAQ) was used as a reference electrode. All reported potentials were converted to the reversible hydrogen electrode (RHE) scale. All working potentials were controlled with a Bio-logic SP-300 Potentiostat under room temperature. The working electrolyte was an aqueous 0.1 M KHCO<sub>3</sub> solution, made from Milli-Q water and KHCO<sub>3</sub> (Fluka, ACS reagent). Before every CO<sub>2</sub> reduction experiment, CO<sub>2</sub> (Linde, 4.5) was bubbled through the electrolyte for 30 minutes to obtain a CO<sub>2</sub> saturated solution. Blank cyclic voltammograms were first taken to characterize the surface and to stabilize the initial state of the electrode. The ohmic resistance was evaluated by electrochemical impedance spectroscopy (EIS) at 0.1 V vs RHE, and 85% ohmic drop compensation was applied to all subsequent experiments. Electrolysis was performed at fixed potentials for 30 minutes, constantly purging the electrolyte at 8 mL/min CO<sub>2</sub> for a stable pH and continuous CO<sub>2</sub> supply. Gas and liquid samples were taken every 10 minutes. After all experiments, P4VP layer remains intact on both poly Cu and Au electrodes under our working conditions, as evidenced by the cyclic voltammograms of P4VP-modified electrodes after CO<sub>2</sub>RR in Figure A.6.

The gas products from CO<sub>2</sub> reduction were analyzed by a GC-2010 plus system (Shimadzu). The GC system was equipped with two columns. A RTX-1 column (Restek) connected to a FID was used to separate and detect hydrocarbons (CH<sub>4</sub>, C<sub>2</sub>H<sub>4</sub>), and a ShinCarbon ST micropacked 80/100 column (Restek) connected to a TCD was used for H<sub>2</sub> and CO. Liquid products were analyzed via HPLC with an Aminex HPX-87H column (BioRad) equipped with a RID detector (Shimadzu). The detection limit for H<sub>2</sub>, CO and HCOOH was 75 ppm, 10 ppm and 0.1 mM, respectively. Due to low production at low overpotentials and the detection limit of GC and HPLC, experiments were performed three times to ensure the experimental reproducibility. Total FEs of all products with error bars are around 100% at all electrodes, without further normalization.

**In situ ATR-SEIRAS.** A thin layer of poly Cu or Au (ca. 70 nm thickness) was deposited on either a silicon (for Cu) or ZnSe (for Au) prism via magnetron sputtering machine (Leybold, Z-400). The obtained Cu and Au films were used as working electrode during in situ ATR-SEIRAS experiments with an IR spectrometer (Bruker, Vertex 80v). To avoid H<sub>2</sub>O formation from HCO<sub>3</sub><sup>-</sup>, 0.1M KDCO<sub>3</sub> solution was prepared by dissolving 0.05 M K<sub>2</sub>CO<sub>3</sub> in D<sub>2</sub>O and subsequent saturation with CO<sub>2</sub>, which was then used as working electrolyte in all experiments in D<sub>2</sub>O solutions. The background spectra were taken at open circuit potential in H<sub>2</sub>O or D<sub>2</sub>O (sigma, 99.9 atom % D) before each experiment. Afterwards, the working electrolyte was added to the cell. Before CO<sub>2</sub> reduction experiments, cyclic voltammograms were taken in CO<sub>2</sub> saturated solutions to initialize the surface until the spectrum was stable. After that, the sample spectra were taken during LSV from 0.3 V vs RHE to target negative potentials on different working electrode at 1 mV s<sup>-1</sup>. All spectra were taken in absorbance mode by averaging over 200 scans with a 4 cm<sup>-1</sup> resolution.

### 2.3 Results and Discussion

Cyclic voltammetry in aqueous CO<sub>2</sub>-saturated 0.1 M KHCO<sub>3</sub> was used to characterize the initial state of the electrodes. Figure 2.1a shows the cyclic voltammograms of the unmodified poly Cu (black curve) and the P4VP-modified Cu electrodes (red curve), respectively. The poly Cu electrode shows a cyclic voltammogram similar to that reported before,<sup>27-28</sup>

characterized by peaks corresponding to surface oxidation/reduction. The oxidation peak during the positive-going scan is the result of Cu oxide formation ( $\text{Cu}^0 \rightarrow \text{CuO}$ ), while the reduction peaks are associated with the reverse reaction, being  $\text{CuO} \rightarrow \text{Cu}_2\text{O}$  and  $\text{Cu}_2\text{O} \rightarrow \text{Cu}^0$ , respectively, when scanning from positive to negative.<sup>29-30</sup> Much decreased double layer charging current (-0.2 - 0.2 V vs RHE) and oxidation current (0.5 - 0.8 V vs RHE) are observed on the P4VP-modified Cu electrode, implying that fewer Cu sites are electrochemically accessible due to the presence of P4VP layer.

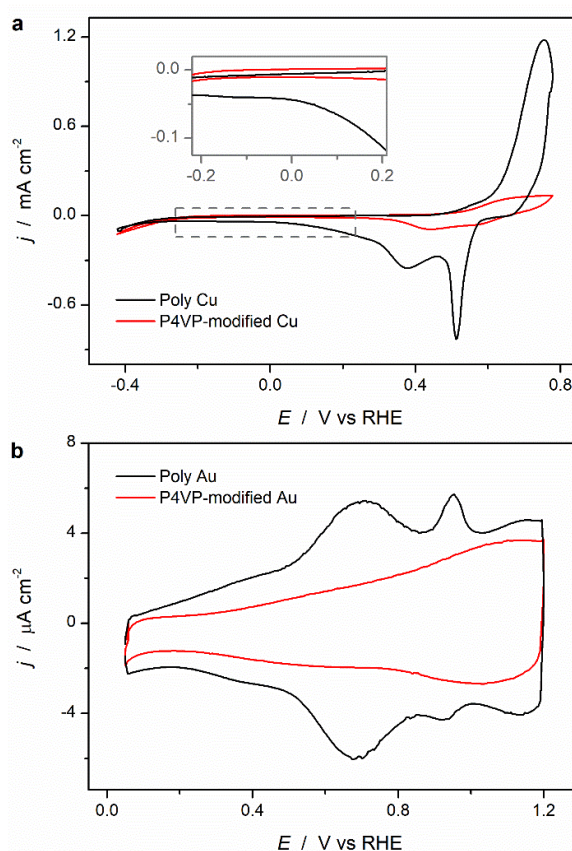


**Figure 2.1** The cyclic voltammograms of (a) poly Cu and (b) poly Au with (red) and without (black) a P4VP layer, measured at 50 mV/s in CO<sub>2</sub> saturated 0.1 M KHCO<sub>3</sub> solution.

Gold was characterized similarly (Figure 2.1b), where the reversible peaks at 0.7 and 0.95 V vs RHE in this case correspond to the electrochemical lifting of the Au (110) and Au (111) surface reconstructions. Although the peaks associated with the lifting of the surface reconstruction of gold have been associated with sulfate adsorption,<sup>31-32</sup> they were also observed in 0.1 M KHCO<sub>3</sub> solutions in a previous work reported by our group.<sup>33</sup> With the

presence of a P4VP layer, these reconstruction-peaks diminish greatly, leaving a broad double layer current, which confirms the decreased permeability of the electrolyte to the reaction interface.

In addition to cyclic voltammetry, AFM was used to characterize the morphology of the electrodes, as depicted in Figure A.1. Figures A.1a, c represent poly Cu and poly Au surfaces respectively, with both electrodes showing typical metallic polycrystalline surfaces with grain boundaries. After modification with P4VP layer, for P4VP-modified Cu (Figure A.1b) and Au electrodes (Figure A.1d), respectively, the morphologies of the surfaces become smoother compared to the uncoated surfaces. This indicates that the P4VP layer fully covers the electrode surfaces, yielding a significant reduction in surface roughness. Additionally, dark spots can be observed in Figures A.1b and d, representing small holes in P4VP film, which confirms previous reports of a P4VP layer adopting a mesoporous structure.<sup>34</sup>

Figure 2.2 depicts the effects on CO<sub>2</sub>RR performance after chemical modification of a polycrystalline Cu surface with a P4VP layer. The partial current densities of the dominant products (H<sub>2</sub>, CO and HCOOH) are shown in Figure 2.2a, with the dashed and solid lines representing unmodified and P4VP-modified Cu electrodes, respectively. Associated FEs (including observed minority products) are depicted in Figures 2.2b and 2.2c, for the unmodified and P4VP-modified Cu electrodes, respectively. Even though other products (ethanol, n-propanol etc.) have been reported as possible products,<sup>1</sup> they were not detected under our working conditions. The total current density of CO<sub>2</sub>RR-related products on P4VP-modified Cu is higher than on unmodified Cu at low overpotentials. This is especially clear at -0.6 V vs RHE, where the combined partial current density of CO<sub>2</sub>RR-related products on the P4VP-modified Cu electrode is almost four times higher than on unmodified Cu. Additionally, at this potential, the current density for H<sub>2</sub> production on the P4VP-modified Cu electrode is a factor of three lower. These results demonstrate that the presence of the P4VP layer promotes the reduction of CO<sub>2</sub> and simultaneously suppresses the HER, especially at low overpotentials. Besides enhancing the total activity of the CO<sub>2</sub>RR, product selectivity is also changed. FEs for HCOOH, CO and H<sub>2</sub> are 13%, 5% and 87%, respectively,

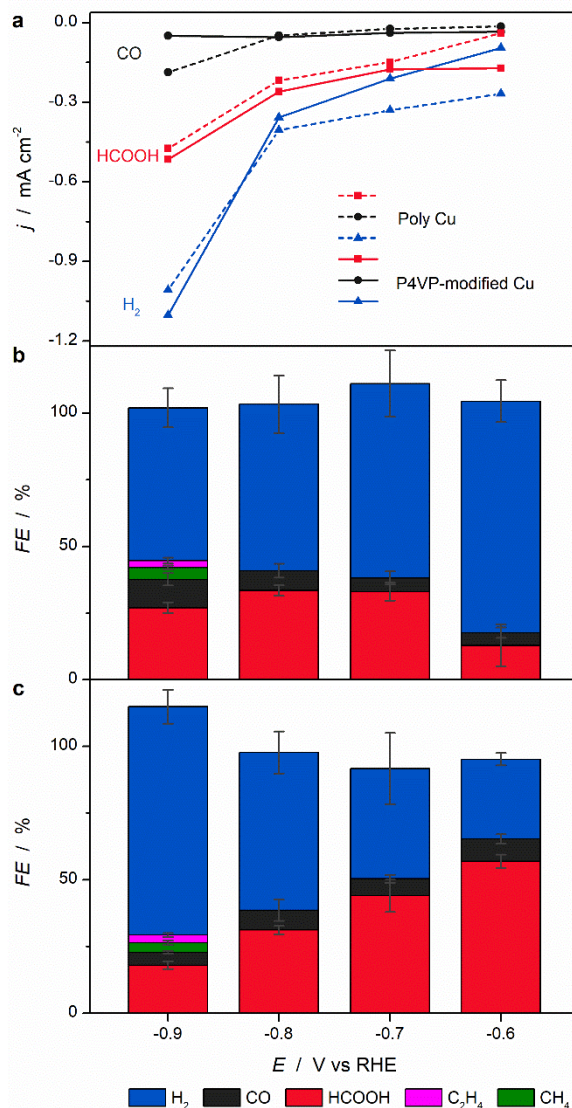


**Figure 2.2** CO<sub>2</sub>RR performance in CO<sub>2</sub> saturated 0.1 M KHCO<sub>3</sub>. (a) Partial current density of H<sub>2</sub>, HCOOH, CO as a function of potential on unmodified Cu (dashed line) and P4VP-modified Cu (solid line), with the FEs for observed products on (b) poly Cu and (c) P4VP-modified Cu. Error bars are standard deviations based on three measurements.

for unmodified Cu at -0.6 V vs RHE, whilst on P4VP-modified Cu, the FEs are 57%, 8% and 33%, respectively, leading to an enhancement factor of 4.4 for HCOOH and 1.6 for CO. The partial current density and FEs for CO<sub>2</sub>RR products (HCOOH and CO) on P4VP-modified Cu remains higher than unmodified electrode at -0.7 V vs RHE. However, at more negative potentials, especially at -0.9 V vs RHE, the partial current density of CO on unmodified Cu electrode increases, while it remains at the same level at less negative potential on P4VP-



modified Cu electrode. Correspondingly, the FEs of CO, CH<sub>4</sub> and C<sub>2</sub>H<sub>4</sub> on P4VP-modified Cu are lower than on unmodified Cu electrode. Our data therefore suggests that the P4VP layer enhances HCOOH formation, and increases the selectivity of HCOOH at low overpotentials, while it has a negative effect on the selectivity of CH<sub>4</sub> and C<sub>2</sub>H<sub>4</sub> at high overpotentials.

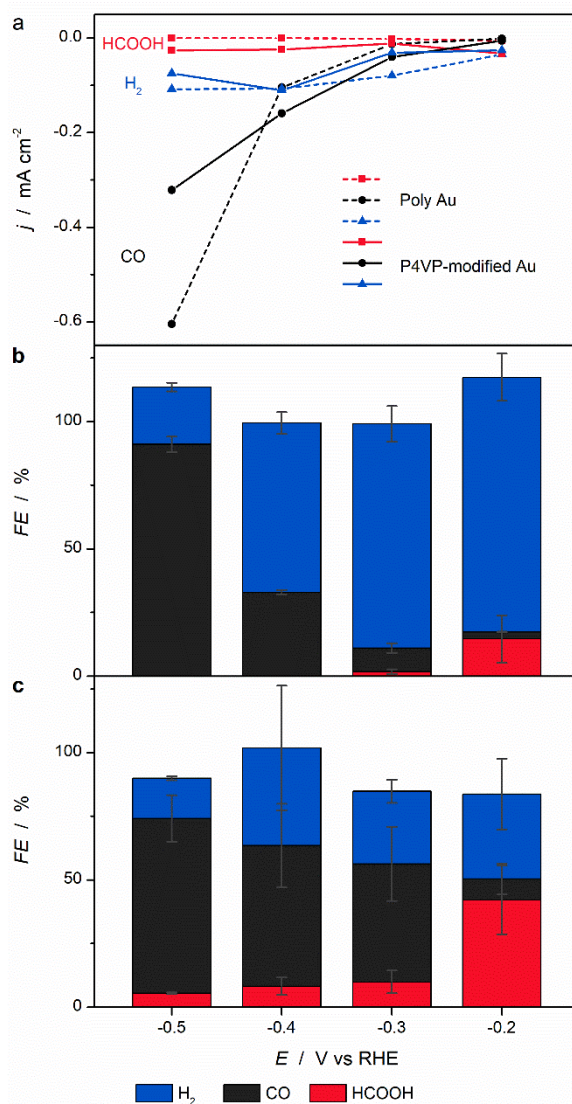


**Figure 2.3** CO<sub>2</sub>RR performance in CO<sub>2</sub> saturated 0.1 M KHCO<sub>3</sub>. (a) Partial current density of H<sub>2</sub>, HCOOH, CO as a function of potential on poly Au (dashed line) and P4VP-modified Au (solid line), with the FEs for observed products on (b) poly Au and (c) P4VP modified polycrystalline Au shown as bars. Errors bars are standard deviations based on three measurements.



To gain additional insights into the mechanism underlying the observed P4VP effects, we continue to investigate the CO<sub>2</sub>RR on unmodified and P4VP-modified poly Au electrodes. Figure 2.3 shows CO<sub>2</sub>RR performance of unmodified and P4VP-modified Au electrodes in CO<sub>2</sub> saturated 0.1 M KHCO<sub>3</sub>. It can be seen in Figures 2.3a (dashed line) and 2.3b that, at low overpotentials, unmodified poly Au predominantly forms hydrogen with only minor amounts of HCOOH and CO, with the former having a relatively higher FE. At increasingly negative potentials, CO<sub>2</sub> reduction gradually takes over, and CO becomes the dominant product whilst HCOOH disappears entirely. In contrast, HCOOH formation is observed on P4VP-modified Au in the entire investigated potential region, as shown in Figure 2.3a (solid line) and Figure 2.3c. Notably, HCOOH is the dominant product at -0.2 V vs RHE with a FE of 42%, although the overall rate is low.

To exclude the possible catalytic effect of the P4VP layer itself, we performed CO<sub>2</sub> reduction on the unmodified pyrolytic graphite and P4VP-modified pyrolytic graphite electrodes (with pyrolytic graphite electrode being chosen for its poor CO<sub>2</sub>RR performance). Measured cyclic voltammograms, and the obtained total current densities at -0.6 V vs RHE on the pyrolytic graphite and P4VP-modified pyrolytic graphite electrodes are shown in Figure A.2. No CO<sub>2</sub>RR products were detected. Therefore, the P4VP layer itself is catalytically inert. This result confirms that the effect of P4VP layer on the activity and selectivity of the CO<sub>2</sub>RR results from the interaction of P4VP layer and metallic active sites (poly Cu and Au).

In an attempt to unravel the origin of the improved CO<sub>2</sub>RR performance, we further employed in situ ATR-SEIRAS to study the surface adsorbates, as well as the interfacial electrolyte species. Figure 2.4 shows the in situ ATR-SEIRA spectra recorded on unmodified Cu (Figure 2.4a) and P4VP-modified Cu (Figure 2.4b) during linear sweep voltammetry (LSV) experiment, scanning from +0.3 to -0.9 V vs RHE at a scan rate of 1 mV/s in CO<sub>2</sub>-saturated 0.1 M KHCO<sub>3</sub>, with the background spectra taken at OCP in Milli-Q water. Besides the H<sub>2</sub>O bending peak at 1650 cm<sup>-1</sup>,<sup>35-38</sup> various bands related to surface adsorbates and electrolyte species are observed in the ATR-SEIRA spectra, with an overview of the different bands pertinent to this work being provided in Table A.1. It can be seen in Figure 2.4a that,

on a polycrystalline copper surface, the dominant bands in the ATR spectrum at +0.3 V vs RHE are located at 1640 and 1511  $\text{cm}^{-1}$ , and can be attributed to a combination of the  $\text{H}_2\text{O}$  bending band (1650  $\text{cm}^{-1}$ ) and the asymmetrical stretching of  $\text{HCO}_3^-$  in solution (1620  $\text{cm}^{-1}$ ) for the former,<sup>36-39</sup> with the latter being indicative of adsorbed  $\text{CO}_3^{2-}$ .<sup>37, 40-41</sup> Additional minor bands are located at 2343, 2001, 1420 and 1330  $\text{cm}^{-1}$ , which correspond to solution phase (dissolved)  $\text{CO}_2$ ,<sup>42</sup> bridge-bound CO ( $\text{CO}_{\text{ad,bridge}}$ ) and solution-phase  $\text{CO}_3^{2-}$  and  $\text{HCO}_3^-$ ,<sup>37, 39, 41, 43-44</sup> respectively. When the potential is scanned to more negative potentials, the band associated with adsorbed  $\text{CO}_3^{2-}$  red-shifts from 1511  $\text{cm}^{-1}$  at +0.3 V vs RHE to 1462  $\text{cm}^{-1}$  at -0.9 V vs RHE as a result of the Stark tuning effect, with the intensity of this band gradually decreasing as  $\text{CO}_3^{2-}$  starts to desorb due to the negatively charged interface at more negative potentials.<sup>37, 40-41</sup> The band at 2001  $\text{cm}^{-1}$  (related to  $\text{CO}_{\text{ad,bridge}}$ ) is similarly found to redshift when the potential is scanned to more negative values whilst simultaneously increasing in intensity, whereas the band at 2343  $\text{cm}^{-1}$  diminishes due to solution-phase  $\text{CO}_2$  being depleted by the  $\text{CO}_2\text{RR}$  at increasingly negative potentials. As for the bands related to solution-phase  $\text{CO}_3^{2-}$  and  $\text{HCO}_3^-$ , their intensity is too weak to make meaningful observations and we will therefore not further discuss. Besides these bands, a number of additional bands starts to appear during the negative-going scan. Although  $\text{CO}_{\text{ad,bridge}}$  is visible already at +0.3 V vs RHE, we know from experiments conducted at higher potential that this band starts to increase from -0.1 V vs RHE. Therefore, we believe that  $\text{CO}_{\text{ad,bridge}}$  at the onset of LSV is an artifact from the initial electrochemical preparation of the surface, with the actual onset of this band being at -0.1 V vs RHE. When the potential is scanned further negative, a broad peak at 2050  $\text{cm}^{-1}$  starts to appear from -0.5 V vs RHE, ascribed to top-bound CO ( $\text{CO}_{\text{ad,top}}$ ) on Cu (100) terrace sites.<sup>43</sup> The appearance of this peak is accompanied by the formation of a sharp band at 2070  $\text{cm}^{-1}$ , which is assigned to  $\text{CO}_{\text{ad,top}}$  on Cu (100) and (111) step sites.<sup>45-46</sup> The latter band becomes increasingly dominant as the potential is scanned further towards -0.9 V vs RHE. Overall, on poly Cu surface, the adsorbed species as well as solution species are changing as a function of the applied potential, the main adsorbates being  $\text{CO}_3^{2-}$ -ad at low overpotential and adsorbed CO at more negative potential.

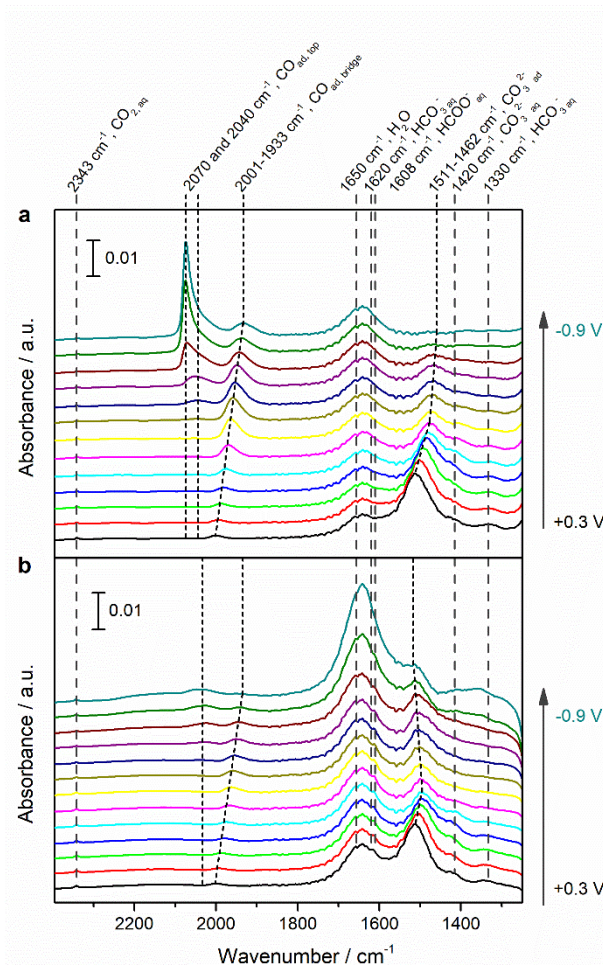


**Figure 2.4** ATR-SEIRA spectra of the CO<sub>2</sub>RR on (a) poly Cu and (b) P4VP-modified Cu during linear sweep voltammetry at 1 mV/s from 0.2 to -0.9 V vs RHE in CO<sub>2</sub> saturated 0.1 M KHCO<sub>3</sub>. The background spectrum was taken at OCP in H<sub>2</sub>O before experiments. The potential interval between spectra is 0.1 V.

A new working electrode was prepared for ATR-SEIRAS experiments on P4VP-modified Cu. To ensure system integrity and surface reproducibility, the copper surface was characterized with ATR-SEIRAS prior to adding a P4VP layer, although the LSV was halted at -0.5 V vs RHE to ensure stability of the surface. As shown in Figure A.3, the presence of CO<sub>ad,top</sub> and CO<sub>ad,bridge</sub> confirms the reproducibility of ATR-SEIRA spectra on the poly Cu surface. The in situ ATR-SEIRA spectra obtained on a P4VP-modified Cu electrode are depicted in Figure 2.4b. Although the P4VP layer seems less stable at the end of LSV (band related to H<sub>2</sub>O and HCO<sub>3</sub><sup>-</sup> at 1620 cm<sup>-1</sup> starts to increase at -0.8 and -0.9 V vs RHE), the bands corresponding to

different interfacial species are located at the same positions during the CO<sub>2</sub>RR. However, after P4VP modification, an additional band at 1608 cm<sup>-1</sup> is observed, which is assigned to the asymmetric stretching of solution-phase HCOO<sup>-</sup>.<sup>37</sup> Contrary to unmodified Cu, at more negative potentials, the band related to CO<sub>ad,top</sub> on (100)/(111) step sites (2070 cm<sup>-1</sup>) is barely present on P4VP-modified Cu, while the bands corresponding to adsorbed CO<sub>ad,top</sub> and CO<sub>ad,bridge</sub> on (100) terraces (2040 and 2001 cm<sup>-1</sup>, respectively) exhibit reduced intensity. With higher CO production (see partial current density, Figure 2.2a) on P4VP-modified Cu between -0.6 and -0.8 V vs RHE, these differences in the CO adsorption band indicate fewer active sites on P4VP-modified Cu, which suggests that the P4VP layer coordinates with Cu active sites, especially with step sites. Furthermore, these reduced CO adsorption bands could also explain the lower selectivity of CH<sub>4</sub> and C<sub>2</sub>H<sub>4</sub> on P4VP-modified Cu electrode. Overall, the discussed results reveal the effect of P4VP layer on adsorbed CO, suggesting an interaction between P4VP layer and metallic poly Cu surface. However, the ATR-SEIRAS results do not give a clear indication of the effect of P4VP layer on interfacial solution species due to the low band intensity.

In previous literature,<sup>36,39</sup> ATR-SEIRAS experiments were applied to determine local pH via the ratio of carbon dioxide and bicarbonate vibrational bands on polycrystalline Au electrodes. To gain further insight into the effect of the modification by P4VP on the near-electrode solution-phase species, we performed in situ ATR-SEIRAS on unmodified Au and P4VP-modified Au electrodes. Figures 2.5a and 2.5b show the recorded ATR-SEIRA spectra during LSV at 1 mV/s in CO<sub>2</sub> saturated 0.1 M KHCO<sub>3</sub> for unmodified and P4VP-modified Au, respectively. Although adsorbed CO bands were observed around 2000 cm<sup>-1</sup> on Au electrodes in previous work,<sup>33, 47-48</sup> they were not observed under our working conditions. We observe only bands related to H<sub>2</sub>O and solution-phase species; CO<sub>2</sub>, HCO<sub>3</sub><sup>-</sup>, CO<sub>3</sub><sup>2-</sup>. Additionally, on P4VP-modified Au, there is a very weak feature at 1608 cm<sup>-1</sup>, which may be assigned to solution HCOO<sup>-</sup>.<sup>37</sup> However, the band attributed to electrolyte HCO<sub>3</sub><sup>-</sup> has a much lower relative intensity on P4VP-modified Au surface, suggesting different local environments after adding the P4VP layer. Instead of looking at absolute band intensity, the ratio of the integrals of the bands related to dissolved CO<sub>2</sub> and solution HCO<sub>3</sub><sup>-</sup> (2343 and 1620 cm<sup>-1</sup>, respectively;

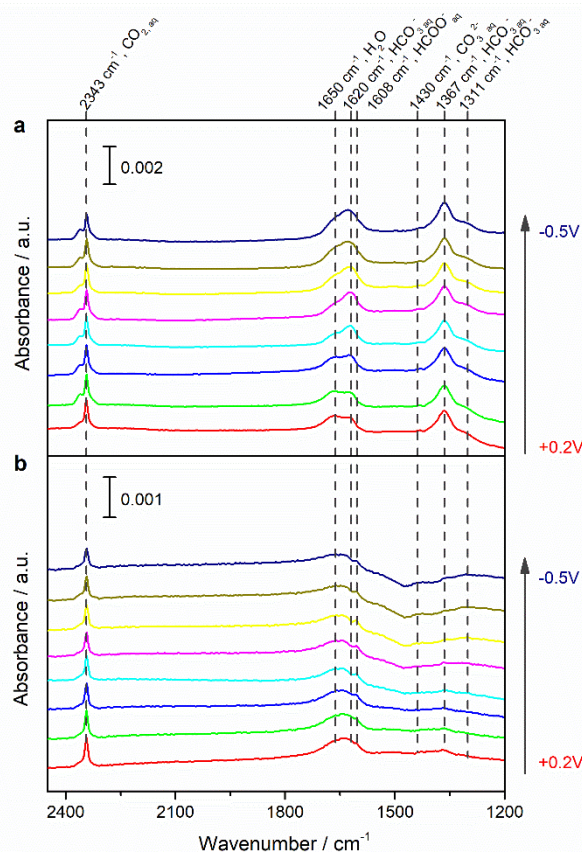


**Figure 2.5** ATR-SEIRA spectra of the CO<sub>2</sub>RR on (a) poly Au and (b) P4VP-modified Au during linear sweep voltammetry at 1 mV/s from 0.2 to -0.5 V vs RHE in CO<sub>2</sub> saturated 0.1 M KHCO<sub>3</sub>. The background spectrum was taken at OCP in pure H<sub>2</sub>O prior to ATR-SEIRAS experiments. The potential interval between spectra is 0.1 V.

$I_{\text{CO}_2} / I_{\text{HCO}_3^-}$ ) was calculated as an indicator of local environment. To avoid convolution with the H<sub>2</sub>O bending band,  $I_{\text{CO}_2} / I_{\text{HCO}_3^-}$  was determined from in situ ATR-SEIRA spectra taken in D<sub>2</sub>O, as the D<sub>2</sub>O bending band is shifted to 1208 cm<sup>-1</sup>. Figure A.4 shows the ATR-SEIRA spectra, obtained on unmodified Au and P4VP-modified Au electrodes in CO<sub>2</sub> saturated 0.05 M K<sub>2</sub>CO<sub>3</sub> in D<sub>2</sub>O. The calculated  $I_{\text{CO}_2} / I_{\text{HCO}_3^-}$  ratio as a function of applied potential for both surfaces is shown in Figure 2.6. On unmodified Au electrodes, the obtained  $I_{\text{CO}_2} / I_{\text{HCO}_3^-}$  agrees with literature reports.<sup>36, 39</sup> Specifically, in the potential region of 0.3 to -0.1 V vs RHE, where no HER nor CO<sub>2</sub>RR occurs,  $I_{\text{CO}_2} / I_{\text{HCO}_3^-}$  remains constant; when the negative-going scan enters the region of -0.2 to -0.4 V vs RHE, where HER and CO<sub>2</sub>RR start,  $I_{\text{CO}_2} / I_{\text{HCO}_3^-}$  keeps decreasing due to the CO<sub>2</sub> consumption and HCO<sub>3</sub><sup>-</sup> formation, as a consequence of the

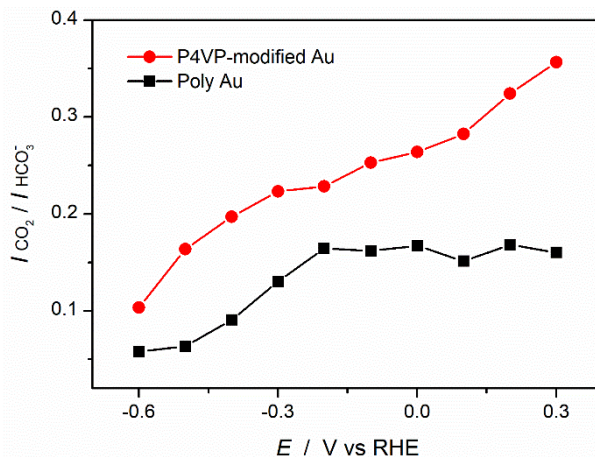


**Figure 2.6** Potential dependency of  $I_{CO_2} / I_{HCO_3^-}$  on poly Au (black) and P4VP-modified Au (red), calculated from ATR-SEIRA spectra obtained during LSV at 1 mV/s in  $CO_2$  saturated 0.1M  $KDCO_3$  in  $D_2O$ . The background spectrum was taken at OCP in  $D_2O$  before experiments.

reaction between  $CO_2$  and  $OH^-$ ; finally, from -0.5 V vs RHE onwards,  $I_{CO_2} / I_{HCO_3^-}$  reaches the lowest point, where  $CO_2$  is almost depleted and  $HCO_3^-$  starts to be consumed by the excess  $OH^-$ , and as a result,  $CO_3^{2-}$  finally become the dominant solution species near the electrode. On the other hand, on the P4VP-modified Au, the obtained  $I_{CO_2} / I_{HCO_3^-}$  (Figure 2.6, red line) is always higher than on the unmodified Au and keeps decreasing with the negative-going scan. The higher value of  $I_{CO_2} / I_{HCO_3^-}$  in the potential region between 0.3 and -0.1 V vs RHE indicates the limited mass transport of  $HCO_3^-$  (compared with  $CO_2$ ) from bulk electrolyte to the P4VP-Cu interface. Moreover, the decreasing  $I_{CO_2} / I_{HCO_3^-}$  in this potential region (where no reaction occurs) suggests slow  $HCO_3^-$  diffusion from bulk electrolyte to the P4VP-Cu interface. Therefore, we propose that this water insoluble P4VP layer not only limits the mass transport of  $H_2O$ , but also limits the mass transport of  $HCO_3^-$ . Both species are proton donor of HER during the  $CO_2RR$ , thereby lowering HER activity. As a result, less  $OH^-$  formation is expected due to the limited HER, and hence less  $CO_2$  is consumed by homogeneous reaction (with  $OH^-$ ) during the  $CO_2RR$ , which could explain the higher  $I_{CO_2} / I_{HCO_3^-}$  on the P4VP-modified surface at more negative potential. Overall, we show the  $I_{CO_2} / I_{HCO_3^-}$  as an indicator of the local environment, which is the  $CO_2/HCO_3^-$  equilibrium resulting

from reactions (both HER and CO<sub>2</sub>RR) at the interface as well as the mass transport from the bulk electrolyte to the interface. We have assigned the inhibited HER on P4VP-modified Cu and Au electrodes to the limit transport of H<sub>2</sub>O and HCO<sub>3</sub><sup>-</sup>, however, the CO<sub>2</sub>RR products distribution is still depends on the nature of the catalysts and the applied potential. Therefore, it is not possible to directly correlate  $I_{\text{CO}_2} / I_{\text{HCO}_3^-}$  ratios with CO or HCOOH yield.

As a final consideration, we investigated surface hydrophobicity, as an indicator of surface and H<sub>2</sub>O interaction, via contact angle measurements. Figure A.5 shows the contact angles between a water droplet and our investigated surfaces. Unmodified Au shows the most hydrophobic surface with a contact angle of 91 degrees. Upon modification with a P4VP layer, both Cu and Au electrodes shows the same contact angle (57 degrees), which is more hydrophilic than poly Au. Surprisingly, unmodified poly Cu exhibits the most hydrophilic surface (17 degrees), which is probably due to the presence of a CuOx layer when the copper surface is exposed to air. However, CV preparation employed in this work prior to the CO<sub>2</sub>RR experiments is expected to remove this CuOx layer, and therefore, a more hydrophobic surface of metallic poly Cu is expected under CO<sub>2</sub>RR conditions. Overall, the contact angle measurements show different interaction between H<sub>2</sub>O and the employed working electrodes. It has been suggested previously that hydrophilic additives improve HCOOH selectivity during the CO<sub>2</sub>RR, by influencing the formation of surface hydrides.<sup>24</sup>

## 2.4 Conclusions

In this work, we investigated the effect of chemical modification via the addition of a P4VP layer on CO<sub>2</sub>RR of poly Cu and Au electrodes. We have shown that the presence of P4VP layer hinders the HER while it enhances the CO<sub>2</sub>RR, especially HCOOH formation, on both electrodes. Less CO-adsorption bands on P4VP-modified Cu and higher  $I_{\text{CO}_2} / I_{\text{HCO}_3^-}$  ratios on P4VP-modified Au are observed from in situ ATR-SEIRAS experiments, compared to unmodified electrodes. This indicates inhibited mass transport of H<sub>2</sub>O and HCO<sub>3</sub><sup>-</sup> from the bulk to the catalytically active sites with the presence of a P4VP layer, whilst also suggesting coordination between the P4VP layer and Cu sites. In addition, contact angle measurement shows P4VP modification influences the hydrophilicity of the surface, which influences

surface hydride formation,<sup>24</sup> resulting in enhanced and preferential HCOOH formation at low overpotential (with respect to CO). We believe that this is an important experimental finding highlighting that the electrolyte side of the catalyst is very important in steering selectivity, so much so that even a catalyst such as Au can produce substantial amounts of HCOOH. Our work offers further understanding of enhanced the CO<sub>2</sub>RR activity and selectivity on P4VP layer modified electrodes, and confirms that functionalization by tailored additives is a promising strategy for developing selective catalysts.



## References

1. Kuhl, K. P.; Cave, E. R.; Abram, D. N.; Jaramillo, T. F., New insights into the electrochemical reduction of carbon dioxide on metallic copper surfaces. *Energy Environ. Sci.* **2012**, 5 (5), 7050-7059.
2. Hatsukade, T.; Kuhl, K. P.; Cave, E. R.; Abram, D. N.; Jaramillo, T. F., Insights into the electrocatalytic reduction of CO<sub>2</sub> on metallic silver surfaces. *Phys. Chem. Chem. Phys.* **2014**, 16 (27), 13814-9.
3. Montoya, J. H.; Shi, C.; Chan, K.; Norskov, J. K., Theoretical Insights into a CO Dimerization Mechanism in CO<sub>2</sub> Electroreduction. *J. Phys. Chem. Lett.* **2015**, 6 (11), 2032-7.
4. Hanselman, S.; Koper, M. T. M.; Calle-Vallejo, F., Computational Comparison of Late Transition Metal (100) Surfaces for the Electrocatalytic Reduction of CO to C<sub>2</sub> Species. *ACS Energy Lett.* **2018**, 3 (5), 1062-1067.
5. Kortlever, R.; Shen, J.; Schouten, K. J.; Calle-Vallejo, F.; Koper, M. T., Catalysts and Reaction Pathways for the Electrochemical Reduction of Carbon Dioxide. *J. Phys. Chem. Lett.* **2015**, 6 (20), 4073-4082.
6. Durst, J.; Rudnev, A.; Dutta, A.; Fu, Y.; Herranz, J.; Kaliginedi, V.; Kuzume, A.; Permyakova, A. A.; Paratcha, Y.; Broekmann, P.; Schmidt, T. J., Electrochemical CO<sub>2</sub> Reduction - A Critical View on Fundamentals, Materials and Applications. *Chimia (Aarau)* **2015**, 69 (12), 769-776.
7. Oloman, C.; Li, H., Electrochemical processing of carbon dioxide. *ChemSusChem* **2008**, 1 (5), 385-91.
8. Yang, Z. N.; Oropeza, F. E.; Zhang, K. H. L., P-block metal-based (Sn, In, Bi, Pb) electrocatalysts for selective reduction of CO<sub>2</sub> to formate. *Appl Materials* **2020**, 8 (6).
9. Min, X.; Kanan, M. W., Pd-catalyzed electrohydrogenation of carbon dioxide to formate: high mass activity at low overpotential and identification of the deactivation pathway. *J. Am. Chem. Soc.* **2015**, 137 (14), 4701-8.
10. Gao, D.; Zhou, H.; Wang, J.; Miao, S.; Yang, F.; Wang, G.; Wang, J.; Bao, X., Size-dependent electrocatalytic reduction of CO<sub>2</sub> over Pd nanoparticles. *J. Am. Chem. Soc.* **2015**, 137 (13), 4288-91.
11. Dinh, C. T.; Burdyny, T.; Kibria, M. G.; Seifitokaldani, A.; Gabardo, C. M.; Garcia de Arquer, F. P.; Kiani, A.; Edwards, J. P.; De Luna, P.; Bushuyev, O. S.; Zou, C.; Quintero-Bermudez, R.; Pang, Y.; Sinton, D.; Sargent, E. H., CO<sub>2</sub> electroreduction to ethylene via hydroxide-mediated copper catalysis at an abrupt interface. *Science* **2018**, 360 (6390), 783-787.
12. Chen, X.; Chen, J.; Alghoraibi, N. M.; Henckel, D. A.; Zhang, R.; Nwabara, U. O.; Madsen, K. E.; Kenis, P. J. A.; Zimmerman, S. C.; Gewirth, A. A., Electrochemical CO<sub>2</sub>-to-ethylene conversion on polyamine-incorporated Cu electrodes. *Nat. Catal.* **2020**, 4 (1), 20-27.
13. Wang, X.; Klingan, K.; Klingenhof, M.; Moller, T.; Ferreira de Araujo, J.; Martens, I.; Bagger, A.; Jiang, S.; Rossmeisl, J.; Dau, H.; Strasser, P., Morphology and mechanism of highly selective Cu(II) oxide nanosheet catalysts for carbon dioxide electroreduction. *Nat. Commun.* **2021**, 12 (1), 1-12.
14. Pavesi, D.; Dattila, F.; Van de Poll, R. C. J.; Anastasiadou, D.; García-Muelas, R.; Figueiredo, M.; Gruter, G.-J. M.; López, N.; Koper, M. T. M.; Schouten, K. J. P., Modulation of the selectivity of CO<sub>2</sub> to CO electroreduction in palladium rich Palladium-Indium nanoparticles. *J. Catal.* **2021**, 402, 229-237.
15. Ponnurangam, S.; Yun, C. M.; Chernyshova, I. V., Robust Electroreduction of CO<sub>2</sub> at a Poly(4-vinylpyridine)-Copper Electrode. *ChemElectroChem* **2016**, 3 (1), 74-82.

16. Han, Z.; Kortlever, R.; Chen, H. Y.; Peters, J. C.; Agapie, T., CO<sub>2</sub> Reduction Selective for C<sub>≥2</sub> Products on Polycrystalline Copper with N-Substituted Pyridinium Additives. *ACS Cent. Sci.* **2017**, *3* (8), 853-859.
17. Ahn, S.; Klyukin, K.; Wakeham, R. J.; Rudd, J. A.; Lewis, A. R.; Alexander, S.; Carla, F.; Alexandrov, V.; Andreoli, E., Poly-Amide Modified Copper Foam Electrodes for Enhanced Electrochemical Reduction of Carbon Dioxide. *ACS Catal.* **2018**, *8* (5), 4132-4142.
18. Thevenon, A.; Rosas-Hernandez, A.; Peters, J. C.; Agapie, T., In-Situ Nanostructuring and Stabilization of Polycrystalline Copper by an Organic Salt Additive Promotes Electrocatalytic CO<sub>2</sub> Reduction to Ethylene. *Angew. Chem. Int. Ed. Engl.* **2019**, *58* (47), 16952-16958.
19. Wei, X.; Yin, Z.; Lyu, K.; Li, Z.; Gong, J.; Wang, G.; Xiao, L.; Lu, J.; Zhuang, L., Highly Selective Reduction of CO<sub>2</sub> to C<sub>2+</sub> Hydrocarbons at Copper/Polyaniline Interfaces. *ACS Catal.* **2020**, *10* (7), 4103-4111.
20. Wagner, A.; Sahm, C. D.; Reisner, E., Towards molecular understanding of local chemical environment effects in electro- and photocatalytic CO<sub>2</sub> reduction. *Nat. Catal.* **2020**, *3* (10), 775-786.
21. Sharifi Golru, S.; Biddinger, E. J., Effect of additives in aqueous electrolytes on CO<sub>2</sub> electroreduction. *Chem. Eng. J.* **2021**, *428*, 131303-131323.
22. Mu, S.; Li, L.; Zhao, R.; Lu, H.; Dong, H.; Cui, C., Molecular-Scale Insights into Electrochemical Reduction of CO<sub>2</sub> on Hydrophobically Modified Cu Surfaces. *ACS Appl. Mater. Interfaces* **2021**, *13* (40), 47619-47628.
23. Gutierrez-Sanchez, O.; Daems, N.; Bulut, M.; Pant, D.; Breugelmans, T., Effects of Benzyl-Functionalized Cationic Surfactants on the Inhibition of the Hydrogen Evolution Reaction in CO<sub>2</sub> Reduction Systems. *ACS Appl. Mater. Interfaces* **2021**, *13* (47), 56205-56216.
24. Buckley, A. K.; Lee, M.; Cheng, T.; Kazantsev, R. V.; Larson, D. M.; Goddard, W. A., III; Toste, F. D.; Toma, F. M., Electrocatalysis at Organic-Metal Interfaces: Identification of Structure-Reactivity Relationships for CO<sub>2</sub> Reduction at Modified Cu Surfaces. *J. Am. Chem. Soc.* **2019**, *141* (18), 7355-7364.
25. Cave, E. R.; Montoya, J. H.; Kuhl, K. P.; Abram, D. N.; Hatsukade, T.; Shi, C.; Hahn, C.; Nørskov, J. K.; Jaramillo, T. F., Electrochemical CO<sub>2</sub> reduction on Au surfaces: mechanistic aspects regarding the formation of major and minor products. *Phys. Chem. Chem. Phys.* **2017**, *19* (24), 15856-15863.
26. Monteiro, M. C. O.; Philips, M. F.; Schouten, K. J. P.; Koper, M. T. M., Efficiency and selectivity of CO<sub>2</sub> reduction to CO on gold gas diffusion electrodes in acidic media. *Nat. Commun.* **2021**, *12* (1), 1-7.
27. Ren, D.; Wong, N. T.; Handoko, A. D.; Huang, Y.; Yeo, B. S., Mechanistic Insights into the Enhanced Activity and Stability of Agglomerated Cu Nanocrystals for the Electrochemical Reduction of Carbon Dioxide to n-Propanol. *J. Phys. Chem. Lett.* **2016**, *7* (1), 20-4.
28. Klingan, K.; Kottakatt, T.; Jovanov, Z. P.; Jiang, S.; Pasquini, C.; Scholten, F.; Kubella, P.; Bergmann, A.; Roldan Cuenya, B.; Roth, C.; Dau, H., Reactivity Determinants in Electrodeposited Cu Foams for Electrochemical CO<sub>2</sub> Reduction. *ChemSusChem* **2018**, *11* (19), 3449-3459.
29. Tang, W.; Peterson, A. A.; Varela, A. S.; Jovanov, Z. P.; Bech, L.; Durand, W. J.; Dahl, S.; Nørskov, J. K.; Chorkendorff, I., The importance of surface morphology in controlling the selectivity of polycrystalline copper for CO<sub>2</sub> electroreduction. *Phys. Chem. Chem. Phys.* **2012**, *14* (1), 76-81.
30. Simon, G. H.; Kley, C. S.; Roldan Cuenya, B., Potential-Dependent Morphology of Copper Catalysts During CO<sub>2</sub> Electroreduction Revealed by In Situ Atomic Force Microscopy. *Angew. Chem.*

*Int. Ed. Engl.* **2021**, 60 (5), 2561-2568.

31. Hamelin, A., Cyclic voltammetry at gold single-crystal surfaces. Part 1. Behaviour at low-index faces. *J. Electroanal. Chem.* **1996**, 407 (1-2), 1-11.
32. Yoshida, K.; Kuzume, A.; Broekmann, P.; Pobelov, I. V.; Wandlowski, T., Reconstruction and electrochemical oxidation of Au(110) surface in 0.1 M H<sub>2</sub>SO<sub>4</sub>. *Electrochim. Acta* **2014**, 139, 281-288.
33. Marcandalli, G.; Villalba, M.; Koper, M. T. M., The Importance of Acid-Base Equilibria in Bicarbonate Electrolytes for CO<sub>2</sub> Electrochemical Reduction and CO Reoxidation Studied on Au(hkl) Electrodes. *Langmuir* **2021**, 37 (18), 5707-5716.
34. Tapan, N. A., CO<sub>2</sub> electroreduction on P4VP modified copper deposited gas diffusion layer electrode: pH effect. *Mater. Renew. Sustain. Energy* **2016**, 5 (4), 1-10.
35. Shaw, S. K.; Berna, A.; Feliu, J. M.; Nichols, R. J.; Jacob, T.; Schiffrin, D. J., Role of axially coordinated surface sites for electrochemically controlled carbon monoxide adsorption on single crystal copper electrodes. *Phys. Chem. Chem. Phys.* **2011**, 13 (12), 5242-51.
36. Ayemoba, O.; Cuesta, A., Spectroscopic Evidence of Size-Dependent Buffering of Interfacial pH by Cation Hydrolysis during CO<sub>2</sub> Electroreduction. *ACS Appl. Mater. Interfaces* **2017**, 9 (33), 27377-27382.
37. Moradzaman, M.; Mul, G., Infrared Analysis of Interfacial Phenomena during Electrochemical Reduction of CO<sub>2</sub> over Polycrystalline Copper Electrodes. *ACS Catal.* **2020**, 10 (15), 8049-8057.
38. Larsen, O. F.; Woutersen, S., Vibrational relaxation of the H<sub>2</sub>O bending mode in liquid water. *J. Chem. Phys.* **2004**, 121 (24), 12143-5.
39. Dunwell, M.; Yang, X.; Setzler, B. P.; Anibal, J.; Yan, Y.; Xu, B., Examination of Near-Electrode Concentration Gradients and Kinetic Impacts on the Electrochemical Reduction of CO<sub>2</sub> using Surface-Enhanced Infrared Spectroscopy. *ACS Catal.* **2018**, 8 (5), 3999-4008.
40. Sartin, M. M.; Yu, Z.; Chen, W.; He, F.; Sun, Z.; Chen, Y.-X.; Huang, W., Effect of Particle Shape and Electrolyte Cation on CO Adsorption to Copper Oxide Nanoparticle Electrocatalysts. *J. Phys. Chem. C* **2018**, 122 (46), 26489-26498.
41. Arihara, K.; Kitamura, F.; Ohsaka, T.; Tokuda, K., Characterization of the adsorption state of carbonate ions at the Au(111) electrode surface using in situ IRAS. *J. Electroanal. Chem.* **2001**, 510, 128-135.
42. Falk, M.; Miller, A. G., Infrared spectrum of carbon dioxide in aqueous solution. *Vib. Spectrosc* **1992**, 4, 105-108.
43. Hori, Y.; Koga, O.; Watanabe, Y.; Matsuo, T., FTIR measurements of charge displacement adsorption of CO, on poly- and single crystal (100) of Cu electrodes. *Electrochim. Acta* **1998**, 44 (8-9), 1389-1395.
44. Gunathunge, C. M.; Ovalle, V. J.; Li, Y.; Janik, M. J.; Waagele, M. M., Existence of an Electrochemically Inert CO Population on Cu Electrodes in Alkaline pH. *ACS Catal.* **2018**, 8 (8), 7507-7516.
45. Koga, O.; Teruya, S.; Matsuda, K.; Minami, M.; Hoshi, N.; Hori, Y., Infrared spectroscopic and voltammetric study of adsorbed CO on stepped surfaces of copper monocrystalline electrodes. *Electrochim. Acta* **2005**, 50 (12), 2475-2485.
46. Gunathunge, C. M.; Li, X.; Li, J.; Hicks, R. P.; Ovalle, V. J.; Waagele, M. M., Spectroscopic Observation of Reversible Surface Reconstruction of Copper Electrodes under CO<sub>2</sub> Reduction. *J. Phys. Chem. C* **2017**, 121 (22), 12337-12344.
47. Rodriguez, P.; Garcia-Araez, N.; Koverga, A.; Frank, S.; Koper, M. T., CO electrooxidation on

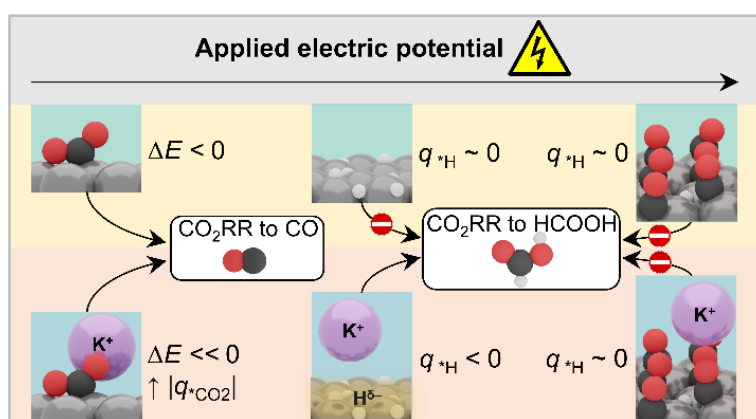
gold in alkaline media: a combined electrochemical, spectroscopic, and DFT study. *Langmuir* **2010**, 26 (14), 12425-32.

48. Wuttig, A.; Yaguchi, M.; Motobayashi, K.; Osawa, M.; Surendranath, Y., Inhibited proton transfer enhances Au-catalyzed CO<sub>2</sub>-to-fuels selectivity. *Proc. Natl. Acad. Sci. U.S.A.* **2016**, 113 (32), E4585-93.



## Chapter 3

### Influence of Cations on HCOOH and CO Formation during CO<sub>2</sub> Reduction on a Pd<sub>ML</sub>Pt(111) Electrode



This chapter is based on:

Ye, C.; Dattila, F.; Chen, X.; Lopez, N.; Koper, M. T. M. *J. Am. Chem. Soc.* **2023**, 145 (36), 19601-19610.

**Abstract:** Understanding the role of cations on the electrochemical CO<sub>2</sub> reduction (CO<sub>2</sub>RR) process is of fundamental importance for practical application. In this work, we investigate how cations influence HCOOH and CO formation on Pd<sub>ML</sub>Pt(111) in pH 3 electrolytes. While only (a small amount of adsorbed) CO forms on Pd<sub>ML</sub>Pt(111) in the absence of metal cations, the onset potential of HCOOH and CO decreases with increasing cation concentrations. The cation effect is stronger on HCOOH formation compared to CO formation on Pd<sub>ML</sub>Pt(111). Density functional theory simulations indicate that cations facilitate both hydride formation and CO<sub>2</sub> activation by polarizing the electronic density at the surface and stabilizing \*CO<sub>2</sub><sup>-</sup>. Although the upshift of the metal work function caused by high coverage of adsorbates limits hydride formation, the cation-induced electric field counterbalances this effect in case of \*H species, sustaining HCOOH production at mild negative potentials. Instead, at the high \*CO coverages observed at very negative potentials, surface hydrides do not form, preventing the HCOOH route both in absence and presence of cations. Our results open the way for a consistent evaluation of cationic electrolyte effects on both activity and selectivity in CO<sub>2</sub>RR on Pd-Pt catalysts.

### 3.1 Introduction

The electrochemical carbon dioxide reduction reaction (CO<sub>2</sub>RR) into fuels and chemicals has recently gained substantial attention as a promising method to utilize this abundant carbon feedstock and to store excess renewable electric energy. In aqueous media, the CO<sub>2</sub>RR can generate various products, including formic acid (HCOOH), carbon monoxide (CO), hydrocarbons, and alcohols, depending on the catalyst and the microenvironment.<sup>1-4</sup> Therefore, understanding the factors determining selectivity at the molecular level is crucial to ensure the future application of CO<sub>2</sub>RR.

The nature of the metal catalyst has an important effect on the activity and selectivity in CO<sub>2</sub>RR. Of the monometallic catalysts, Cu exhibits a unique selectivity to methane and various multi-carbon products such as ethylene, ethanol, and propanol.<sup>5-8</sup> Precious metal catalysts such as Au and Ag show high selectivity towards CO in CO<sub>2</sub>RR.<sup>4,9</sup> Platinum-group metals, are also selective for CO formation but are affected by CO surface poisoning.<sup>3, 10-12</sup> Pd-based catalysts can reach a Faradaic efficiency of 95% for CO generation at negative potentials (-0.8 V<sub>RHE</sub>).<sup>10-11</sup> However, this selectivity is potential dependent and Pd can also deliver a high Faradaic efficiency towards HCOOH (close to 99%) with a small overpotential of 0.1 V.<sup>3</sup> Although Pd deactivates over a few hours because of the simultaneous formation of (adsorbed) CO,<sup>3</sup> Pd is an excellent candidate to study the electrochemical CO<sub>2</sub>RR because of this selectivity switch between HCOOH and CO formation in different potential windows.

To better understand the special reactivity of Pd for CO<sub>2</sub>RR, detailed investigations on atomically well-defined Pd surfaces are highly desirable. Pt single crystals modified with a Pd monolayer are good candidates as their electrochemical and electrocatalytic properties have been shown to be similar to bulk Pd single crystals, but they do not exhibit the bulk-like hydrogen absorption of Pd crystals (a process which will mask the CO<sub>2</sub>RR current).<sup>13-15</sup> Recent work has shown that a Pd<sub>ML</sub>Pt(111) single-crystal electrode has a high, almost reversible catalytic activity for the reduction of CO<sub>2</sub> to HCOOH and the oxidation of HCOOH to CO<sub>2</sub>, very similar to bulk Pd crystals.<sup>16</sup> The high activity for the reduction of CO<sub>2</sub> to HCOOH at low overpotential was ascribed to the hydridic (negatively-charged) character



of the surface adsorbed hydrogen  $*H^{\delta-}$  on Pd<sub>ML</sub>Pt(111), which reacts with CO<sub>2</sub> in the solution close to the metal to form HCOOH.<sup>3, 16</sup> This hydridic character was reported to depend on the metal work function.<sup>3, 16</sup> At more negative potentials,  $*CO_2$  binding through the carbon becomes more favorable, eventually leading to the formation of surface adsorbed  $*CO$ , which poisons the electrode.<sup>16</sup> Recently, surface polarization has been proposed as a crucial trigger for hydride transfer on transition metals.<sup>17</sup> Specifically, it was observed that more negative applied potentials increase the electrostatic potential drop at the metal/electrolyte interface, boosting the hydride transfer to acceptor molecules in the electrolyte.

Other than the nature of the catalyst, the electrolyte composition, especially the cations, has been shown to have a strong impact on the CO<sub>2</sub>RR activity and selectivity.<sup>18-22</sup> On copper, silver, and gold electrodes,<sup>22</sup> it was observed that the reduction of CO<sub>2</sub> to CO does not occur in the absence of (alkali) cations in the electrolyte. This was ascribed to the stabilizing interaction between the cation and the first CO<sub>2</sub> reduction intermediate (negatively charged surface-adsorbed CO<sub>2</sub>, denoted as  $*CO_2^{\delta-}$ ), although other effects of alkali cations have also been suggested (regulation of local pH and/or the local double layer electric field).<sup>22</sup> A HCOO<sup>-</sup>-mediated pathway to CO has been proposed to occur on Ag(111) *via* outer-sphere cation activation of CO<sub>2</sub>.<sup>23</sup> These observations make it relevant to investigate the cation effect on HCOOH formation, for which the Pd<sub>ML</sub>Pt(111) electrode is an ideal model system.

In this work, we present CO<sub>2</sub>RR performance on a Pd<sub>ML</sub>Pt(111) electrode in a pH 3 electrolyte with various cation concentrations, focusing on selectivity differences between HCOOH and CO formation as a function of potential. We show that the onset potential for both HCOOH and CO formation shifts to more positive potential with the increase of the cation concentration. Remarkably, there is a differential effect in the reaction paths, the cation effect being stronger on HCOOH formation than on CO formation. Based on complementary density functional theory simulations, we present a mechanism to explain why HCOOH generation is highly sensitive to the presence of cations in the electrolyte under realistic conditions, *i.e.* high  $*H$  and  $*CO$  coverages. Our work underscores the crucial importance of cations and the overall microenvironment design in catalytic CO<sub>2</sub>RR.

### 3.2 Experimental Section

**Chemicals and cell preparation.** Ultrapure water (resistivity  $> 18.2 \text{ M}\Omega\cdot\text{cm}$ , Millipore Milli-Q) was used for all experiments in this work. Prior to each experiment, all cell compartments were cleaned by storing them in a potassium permanganate solution ( $1 \text{ g}\cdot\text{L}^{-1} \text{ KMnO}_4$  (Fluka, ACS reagent) in  $0.5 \text{ M H}_2\text{SO}_4$  (Fluka, ACS reagent)) overnight. The solution was subsequently drained and the cell compartments were rinsed with a dilute piranha solution (1:3 v/v of  $\text{H}_2\text{O}_2$  (Merck, Emprove exp) /  $\text{H}_2\text{SO}_4$ ) to remove residual  $\text{KMnO}_4$  and  $\text{MnOx}$ . Afterwards, the cell compartments were cleaned by repetitively rinsing and boiling with Milli-Q water to remove all inorganic contaminants. Electrolytes were prepared from  $\text{LiClO}_4$  (Sigma-Aldrich,  $\geq 99.99\%$  trace metal basis),  $\text{NaClO}_4$  (Sigma-Aldrich,  $\geq 99.99\%$  trace metal basis),  $\text{KClO}_4$  (Sigma-Aldrich,  $\geq 99.99\%$  trace metal basis),  $\text{NaClO}_4$  (Sigma-Aldrich,  $\geq 99.99\%$  trace metal basis),  $\text{H}_2\text{SO}_4$  (Merck, Suprapur, 96%),  $\text{PdSO}_4$  (Sigma-Aldrich, 99.99% trace metal basis) and  $\text{HClO}_4$  (Sigma-Aldrich, Ultrapure, 70%). In this work, a Pt wire (0.5 mm diameter, MaTecK, 99.9%) was used as the counter electrode, a reversible hydrogen electrode (RHE) was used as the reference electrode, and all the potentials were iR corrected and controlled with an Autolab PGSTAT302N potentiostat.

**Preparation of Pd monolayers on Pt (111) single crystal.** The characterization and preparation of the electrodes were carried out in the hanging meniscus configuration in standard three-electrode glass cells. Prior to each experiment, argon (Linde, 5.0) was purged through the electrolyte for 30 min to remove air from the solution. The Pt(111) single crystal (area =  $0.08 \text{ cm}^2$ ) was prepared according to the Clavilier method<sup>24</sup> and characterized with cyclic voltammetry in  $0.1 \text{ M HClO}_4$ . Cyclic voltammogram of Pt(111) in  $0.1 \text{ M HClO}_4$  measured at  $50 \text{ mV s}^{-1}$  is shown in Figure B.1a. Afterwards, the Pd monolayer was deposited on the Pt(111) single crystal with the method previously reported by our group.<sup>16, 25</sup> Briefly, the prepared Pt(111) single crystal was transferred and immersed into a  $\text{Pd}^{2+}$  containing electrolyte at  $+0.85 \text{ V}_{\text{RHE}}$ , and then cycled between  $+0.07$  and  $+0.85 \text{ V}_{\text{RHE}}$  until a full monolayer of Pd was formed on Pt(111). The corresponding Pd formation process on Pt(111) is shown in Figure B.1b, with the growth of a sharp peak at  $0.23 \text{ V}_{\text{RHE}}$  representing the

accumulation of Pd on the Pt(111) surface and a decreasing peak at 0.5 V<sub>RHE</sub> which is the characteristic spike of Pt(111) in 0.1M H<sub>2</sub>SO<sub>4</sub>.<sup>25</sup> With the accumulation of Pd on Pt(111), the peak at 0.5 V<sub>RHE</sub> eventually disappears, which suggests a full monolayer on Pt(111) surface. After Pd monolayer deposition, the Pd<sub>ML</sub>Pt(111) electrode was taken from the cell and rinsed with Milli-Q water thoroughly. Finally, the freshly prepared Pd<sub>ML</sub>Pt(111) was characterized in 0.1M HClO<sub>4</sub> and used as working electrode in the subsequent experiments.

**Electrochemical measurements.** All electrochemical experiments were carried out in a standard three-electrode electrochemical cell. The CO<sub>2</sub>RR experiment in the absence of metal cations was performed in 1 mM HClO<sub>4</sub> (pH 3). pH=3 was chosen as it is the highest pH where one still has reasonable electrolyte conductivity in the absence of (alkali) cations, while having low proton reduction current. In case of electrolytes with different cation concentrations, calculated amounts of salt were added to 1 mM HClO<sub>4</sub> solution. Prior to each experiment, CO<sub>2</sub> (Linde, 4.5) was purged through the electrolyte for at least 30 min to obtain a CO<sub>2</sub>-saturated electrolyte. Cyclic voltammetry measurements at 10 or 50 mV s<sup>-1</sup> were first taken in pH 3 working electrolytes. Afterwards, linear sweep voltammetry measurements were performed from 0.1 V<sub>RHE</sub> to the required negative potentials at 1 mV s<sup>-1</sup>, followed immediately by CO oxidation stripping experiments taken at 10 mV s<sup>-1</sup>. The scan rate for CO oxidation stripping experiments was chosen to oxidize all CO adsorbed on Pd surface in one scan. Due to the strong CO adsorption on Pd surface,<sup>25</sup> CO generated during CO<sub>2</sub>RR remains on Pd surface until it is oxidized to CO<sub>2</sub> during the CO oxidation stripping experiments. With a known surface area of the electrode (the same surface area as Pt(111) single crystal), the CO surface coverage generated during CO<sub>2</sub>RR was then estimated from the CO oxidation charge obtained from the stripping experiments.<sup>16, 26</sup> In case of linear sweep voltammetry recorded in argon-purged electrolyte, argon was first purged through the electrolyte for at least 30 min to obtain an air-free electrolyte and then linear sweep voltammetry experiments were performed from 0.1 V<sub>RHE</sub> to negative potential at a scan rate of 10 mV s<sup>-1</sup>.

**Online high-performance liquid chromatography (HPLC).** All the online HPLC experiments were carried out in a H-type electrochemical cell equipped with three electrodes.

The cell compartments were separated by a Nafion 117 membrane. Prior to the online HPLC experiments, CO<sub>2</sub> (Linde, 4.5) was purged through the cell for at least 30 min to saturate the electrolyte. While a linear sweep voltammetry was performed from +0.1 V<sub>RHE</sub> to the required negative potentials at 1 mV s<sup>-1</sup>, liquid samples were simultaneously collected with an open tip positioned close to our working electrode at a collection rate of 60 µL min<sup>-1</sup>.<sup>27</sup> Therefore, each sample contains products averaged over a potential range of 60 mV. Or in other words, each sample takes a collection time of 60 s. Afterwards, the collected samples were analyzed by HPLC equipped with an Aminex HPX-87H column (BioRad) and a RID detector (Shimadzu). Notably, the obtained HCOOH concentration in this work is a measure of the HCOO<sup>-</sup> concentration near the working electrode (which will be higher than bulk HCOO<sup>-</sup> concentration) and therefore not suitable for a quantitative Faradaic efficiency determination. Chronoamperometry experiments at -1.2 V<sub>RHE</sub> were performed to check HCOOH formation in a pH 3 electrolyte in the absence of metal cations. The online-HPLC tip was positioned close to the working electrode. After 10 min of chronoamperometry, a liquid sample was taken and further analyzed with HPLC. A higher local HCOOH concentration (if there is any formed during CO<sub>2</sub>RR) with chronoamperometry at fixed potentials is expected and detected with HPLC.

**Density functional theory details.** We performed the density functional theory (DFT) simulations through the Vienna Ab initio Simulation Package (VASP).<sup>28-29</sup> We employed the PBE density functional<sup>30</sup> including dispersion through the DFT-D2 method,<sup>31-32</sup> with our reparametrized C<sub>6</sub> coefficients.<sup>33</sup> Inner electrons were reproduced by PAW pseudopotentials<sup>34-35</sup> and the monoelectronic states for the valence electrons were expanded as plane waves with a kinetic energy cutoff of 450 eV. We modeled the experimental system in agreement with our recent works.<sup>22, 36</sup> The surface model for the cation-free case consisted of a (3×3) Pd<sub>ML</sub>Pt(111) supercell, including 1 Pd monolayer on top of 4 Pt layers, where the two bottom layers were kept fixed to the bulk distance (see Figure 3.5a-b). To assess the role of alkali cations, we introduced in the simulation cell a solvated K<sup>+</sup> (with 5 H<sub>2</sub>O in its coordination shell), fixing its z-coordinate to a distance of 4 Å (near-cation) and 9 Å (far-cation) from the surface layer. We considered two systems with different cation-surface

distance to decouple short- and long-range cation interactions. Besides, to assess the case of charged simulations cells,<sup>37</sup> we considered for both the near- and far-cation cases a cell with 1 excess electron ( $K^+$  without  $OH^-$ ) and a neutral cell ( $K^+$  with  $OH^-$ ). For the second system,  $K^+$  was neutralized *via* a  $OH^-$  formed by removing a hydrogen from one of the  $H_2O$  molecules.<sup>22</sup> The vacuum extended for at least 10 Å beyond cation's solvation shell (or the Pd surface layer, for the cation-free case). Since the solvation layer with cations, water molecules, and adsorbates was placed only on one side of the slab, an additional dipole correction was applied to remove spurious contributions arising from the asymmetric slab model.<sup>38</sup>

**Effect of applied electric potential on formation energies.** The thermodynamics of  $CO_2$  activation was assessed by computing the formation energy of this intermediate (Equations 3.1-2). A  $CO_2$  (1/9 ML) was let to adsorb on the surface. For the system with 4 Å distance between  $K^+$  and surface, the adsorbate was initially placed in proximity of the alkali cation ( $d_{K^+-O(CO_2)} \sim 2.80$  Å)<sup>39</sup> to enable short-range cation effects. Formation energies were calculated taking as energy references  $CO_2(g)$ ,  $H_2O(g)$ , and surface+solvation layer, *i.e.*  $Pd_{ML}Pt(111) 3\times 3 + K^+(5H_2O)$ . To account for variations in the metal work function and consequent changes of electric potential along the reaction path, we first estimated DFT formation energies at the electrostatic potential  $\Phi$  corresponding to the work function  $W$  of the environment. The electrostatic potential  $\Phi$  was calculated by normalizing the work function by the unit of elementary charge  $e^-$  ( $-1e^-$ ).<sup>40</sup>  $E$  and  $\Phi$  indicate respectively DFT energies and electrostatic potential for surface + solvation + adsorbate (ads) and surface + solvation alone (surf), as reported in Table B.1, while  $q$  represents the surface charge density for initial state (surface + solvation) and final state (surface + solvation + adsorbate), see Table B.2. Next, we computed all energies at the work function corresponding to an applied electric potential of -0.40 V vs RHE (*i.e.* -0.58 V vs SHE at pH = 3) through Equation 3.2.<sup>41</sup> Given that the work function for the standard hydrogen electrode is 4.4 eV,<sup>40</sup> at an applied potential of -0.4 V vs RHE the expected metal work function is 3.82 eV.  $\Delta q$  represents the change in surface electronic charge along the reaction step and it is given in unit of elementary charge  $e^-$  ( $-1e^-$ ).

$$E_{\text{ads}}(\Phi_{\text{surf}}) - E_{\text{surf}}(\Phi_{\text{surf}}) = E_{\text{ads}}(\Phi_{\text{ads}}) - E_{\text{surf}}(\Phi_{\text{surf}}) + \frac{(q_{\text{ads}} - q_{\text{surf}})(\Phi_{\text{ads}} - \Phi_{\text{surf}})}{2} \quad (3.1)$$

$$\Delta E(\Phi_{-0.4 \text{ V vs RHE}}) = \Delta E(\Phi_{\text{surf}}) + \Delta q(\Phi_{\text{surf}} - \Phi_{-0.4 \text{ V vs RHE}}) \quad (3.2)$$

### 3.3 Results and Discussion

#### 3.3.1 Results

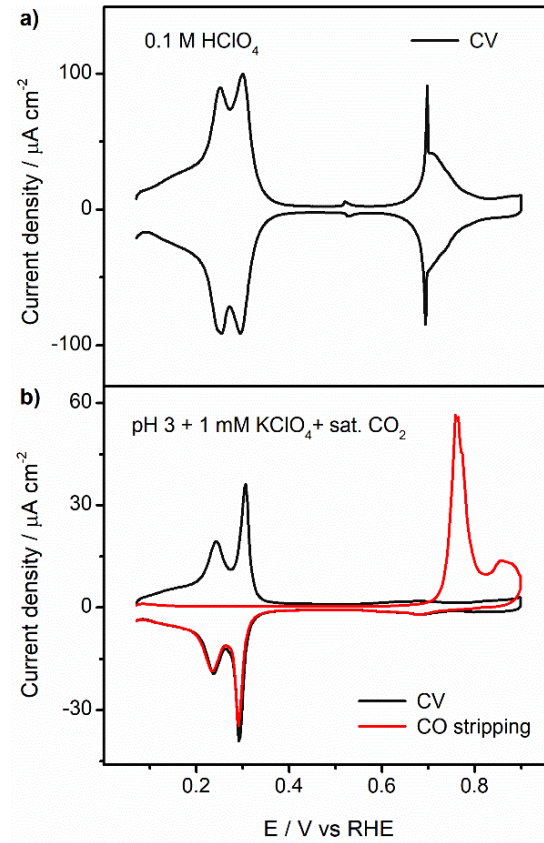


**Figure 3.1 Cyclic Voltammetry of Pd<sub>ML</sub>Pt(111).** a) Cyclic voltammogram of Pd<sub>ML</sub>Pt(111) electrode in 0.1M HClO<sub>4</sub>. Scan rate: 50 mV s<sup>-1</sup>. b) Blank cyclic voltammograms (black) and CO stripping voltammogram (red) of Pd<sub>ML</sub>Pt(111) in CO<sub>2</sub>-saturated pH 3 electrolyte in the presence of 1 mM KClO<sub>4</sub>. Scan rate: 10 mV s<sup>-1</sup>.

**Cyclic voltammetry of Pd<sub>ML</sub>Pt(111).** Figure 3.1a shows the blank cyclic voltammogram of Pd<sub>ML</sub>Pt(111) in 0.1M HClO<sub>4</sub>. The blank curve, measured at 50 mV s<sup>-1</sup>, shows the characteristic regions of the Pd<sub>ML</sub>Pt(111) electrode: a region between +0.05 and +0.35 V<sub>RHE</sub>

with peaks at +0.21 and +0.31  $V_{\text{RHE}}$ , corresponding to the replacement of adsorbed  $\ast\text{H}$  by adsorbed  $\ast\text{OH}$  and the replacement of adsorbed  $\ast\text{OH}$  by adsorbed  $\ast\text{ClO}_4^-$ , respectively; a low-current region between +0.35 and +0.65  $V_{\text{RHE}}$  in which the surface is covered with adsorbed perchlorate anions (which appear to undergo a structural transition at ca. +0.52  $V_{\text{RHE}}$ ); and a region between +0.65 and +0.90  $V_{\text{RHE}}$  with a sharp peak at +0.69  $V_{\text{RHE}}$ , which is ascribed to the replacement of adsorbed  $\ast\text{ClO}_4^-$  by a higher coverage of  $\ast\text{OH}$  adsorption or  $\ast\text{O}$  adsorption.<sup>16, 25</sup> The blank voltammetry in Figure 3.1a confirms the deposition of a single Pd monolayer on the Pt(111) single crystal as well as the cleanliness of the electrolyte, thereby ensuring the robustness and reproducibility of the experiments in this work.

There are small changes and shifts in these peaks for a pH 3 electrolyte in the absence and presence of cations, which have been described in detail in a previous work.<sup>25</sup> Figure 3.1b shows the blank cyclic voltammogram of  $\text{Pd}_{\text{ML}}\text{Pt}(111)$  in a pH 3 electrolyte with 1 mM  $\text{KClO}_4$  in the presence of  $\text{CO}_2$ .  $\text{CO}_2$  leads to the presence and adsorption of bicarbonate ( $\text{HCO}_3^-$ ) on  $\text{Pd}_{\text{ML}}\text{Pt}(111)$ . As shown in black curve in Figure 3.1b, the peak at +0.31  $V_{\text{RHE}}$  increases in sharpness (compared with the peak at +0.21  $V_{\text{RHE}}$ ), while the stronger bicarbonate adsorption, compared to perchlorate adsorption, lowers the current density in the potential window from +0.35 to +0.9  $V_{\text{RHE}}$ , *i.e.* it suppresses  $\ast\text{OH}$  and/or  $\ast\text{O}$  adsorption.<sup>25</sup> Importantly, below +0.1  $V_{\text{RHE}}$ , the  $\text{Pd}_{\text{ML}}\text{Pt}(111)$  electrode is fully covered with adsorbed hydrogen.

Voltammetry is also used to estimate the amount of adsorbed carbon monoxide ( $\ast\text{CO}$ ) formed on the  $\text{Pd}_{\text{ML}}\text{Pt}(111)$  electrode during  $\text{CO}_2\text{RR}$  experiments. To this end, we use CO stripping voltammetry. The red curve in Figure 3.1b shows the oxidative stripping voltammogram of a full saturation coverage of  $\ast\text{CO}$  obtained from  $\text{CO}_2\text{RR}$  on the  $\text{Pd}_{\text{ML}}\text{Pt}(111)$  electrode, which corresponds to ca. 0.75 ML in terms of available Pd surface atoms.  $\ast\text{CO}$  remains on the surface of the  $\text{Pd}_{\text{ML}}\text{Pt}(111)$  electrode after  $\text{CO}_2\text{RR}$ , which blocks the electrode surface and results in a low current observed in the region between +0.05 and +0.35  $V_{\text{RHE}}$  at the beginning of oxidative stripping voltammogram. With more positive potential, CO oxidation peaks between 0.65  $V_{\text{RHE}}$  and 0.90  $V_{\text{RHE}}$  are observed. Upon oxidation of adsorbed  $\ast\text{CO}$ , the

typical CV features in pH 3 electrolyte are again observed in the negative going scan. This means that the Pd<sub>ML</sub>Pt(111) electrode should still be intact and can be used again for a new experiment.

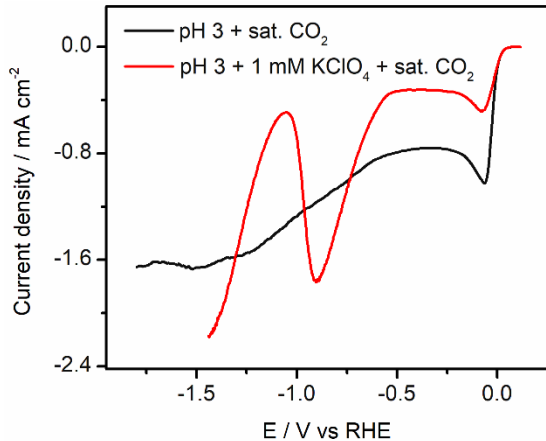


**Figure 3.2** Linear Sweep Voltammetry of Pd<sub>ML</sub>Pt(111) in CO<sub>2</sub> saturated pH 3 electrolytes in the absence (black) and presence of 1mM KClO<sub>4</sub> (red). Scan rate: 10 mV/s.

**Cation effect on HCOOH and CO formation during CO<sub>2</sub>RR.** After surface characterization, we studied the cation concentration effect on formic acid and CO formation during CO<sub>2</sub>RR on Pd<sub>ML</sub>Pt(111) in pH 3 electrolytes. The CO<sub>2</sub>RR experiments were carried out by linear sweep voltammetry, scanning from +0.07 V<sub>RHE</sub> to different negative vertex potentials at 1 mV s<sup>-1</sup>. HCOOH and CO production during CO<sub>2</sub>RR was obtained from online HPLC and CO stripping voltammetry respectively, as introduced in the experimental section and the previous section. Figure 3.2 shows the corresponding linear sweep voltammograms, obtained at higher scan rate (10 mV/s). The meaning of the effect of 1 mM KClO<sub>4</sub> on the voltammetry is explained in the following sections. All CO stripping voltammograms obtained in this work are shown in Figures B.3 - B.7 in the Supporting Information.

Figure 3.3 shows the obtained CO coverage and HCOOH production during CO<sub>2</sub>RR on Pd<sub>ML</sub>Pt(111) as a function of potential in a pH 3 electrolyte, in the presence of 0, 1 and 99 mM KClO<sub>4</sub> respectively (additional data for pH 3 with 5 and 10 mM KClO<sub>4</sub> are shown in Figures B.5 and B.6, a comparison is provided in Figure B.8). Figure 3.3a shows CO and HCOOH production in the absence of metal cations. CO is observed on Pd<sub>ML</sub>Pt(111) in the



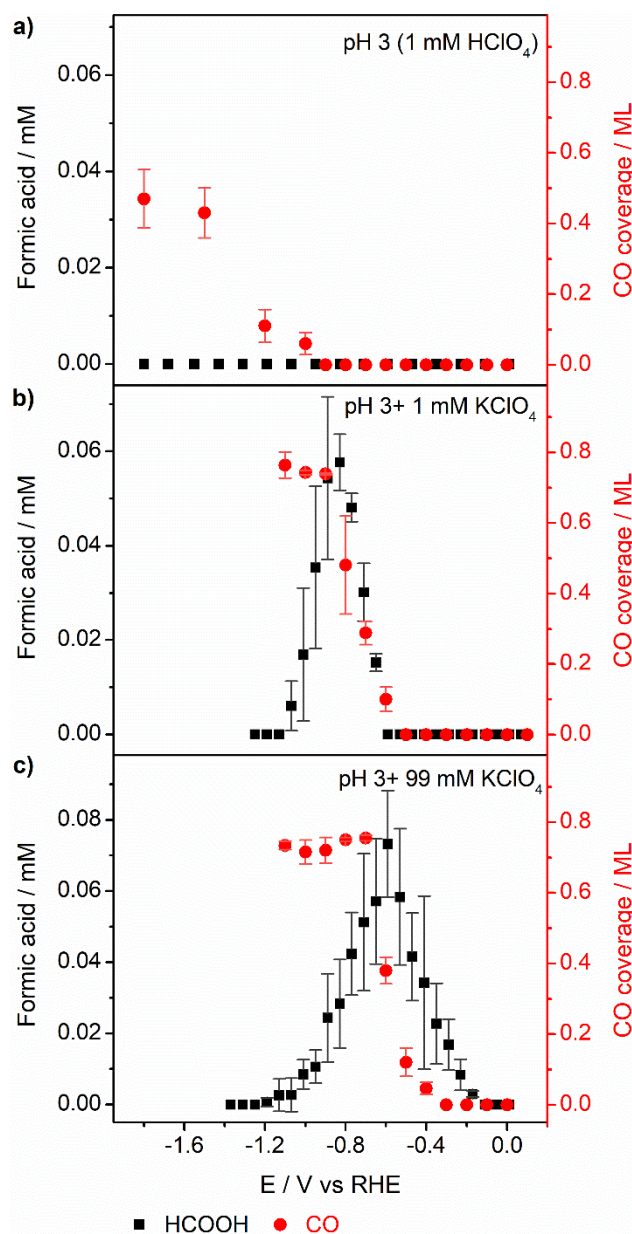


**Figure 3.3** Cation concentration effect on CO<sub>2</sub>RR on Pd<sub>ML</sub>Pt(111). CO coverage and HCOOH formation during CO<sub>2</sub>RR obtained in CO<sub>2</sub> saturated pH 3 electrolytes a) in the absence of metal cations, in the presence of b) 1 mM KClO<sub>4</sub> and c) 99 mM KClO<sub>4</sub>. Error bars are standard deviations based on three independent measurements.

absence of metal cations, albeit at a considerably negative onset potential of -1.0 V<sub>RHE</sub>. The obtained maximum CO coverage under these conditions is ca. 0.4 ML at -1.8 V<sub>RHE</sub>, which is much lower than the saturation CO coverage reported before.<sup>16</sup> Remarkably, no HCOOH production was observed in the absence of metal cations. To verify this result, 10 min of

chronoamperometry was also carried out at  $-1.2\text{ V}_{\text{RHE}}$  with online HPLC, and indeed no HCOOH was detected (see Figure B.3b). Although reporting Faradaic Efficiencies (FE) is not the goal of this work, note that the amount of HCOOH formed is below the limit of detection for HPLC, whereas that of CO (determined by stripping voltammetry) is not, at the more negative potentials. However, the CO that we detect is adsorbed CO, not dissolved CO. We have no (voltammetric) evidence for the formation of dissolved CO under the conditions of our experiment.

Figures 3.3b, c show the same experiments with different concentrations of metal cations in the electrolyte. Figure 3.3b shows CO and HCOOH formation during CO<sub>2</sub>RR in the electrolyte with the presence of 1 mM KClO<sub>4</sub>. \*CO is produced with an onset potential of  $-0.6\text{ V}_{\text{RHE}}$ , whereas the formation of HCOOH was observed with a slightly more negative onset potential of  $-0.65\text{ V}_{\text{RHE}}$ . With the increasingly negative-going potential, \*CO coverage and HCOOH formation keep increasing until a high \*CO coverage (ca. 0.74 ML) is reached at  $-0.9\text{ V}$ . From  $-0.9\text{ V}_{\text{RHE}}$  and more negative potentials, the \*CO coverage remains constant while HCOOH formation drops due to the high coverage of \*CO on the surface. Compared with CO<sub>2</sub>RR in pure pH 3 electrolyte, it is clear that the onset potential of CO<sub>2</sub>RR is less negative in the presence of 1mM KClO<sub>4</sub>. With the increase of the cation concentration (99 mM KClO<sub>4</sub>, Figure 3.3c), CO formation starts at  $-0.4\text{ V}_{\text{RHE}}$  whereas HCOOH is produced from  $-0.2\text{ V}_{\text{RHE}}$ . This result shows that cations have a stronger effect on HCOOH production compared to \*CO formation, yielding a lower overpotential for HCOOH in the presence of a high cation concentration. This result is consistent with HCOOH as the major CO<sub>2</sub>RR product (with minor CO poisoning) at low overpotentials, as shown in previous work on nanoparticulate Pd. Note that on nanoparticulate Pd, the current due to H intercalation should be minimal, at least during long-term electrolysis experiments.<sup>3</sup>

Knowing the effect of cations of CO<sub>2</sub>RR on Pd<sub>ML</sub>Pt(111), we can now understand the voltammograms in Figure 3.2. The reduction wave between 0 and  $-0.5\text{ V}_{\text{RHE}}$  is due to the (diffusion-limited) reduction of protons (their concentration being ca. 1 mM at pH=3). The current density is higher in the absence of cations (black curve) as under these conditions,

protons are also transported to the surface by migration, in addition to diffusion.<sup>42-43</sup> In the presence of cations (red curve), CO<sub>2</sub> reduction starts after -0.5 V<sub>RHE</sub>. The corresponding peak is completely absent when cations are lacking. The peak shape is caused by the fact that at potentials more negative than -0.9 V<sub>RHE</sub>, adsorbed CO is formed and the production of HCOOH is inhibited. To confirm the origin of the peak at -0.8 V<sub>RHE</sub>, linear sweep voltammetry was carried out under the same experimental conditions in argon-purged pH 3 electrolyte. The corresponding linear sweep voltammogram is shown in Figure B.2. No peak was observed in pH 3 electrolyte with the presence of 1 mM KClO<sub>4</sub>, confirming that the peak at -0.8 V<sub>RHE</sub> is due to CO<sub>2</sub> reduction.

Interestingly, at potentials more negative than -1.1 V<sub>RHE</sub>, the solution with cations clearly shows the reduction of water. There is no such clear water reduction current in the absence of cations. One could interpret this as an important promoting role of cations of water reduction (an effect which is known),<sup>44</sup> but one should also be aware that in the absence of supporting electrolyte, there are no ions available to carry such a reduction current. Therefore, we cannot claim that water reduction does not occur without cations, only that cations promote water reduction.

Furthermore, we also studied the effect of cation identity on CO and HCOOH formation during CO<sub>2</sub>RR on Pd<sub>ML</sub>Pt(111). Figure 3.4 shows the obtained CO coverage and HCOOH production during CO<sub>2</sub>RR as a function of potential in pH 3 electrolytes in the presence of 99mM LiClO<sub>4</sub> and NaClO<sub>4</sub>, respectively. We observe that the CO coverage obtained from pH 3 electrolyte containing 99 mM LiClO<sub>4</sub> is ca. 0.5 ML, which is less than the coverage obtained in the pH 3 electrolyte containing 99 mM NaClO<sub>4</sub> or KClO<sub>4</sub>. Moreover, we observe a correlation between CO<sub>2</sub>RR activity and the cation identity. The activity for CO and HCOOH formation on Pd<sub>ML</sub>Pt(111) increases in the order Li<sup>+</sup> < Na<sup>+</sup> < K<sup>+</sup>, following the ability of these species to accumulate near the surface.<sup>22, 36</sup> These results confirm the specific importance of the nature of the metal cations, and that in general, a strongly hydrated cation such as Li<sup>+</sup> has a lower promoting effect on CO<sub>2</sub> activation compared to more weakly hydrated cations.

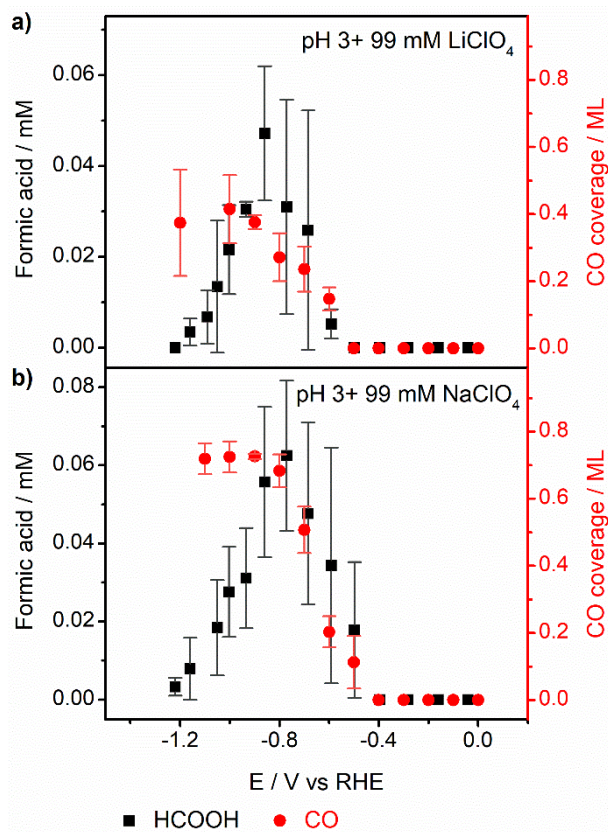


**Figure 3.4** Cation identity effect on Pd<sub>ML</sub>Pt(111). CO coverage and HCOOH formation during CO<sub>2</sub>RR obtained in CO<sub>2</sub> saturated pH 3 electrolytes containing 99 mM a) LiClO<sub>4</sub> and b) NaClO<sub>4</sub>. Error bars are standard deviations based on three independent measurements.

**Computational model.** To gain additional insights into the mechanism underlying the observed cation effects on HCOOH and CO formation during CO<sub>2</sub>RR, we carried out complementary density functional theory (DFT) simulations. According to the state-of-the-art, the mechanisms for the formation of formic acid and CO from CO<sub>2</sub>RR encompass several elementary steps. For CO<sub>2</sub> reduction to formic acid on Pd, it is now agreed that the most relevant step is the adsorption of hydrogen as hydride (\*H<sup>δ-</sup>),<sup>3, 16</sup> which performs a nucleophilic attack on the positively charged carbon of a nearby CO<sub>2</sub> in solution. Depending on the bulk solution pH, the generated formate becomes protonated to formic acid. Instead, the route towards CO requires the adsorption of CO<sub>2</sub> *via* the C atom, with subsequently one of the terminal O atoms becoming hydrogenated until water splits off, leaving adsorbed \*CO on the catalyst surface.

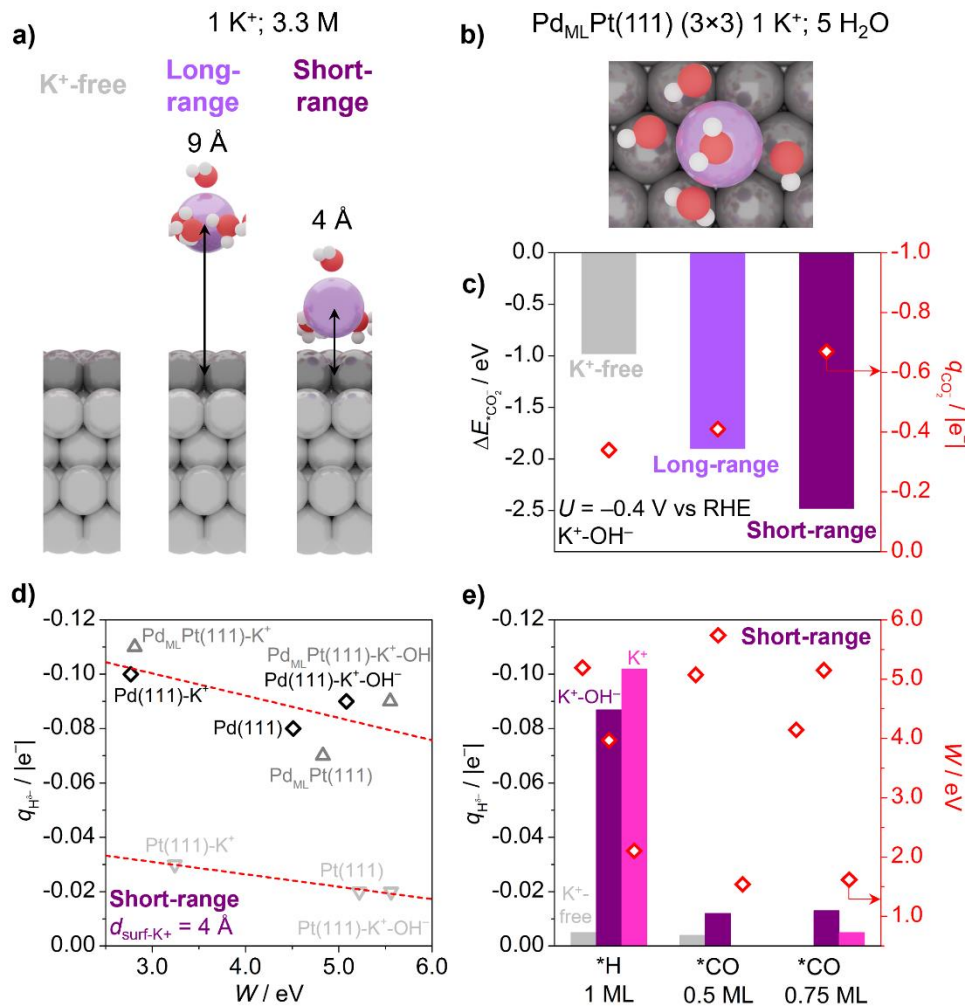
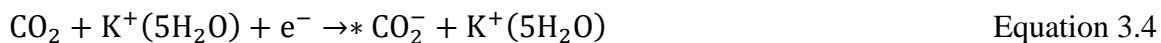


**Figure 3.5** Cation promotional effect on CO<sub>2</sub> adsorption and formation of a surface hydride (\*H<sup>δ-</sup>). a) Side and b) top views of the Pd<sub>ML</sub>Pt(111) (3×3)-1K<sup>+</sup>(5 H<sub>2</sub>O) models. c) CO<sub>2</sub><sup>-</sup> formation energy at  $U = -0.4$  V vs RHE (left y-axis) and excess charge on CO<sub>2</sub> unit (right y-axis) for a neutral Pd<sub>ML</sub>Pt(111) (3×3)-1K<sup>+</sup>(5 H<sub>2</sub>O) supercell (K<sup>+</sup>-OH<sup>-</sup> couple). d) Correlation between H<sup>δ-</sup> Bader charges and work function ( $W$ ) of Pd(111) (3×3), Pd<sub>ML</sub>Pt(111) (3×3), and Pt(111) (3×3), respectively black, dark and light gray data points. For both charged (K<sup>+</sup>) and neutral supercells (K<sup>+</sup>-OH<sup>-</sup>), the cation-surface distance was 4 Å. e) H<sup>δ-</sup> Bader charges (left y-axis) and metal work function (red data points, right y-axis) for Pd<sub>ML</sub>Pt(111) (3×3) at various \*H and \*CO coverages. Gray, purple, and magenta columns indicate respectively the K<sup>+</sup>-free, neutral (K<sup>+</sup>-OH<sup>-</sup>), and charged (K<sup>+</sup>) supercells. When present, the cation was placed 4 Å far away from the surface.

To model these key reaction steps, we carried out DFT simulations with the PBE-D2 functional.<sup>30-33</sup> To simulate the experimental surface without cation in the electrolyte, we chose a (3×3) Pd<sub>ML</sub>Pt(111) supercell, composed of 1 Pd monolayer on top of 4 Pt layers, of which the two lower layers were kept fixed to resemble the bulk. Further, to assess the role of metal cations, we included 1 K<sup>+</sup> with 5 coordinated H<sub>2</sub>O molecules within its solvation shell in the simulation cell.<sup>36</sup> Since the volume of the solvation layer accounts for 0.50 nm<sup>3</sup> (7 Å thickness), the surface cation concentration was equivalent to 3.3 M. K<sup>+</sup> was inserted at two fixed distances either 4 Å or 9 Å from the Pd<sub>ML</sub>Pt(111) surface (Figure 3.5a-b) to decouple short- and long-range cation effects on reaction intermediates. To avoid artificial interactions between periodic images, the vacuum thickness extended for 10 Å beyond the Pd<sub>ML</sub>Pt(111) surface layer for the cation-free case, and beyond the outermost water molecule if the cation was present, respectively.<sup>45</sup> Since we recently highlighted the importance of charged simulation cells to model cation effects,<sup>37</sup> we considered here both a cell with 1 excess electron (K<sup>+</sup> without OH<sup>-</sup>) and a neutral cell (K<sup>+</sup> with OH<sup>-</sup>). In this second case, we neutralized K<sup>+</sup> *via* a OH<sup>-</sup> formed by removing a hydrogen from one of the H<sub>2</sub>O molecules.<sup>22</sup> Since excess electrons in the simulation cell led to significant variations in the metal work function  $W$  and consequently in the electrostatic potential  $\Phi$  along the simulation cell (Figures B.9 and B.10), when assessing the thermodynamics of CO<sub>2</sub> activation (Figure 3.5c), we opted for neutral supercells (K<sup>+</sup>-OH<sup>-</sup> couple) to keep  $W$  constant (as shown in Table B.1).

**Mechanism of cation effect on CO<sub>2</sub> activation.** CO<sub>2</sub> activation is often assumed as the rate-determining step for CO<sub>2</sub>RR on transition metals.<sup>22</sup> To assess the potential role of cations on CO<sub>2</sub> reduction to CO, we estimated the energy required for activating CO<sub>2</sub> on Pd<sub>ML</sub>Pt(111) (3×3) for the cation-free case (see Equation 3.3) and in presence of cations at 4 and 9 Å far away from the surface (Equation 3.4). We corrected the DFT energy for a potential-dependent term calculated at  $U = -0.4$  V vs RHE (pH = 3), the observed onset potential for CO<sub>2</sub> reduction to CO (Figure 3.3c). Such potential-dependent term was obtained by tuning the metal work function in line with the approach suggested by Chan and Nørskov (Refs. <sup>40-41</sup>), as shown in section: Effect of Applied Electric Potential on Formation Energies, Equations 3.1 and 3.2, Tables B.1 and B.2). In Equation 3.5,  $\Delta q$  represents the change in electronic surface

charge for Pd<sub>ML</sub>Pt(111) (3×3) between the final (surface + \*CO<sub>2</sub><sup>-</sup>) and initial (surface + CO<sub>2</sub>) state, thus it is equal to -1 e<sup>-</sup>.



$$\Delta E_{* \text{CO}_2^-}(\Phi_{-0.4 \text{ V vs RHE}}) = \Delta E_{* \text{CO}_2^-}(\Phi_{\text{surf}}) + \Delta q(\Phi_{\text{surf}} - \Phi_{-0.4 \text{ V vs RHE}}) \quad \text{Equation 3.5}$$

In the presence of proximal metal cation ( $d_{\text{K}^+-\text{surf}} = 4 \text{ \AA}$ ), the K<sup>+</sup> coordinates to the free oxygen of the CO<sub>2</sub> molecule, leading to a strong CO<sub>2</sub> binding ( $\Delta E = -2.5 \text{ eV}$ , as reported in Figure 3.5c). Instead, for a cation-surface distance of 9 Å, we observe a weaker \*CO<sub>2</sub> adsorption energy, around -1.9 eV. In agreement with experimental results (see Figure 3.3a), CO<sub>2</sub> activation occurs also for the cation-free case, being exothermic by around -1.0 eV at -0.4 V vs RHE. Additionally, our results show that metal cations enhance the electron transfer from Pd<sub>ML</sub>Pt(111) to adsorbed CO<sub>2</sub> (see right y-axis in Figure 3.5c). In fact, the CO<sub>2</sub> Bader charge ( $q_{\text{CO}_2}$ ) is -0.67 |e<sup>-</sup>| for  $d_{\text{K}^+-\text{surf}} = 4 \text{ \AA}$ , while decreases to -0.41 |e<sup>-</sup>| if the cation is far from the surface ( $d_{\text{K}^+-\text{surf}} = 9 \text{ \AA}$ ).  $q_{\text{CO}_2}$  further reduces to -0.34 |e<sup>-</sup>| in absence of metal cations in the simulation cell. Cation-promoted electron transfer to CO<sub>2</sub> was confirmed as well on Pd(111) (3×3) and Pt(111) (3×3), see Figure B.11.

**Mechanism of cation effect on hydride formation.** Moving on to HCOOH selectivity, we assess the effect of cations on the formation of adsorbed hydride (\*H<sup>δ-</sup>). As shown in Figure 3.5d, the Bader charge of adsorbed hydride (\*H<sup>δ-</sup>) correlates with the work function of Pd(111), Pd<sub>ML</sub>Pt(111), and Pt(111), in line with previous findings in Ref. <sup>3, 16</sup>. In turn, the metal work function decreases in presence of neighboring K<sup>+</sup> due to increased cation-induced polarization of the surface electronic density, favoring the formation of surface hydrides. Such phenomenon may be also expressed in terms of metal *d*-band center. For materials with low *d*-band center, such as Pt(111) ( $\epsilon_d \sim -2.0 \text{ eV}$ ), the limited electronic density available at the surface prevents an effective formation of a hydride ( $\delta^- \sim -0.02 |e^-|$ ). Instead, on metals characterized by higher values of *d*-band center ( $\epsilon_d \sim -1.5 \text{ eV}$ , or low work function), such as

Pd(111) and Pd<sub>ML</sub>Pt(111), more electronic density is available at the surface, enabling the formation of surface hydrides ( $\delta^- \sim -0.10$  |e<sup>-</sup>|). A previous experimental study showed a strong correlation between Pd content and HCOOH/HCOO<sup>-</sup> selectivity on Pt-Pd nanoparticles and aerogels, while pure Pt was reported not able to reduce CO<sub>2</sub> to HCOOH/HCOO<sup>-</sup>.<sup>16, 27, 46</sup> We here confirm that CO<sub>2</sub>RR to HCOOH requires hydride species on PdPt catalysts, which occur only for suitable surface charging, *i.e.* appropriate filling of *d*-band states or induced by neighboring cation. In fact, we observe that \*H<sup>δ-</sup> Bader charges correlate with the K<sup>+</sup>-induced electric field (proportional to  $q^{K^+}/r_{K^+H}^2$ ), as shown in Figure B.12 and Table B.3. Higher intensities of cation-induced electric field lead to increased polarization at the surface<sup>17</sup>, which enhances the hydridic character of \*H.

Figure 3.5d suggests that surface hydrides should also form in absence of cations, which is at odds with experimental results on HCOOH selectivity for Pd<sub>ML</sub>Pt(111) (Figure 3.3a). Thus, we upgraded our model to more realistic conditions, *i.e.* high \*H and \*CO coverages, retrieving input geometries from a previous theoretical study.<sup>47</sup> Remarkably, hydrides are preserved at 1 ML \*H coverage only in presence of neighboring cations, while  $\delta^- > -0.01$  |e<sup>-</sup>| in the cation-free case (Figure 3.5e). High CO coverages (0.5 and 0.75 ML) hinder the formation of surface hydrides both in absence and presence of alkali cations. Both insights can be rationalized by the upshift of Pd<sub>ML</sub>Pt(111) work function at high adsorbate coverages, partially balanced by the downshift in presence of neighboring cation at high \*H coverage (Figure 3.5e). Other factors may also contribute to the selective reduction of CO<sub>2</sub> to HCOOH on Pd<sub>ML</sub>Pt(111) at mild negative potentials. Considering the case of outer-sphere CO<sub>2</sub> activation to HCOO<sup>-</sup> by alkali cations, proposed by Pidko *et al.*<sup>23</sup> on Ag(111), such coupling is exothermic for both neutral (K<sup>+</sup>-OH<sup>-</sup>) and charged (K<sup>+</sup>) cells (see Figure B.13) on Pd<sub>ML</sub>Pt(111) (3×3). Instead, for the cation free case, such process is endothermic by 0.2 eV. Nevertheless, in the case of adsorbed hydride transfer to physisorbed CO<sub>2</sub> at -0.4 V vs RHE, the cation contribution appears less critical. In fact, such step is almost thermoneutral (~0.1 eV) both in presence and absence of neighboring cations (Figure B.13).

### 3.3.2 Discussion



Our results show the crucial role of metal cations on HCOOH and CO formation during CO<sub>2</sub>RR on Pd<sub>ML</sub>Pt(111). Without metal cations, only limited CO<sub>2</sub> reduction to CO takes place.

<sup>22</sup> This result is slightly different from the previous work reported by our group for CO<sub>2</sub> activation to CO on Ag, Au, and Cu electrodes, for which cations are a necessary reaction partner. This difference must be due to the fact that palladium binds CO more strongly, and therefore, the activation barrier for CO formation is lower, such that even in the absence of cations, CO formation can take place. The activity towards HCOOH and CO improves with the increase of cation concentration, leading to the decreased onset potential of both products. Remarkably, Pd<sub>ML</sub>Pt(111) produces no HCOOH in the absence of cations while it is still somewhat active for \*CO formation. In the presence of a high cation concentration, the selectivity pattern reverses and HCOOH formation happens at a lower overpotential, suggesting a stronger cation effect on HCOOH formation than CO formation on Pd<sub>ML</sub>Pt(111). In a previous work, we have rationalized the role of \*H<sup>δ-</sup> on HCOO<sup>-</sup>/HCOOH formation on Pd surfaces and the dependence of hydridic character on the metal work function.<sup>16</sup> Hydrides are instrumental for reducing CO<sub>2</sub> to HCOO<sup>-</sup>/HCOOH on Pt-Pd catalysts through a nucleophilic attack on a nearby CO<sub>2</sub>.

The insights from our DFT simulations support the mechanism reported for CO vs HCOO<sup>-</sup>/HCOOH competition on Pd<sub>ML</sub>Pt(111),<sup>16</sup> complementing our previous observations on other transition metals (Ag, Au, Cu).<sup>22</sup> Neighboring cations ( $d_{K+-surf} = 4 \text{ \AA}$ ) enhance CO<sub>2</sub> activation by more than 1 eV at  $U = -0.4 \text{ V}_{RHE}$  vs the cation-free case, further facilitating the electron transfer to the CO<sub>2</sub> unit (CO<sub>2</sub> Bader charge of  $-0.67 |e^-|$ ). Regarding formic acid/formate selectivity, hydrides are effectively formed on materials with a low work function, such as Pd(111) and Pd<sub>ML</sub>Pt(111). These catalysts enable the transfer of surface electronic density to the adsorbate, while hydrides are not formed on catalysts with deep electronic states, such as Pt(111), which prevent the formic acid pathway. In case of a high \*H coverage, the cation-induced local electric field counterbalances the upshift of the metal work function due to the adsorbates, which instead hinder the formation of hydrides for the cation-free case. Such evidence rationalizes one of the most striking experimental observations in this work, *i.e.* the complete absence of HCOOH formation in the absence of cations.

In addition to  $^*\text{H}$  coverage effect, cation-induced outer-shell  $\text{CO}_2$  activation and short-range stabilization of  $\text{HCOO}^-$  may also aid in favoring  $\text{HCOOH}$  formation.<sup>23</sup> However, given the general agreement that  $\text{HCOOH}$  selectivity crucially depends on hydrides, we highlight here the stabilization of the hydridic character as the critical contribution of cations. We note that cations enhance the formation of surface hydrides and the hydride transfer to  $\text{CO}_2$  by inducing a further polarization of the  $\text{Pd-H}$  bond, in line with the conclusions of ref 17. Finally, during  $\text{CO}_2\text{RR}$ , the interfacial pH changes<sup>20, 48</sup>, which may impact interfacial reactivity. Previous reported work suggests a pH swing close to an Au electrode from bulk pH conditions to an interfacial pH around 10-12 during  $\text{CO}_2\text{RR}$  under highly reactive conditions.<sup>20, 48</sup> Cations have a small buffering capacity<sup>21</sup>, with an impact on the interfacial pH which can be measured.<sup>48</sup> This effect may be one of the factors contributing to our experimental results, however, it is hard to imagine that this relatively small effect would explain the observations shown in Figure 3.3.

### 3.4 Conclusions

We have studied the cation effect on  $\text{HCOOH}$  and  $\text{CO}$  formation during  $\text{CO}_2\text{RR}$  with a well-defined  $\text{Pt}(111)$  electrode with epitaxially grown  $\text{Pd}$  monolayer. The experiments show that cations have a stronger effect on  $\text{HCOOH}$  formation compared to  $^*\text{CO}$  formation. There is no  $\text{HCOOH}$  formation in the absence of cations though there is  $^*\text{CO}$  formation at high overpotentials. In the presence of a high cation concentration a lower overpotential for  $\text{HCOOH}$  formation is observed. Our DFT results help rationalize the experimental observations. Both  $\text{CO}$  and  $\text{HCOOH}$  formation pathways involve negatively charged intermediates, *i.e.* negatively charged adsorbed  $\text{CO}_2$  and adsorbed hydride, resp., whose formation is favored by the interaction with cations. The generation of hydrides is favored by a low metal work function (that correlates with an appropriate position of the metal  $d$ -band). The cation can further downshift the metal work function by inducing increased surface electronic density and thus promoting hydrides or sustaining the formation of hydrides at high  $^*\text{H}$  coverage. Consequently,  $\text{CO}_2$  reduction to formic acid takes place at mild applied potential. Instead, high  $\text{CO}$  coverages prevent the formation of hydrides both in presence and

absence of cations, causing the quick decrease of formic acid selectivity at high applied potential. As a final remark, since cation effects on CO<sub>2</sub>RR to HCOOH depend on both the cation accumulation at the surface (well described by cation acidity) and the induced electronic density at the surface, further studies to optimize electrolytes towards formic acid selectivity should target cations (or mixtures) with high induced electric field (*i.e.*  $\delta^+$ -favorable formation) and a relatively low acidity, beyond the current employed standard cations (Figure B.12, Table B.3).

Our study reveals once more that the search for optimized systems for CO<sub>2</sub>R should carefully tailor the design of both sides of the electrolyte/electrode interface, especially for HCOOH/HCOO<sup>-</sup> formation.

## References

1. Kuhl, K. P.; Cave, E. R.; Abram, D. N.; Jaramillo, T. F., New insights into the electrochemical reduction of carbon dioxide on metallic copper surfaces. *Energy Environ. Sci.* **2012**, *5* (5), 7050-7059.
2. Hatsukade, T.; Kuhl, K. P.; Cave, E. R.; Abram, D. N.; Jaramillo, T. F., Insights into the electrocatalytic reduction of CO<sub>2</sub> on metallic silver surfaces. *Phys. Chem. Chem. Phys.* **2014**, *16* (27), 13814-9.
3. Min, X.; Kanan, M. W., Pd-catalyzed electrohydrogenation of carbon dioxide to formate: high mass activity at low overpotential and identification of the deactivation pathway. *J. Am. Chem. Soc.* **2015**, *137* (14), 4701-8.
4. Cave, E. R.; Montoya, J. H.; Kuhl, K. P.; Abram, D. N.; Hatsukade, T.; Shi, C.; Hahn, C.; Nørskov, J. K.; Jaramillo, T. F., Electrochemical CO<sub>2</sub> reduction on Au surfaces: mechanistic aspects regarding the formation of major and minor products. *Phys. Chem. Chem. Phys.* **2017**, *19* (24), 15856-15863.
5. Cao, Z.; Kim, D.; Hong, D.; Yu, Y.; Xu, J.; Lin, S.; Wen, X.; Nichols, E. M.; Jeong, K.; Reimer, J. A.; Yang, P.; Chang, C. J., A Molecular Surface Functionalization Approach to Tuning Nanoparticle Electrocatalysts for Carbon Dioxide Reduction. *J. Am. Chem. Soc.* **2016**, *138* (26), 8120-5.
6. Zhang, X.; Li, J.; Li, Y. Y.; Jung, Y.; Kuang, Y.; Zhu, G.; Liang, Y.; Dai, H., Selective and High Current CO<sub>2</sub> Electro-Reduction to Multicarbon Products in Near-Neutral KCl Electrolytes. *J. Am. Chem. Soc.* **2021**, *143* (8), 3245-3255.
7. Yuan, X.; Chen, S.; Cheng, D.; Li, L.; Zhu, W.; Zhong, D.; Zhao, Z. J.; Li, J.; Wang, T.; Gong, J., Controllable Cu(0) -Cu(+) Sites for Electrocatalytic Reduction of Carbon Dioxide. *Angew. Chem. Int. Ed. Engl.* **2021**, *60* (28), 15344-15347.
8. Wang, X.; Klingan, K.; Klingenhof, M.; Moller, T.; Ferreira de Araujo, J.; Martens, I.; Bagger, A.; Jiang, S.; Rossmeisl, J.; Dau, H.; Strasser, P., Morphology and mechanism of highly selective Cu(II) oxide nanosheet catalysts for carbon dioxide electroreduction. *Nat. Commun.* **2021**, *12* (1), 1-12.
9. Wuttig, A.; Yaguchi, M.; Motobayashi, K.; Osawa, M.; Surendranath, Y., Inhibited proton transfer enhances Au-catalyzed CO<sub>2</sub>-to-fuels selectivity. *Proc. Natl. Acad. Sci. U.S.A.* **2016**, *113* (32), E4585-93.
10. Gao, D.; Zhou, H.; Wang, J.; Miao, S.; Yang, F.; Wang, G.; Wang, J.; Bao, X., Size-dependent electrocatalytic reduction of CO<sub>2</sub> over Pd nanoparticles. *J. Am. Chem. Soc.* **2015**, *137* (13), 4288-91.
11. Guo, R.-H.; Liu, C.-F.; Wei, T.-C.; Hu, C.-C., Electrochemical behavior of CO<sub>2</sub> reduction on palladium nanoparticles: Dependence of adsorbed CO on electrode potential. *Electrochem. Commun.* **2017**, *80*, 24-28.
12. Darby, M. T.; Sykes, E. C. H.; Michaelides, A.; Stamatakis, M., Carbon Monoxide Poisoning Resistance and Structural Stability of Single Atom Alloys. *Top. Catal.* **2018**, *61* (5), 428-438.
13. Arenz, M.; Stamenkovic, V.; Ross, P. N.; Markovic, N. M., Surface (electro-)chemistry on Pt(111) modified by a Pseudomorphic Pd monolayer. *Surf. Sci.* **2004**, *573* (1), 57-66.
14. Baldauf, M.; Kolb, D. M., Formic Acid Oxidation on Ultrathin Pd Films on Au(hkl) and Pt(hkl) Electrodes. *J. Phys. Chem.* **1996**, *100* (27), 11375-11381.
15. Chen, X.; Koper, M. T. M., Mass-transport-limited oxidation of formic acid on a Pd ML Pt(100) electrode in perchloric acid. *Electrochem. Commun.* **2017**, *82*, 155-158.
16. Chen, X.; Granda-Marulanda, L. P.; McCrum, I. T.; Koper, M. T. M., How palladium inhibits

CO poisoning during electrocatalytic formic acid oxidation and carbon dioxide reduction. *Nat. Commun.* **2022**, *13* (1), 38.

17. Wang, H.-X.; Toh, W. L.; Tang, B. Y.; Surendranath, Y., Metal surfaces catalyse polarization-dependent hydride transfer from H<sub>2</sub>. *Nat. Catal.* **2023**, *6* (4), 351-362.

18. Huang, B.; Rao, R. R.; You, S.; Hpone Myint, K.; Song, Y.; Wang, Y.; Ding, W.; Giordano, L.; Zhang, Y.; Wang, T.; Muy, S.; Katayama, Y.; Grossman, J. C.; Willard, A. P.; Xu, K.; Jiang, Y.; Shao-Horn, Y., Cation- and pH-Dependent Hydrogen Evolution and Oxidation Reaction Kinetics. *JACS Au* **2021**, *1* (10), 1674-1687.

19. Waagele, M. M.; Gunathunge, C. M.; Li, J.; Li, X., How cations affect the electric double layer and the rates and selectivity of electrocatalytic processes. *J. Chem. Phys.* **2019**, *151* (16), 160902.

20. Ayemoba, O.; Cuesta, A., Spectroscopic Evidence of Size-Dependent Buffering of Interfacial pH by Cation Hydrolysis during CO<sub>2</sub> Electroreduction. *ACS Appl. Mater. Interfaces* **2017**, *9* (33), 27377-27382.

21. Singh, M. R.; Kwon, Y.; Lum, Y.; Ager, J. W., 3rd; Bell, A. T., Hydrolysis of Electrolyte Cations Enhances the Electrochemical Reduction of CO<sub>2</sub> over Ag and Cu. *J. Am. Chem. Soc.* **2016**, *138* (39), 13006-13012.

22. Monteiro, M. C.; Dattila, F.; Hagedoorn, B.; García-Muelas, R.; López, N.; Koper, M., Absence of CO<sub>2</sub> electroreduction on copper, gold and silver electrodes without metal cations in solution. *Nat. Catal.* **2021**, *4* (8), 654-662.

23. Sinha, V.; Khramenkova, E.; Pidko, E. A., Solvent-mediated outer-sphere CO<sub>2</sub> electroreduction mechanism over the Ag111 surface. *Chem. Sci.* **2022**.

24. Clavilier, J.; Armand, D.; Sun, S. G.; Petit, M., Electrochemical adsorption behaviour of platinum stepped surfaces in sulphuric acid solutions. *J. Electroanal. Chem. Interfacial Electrochem.* **1986**, *205* (1-2), 267-277.

25. Chen, X.; Granda-Marulanda, L. P.; McCrum, I. T.; Koper, M. T. M., Adsorption processes on a Pd monolayer-modified Pt(111) electrode. *Chem Sci* **2020**, *11* (6), 1703-1713.

26. López-Cudero, A.; Cuesta, A.; Gutiérrez, C., Potential dependence of the saturation CO coverage of Pt electrodes: The origin of the pre-peak in CO-stripping voltammograms. Part 1: Pt(111). *J. Electroanal. Chem.* **2005**, *579* (1), 1-12.

27. Kortlever, R.; Peters, I.; Koper, S.; Koper, M. T. M., Electrochemical CO<sub>2</sub> Reduction to Formic Acid at Low Overpotential and with High Faradaic Efficiency on Carbon-Supported Bimetallic Pd-Pt Nanoparticles. *ACS Catal.* **2015**, *5* (7), 3916-3923.

28. Kresse, G.; Furthmüller, J., Efficient iterative schemes for ab initio total-energy calculations using a plane-wave basis set. *Phys. Rev. B: Condens. Matter* **1996**, *54* (16), 11169-11186.

29. Kresse, G.; Furthmüller, J., Efficiency of ab-initio total energy calculations for metals and semiconductors using a plane-wave basis set. *Comput. Mater. Sci.* **1996**, *6* (1), 15-50.

30. Perdew, J. P.; Burke, K.; Ernzerhof, M., Generalized Gradient Approximation Made Simple. *Phys. Rev. Lett.* **1996**, *77* (18), 3865-3868.

31. Grimme, S., Semiempirical GGA-type density functional constructed with a long-range dispersion correction. *J. Comput. Chem.* **2006**, *27* (15), 1787-99.

32. Bucko, T.; Hafner, J.; Lebegue, S.; Angyan, J. G., Improved description of the structure of molecular and layered crystals: ab initio DFT calculations with van der Waals corrections. *J. Phys. Chem. A* **2010**, *114* (43), 11814-24.

33. Almora-Barrios, N.; Carchini, G.; Blonski, P.; Lopez, N., Costless Derivation of Dispersion

Coefficients for Metal Surfaces. *J. Chem. Theory Comput.* **2014**, *10* (11), 5002-9.

34. Kresse, G.; Joubert, D., From ultrasoft pseudopotentials to the projector augmented-wave method. *Phys. Rev. B* **1999**, *59* (3), 1758-1775.
35. Blochl, P. E., Projector augmented-wave method. *Phys. Rev. B: Condens. Matter* **1994**, *50* (24), 17953-17979.
36. Monteiro, M. C. O.; Dattila, F.; Lopez, N.; Koper, M. T. M., The Role of Cation Acidity on the Competition between Hydrogen Evolution and CO<sub>2</sub> Reduction on Gold Electrodes. *J. Am. Chem. Soc.* **2022**, *144* (4), 1589-1602.
37. Dattila, F.; Monteiro, M. C. O.; Koper, M. T. M.; López, N., Reply to: On the role of metal cations in CO<sub>2</sub> electrocatalytic reduction. *Nat. Catal.* **2022**, *5* (11), 979-981.
38. Makov, G.; Payne, M. C., Periodic boundary conditions in ab initio calculations. *Phys. Rev. B: Condens. Matter* **1995**, *51* (7), 4014-4022.
39. Marcus, Y., Ionic radii in aqueous solutions. *Chem. Rev.* **1988**, *88* (8), 1475-1498.
40. Chan, K.; Nørskov, J. K., Electrochemical Barriers Made Simple. *J. Phys. Chem. Lett.* **2015**, *6* (14), 2663-2668.
41. Chan, K.; Nørskov, J. K., Potential Dependence of Electrochemical Barriers from ab Initio Calculations. *J. Phys. Chem. Lett.* **2016**, *7* (9), 1686-1690.
42. Daniele, S.; Baldo, M. A.; Corbetta, M.; Mazzocchin, G. A., Linear sweep and cyclic voltammetry for metal deposition at solid and mercury microelectrodes from solutions with and without supporting electrolyte. *J. Electroanal. Chem.* **1994**, *379* (1-2), 261-270.
43. Bard, A. J.; Faulkner, L. R.; White, H. S., *Electrochemical Methods: Fundamentals and Applications*. Wiley: 2022.
44. Goyal, A.; Koper, M. T. M., The Interrelated Effect of Cations and Electrolyte pH on the Hydrogen Evolution Reaction on Gold Electrodes in Alkaline Media. *Angew. Chem. Int. Ed. Engl.* **2021**, *60* (24), 13452-13462.
45. Bellarosa, L.; Garcia-Muelas, R.; Revilla-Lopez, G.; Lopez, N., Diversity at the Water-Metal Interface: Metal, Water Thickness, and Confinement Effects. *ACS Cent. Sci.* **2016**, *2* (2), 109-116.
46. Diercks, J. S.; Georgi, M.; Herranz, J.; Diklič, N.; Chauhan, P.; Clark, A. H.; Hübner, R.; Faisnel, A.; Chen, Q.; Nachtegaal, M.; Eychmüller, A.; Schmidt, T. J., CO<sub>2</sub> Electroreduction on Unsupported PdPt Aerogels: Effects of Alloying and Surface Composition on Product Selectivity. *ACS Appl. Energy Mater.* **2022**, *5* (7), 8460-8471.
47. Sumaria, V.; Nguyen, L.; Tao, F. F.; Sautet, P., Optimal Packing of CO at a High Coverage on Pt(100) and Pt(111) Surfaces. *ACS Catal.* **2020**, *10* (16), 9533-9544.
48. Liu, X.; Monteiro, M. C. O.; Koper, M. T. M., Interfacial pH measurements during CO<sub>2</sub> reduction on gold using a rotating ring-disk electrode. *Phys. Chem. Chem. Phys.* **2023**, *25* (4), 2897-2906.



## **Chapter 4**

### **The Role of Cations in Hydrogen Evolution Reaction on a Platinum Electrode in Mildly Acidic Media**

This chapter is based on:

Ye, C.; Liu, X.; Koper, M. T. M. *Eletrochem. Commun.* **2024**, 166, 107784



**Abstract:** In this work, we study the influence of cation concentration and identity on the hydrogen evolution reaction (HER) on polycrystalline platinum (Pt) electrode in pH 3 electrolytes. Our observations indicate that cations in the electrolyte do not affect proton reduction at low potentials. However, an increase in cation concentration significantly enhances water reduction. Simultaneously, we identify a non-negligible migration current under mass transport limited conditions in electrolytes with low cation concentration. To separate migration effects from specific cation-promotion effects on HER, we carried out further experiments with electrolytes with mixtures of  $\text{Li}^+$  and  $\text{K}^+$  cations. Our results show that, adding strongly hydrated cations ( $\text{Li}^+$ ) to a  $\text{K}^+$ -containing electrolyte leads to a less negative onset potential of water reduction. Interfacial pH measurements reveal a same interfacial pH at the platinum electrode in pH 3 in the presence of 80 mM  $\text{LiClO}_4$  and  $\text{KClO}_4$ , respectively, at potentials where water reduction occurs. Based on these results, we suggest that under the current conditions, the strongly hydrated cations ( $\text{Li}^+$ ) promote water dissociation on the Pt electrode more favorably in comparison with the more weakly hydrated cations ( $\text{K}^+$ ).

### 4.1 Introduction

Catalyzing water splitting, specifically water reduction to produce hydrogen, stands at the forefront of electrochemical research due to its fundamental significance and profound implications for a sustainable energy future. Extensive work has been dedicated to develop efficient catalysts and to gain mechanistic insights of the hydrogen evolution reaction process.<sup>1-13</sup> Traditionally, the significant variations in HER rates (up to few orders of magnitude) observed on different electrode materials have been correlated to differences in the free energy of hydrogen adsorption.<sup>14-15</sup> However, this adsorption energy-based descriptor has certain limitations, notably in its inability to describe the sluggish kinetics of HER in alkaline media,<sup>9, 16</sup> where water dissociation is a prerequisite for generating adsorbed hydrogen. Further, it is crucial to note that the electrochemical environment at the metal-electrolyte interface profoundly influences HER activity under alkaline conditions. Consequently, other descriptors, which extend beyond mere adsorption energies, have gained attention. These include interfacial descriptors, such as the interfacial field strength, the oxophilicity of the surface sites and the cation solvation energy, all of which contribute to a more comprehensive understanding of the HER mechanism.<sup>2, 5, 8, 17-18</sup> In particular, these descriptors capture the delicate balance between the charge transfer-induced water dissociation step ( $H_2O + e^- + * \rightarrow H-* + OH^-$ ), the favorable/unfavorable interactions of the dissociation products with the surface ( $H_{ad}$  and  $OH_{ad}$ ) and/or concomitant rates of the  $H_{ad}$  recombination step ( $H_2$  production) and desorption of  $OH_{ad}$ , thereby influencing HER kinetics in alkaline media.

Metal cations in the electrolyte have been shown to have a significant effect on HER activity in alkaline media. Strmcnik et al have shown that HER kinetics on transition metal hydroxide modified Pt electrodes improves in  $Li^+$  containing electrolytes, which they attribute to the stabilizing effect of  $Li^+$  ions on the adsorbed hydroxyl ( $*OH-cat^+$ ) species at the interface.<sup>19-20</sup> Using a similar system, Liu et al suggest that the driving force for OH desorption is larger for  $Li^+$  than for  $Na^+$  and  $K^+$ , thereby giving rise to the HER activity decreasing in the order  $LiOH > NaOH > KOH$  at pH 13.<sup>21</sup> These studies attributed the promotion of the

electrochemical water dissociation step to favorable cation-water interactions. However, these descriptors fail to elucidate the inverted activity trend ( $K^+ > Na^+ > Li^+$ ) observed on a gold electrode in 0.1 M XOH.<sup>22</sup> Also, increasing  $Na^+$  cation concentration significantly enhances HER activity on a gold electrode up to pH 11 while the opposite trends have been observed at a higher pH (pH > 12).<sup>9</sup> In the latter work, the enhanced HER activity was linked to favorable interaction of the cation with the dissociating water molecule ( $*H-OH^{\delta-}-cat^+$ ), resulting from the increased near-surface cation concentration due to the local field strength.<sup>9, 12</sup> The decreased HER activity at high pH was attributed to a blockage or crowding effect caused by cation accumulation at the interface.<sup>9, 12</sup> These findings underscore the convoluted role of different interfacial parameters in tuning the activity of HER on a given surface in alkaline media.

Understanding the activity trend for the HER is also crucial for the development of other renewable energy technologies, such as electrochemical carbon dioxide reduction ( $CO_2RR$ ), where HER acts as a competing side reaction.<sup>13, 23-25</sup> Conventionally,  $CO_2RR$  electrolyzers have utilized neutral and alkaline electrolyte. However, recent studies highlight the potential of achieving high selectivity for  $CO_2RR$  products in acidic media.<sup>26-30</sup> Although the fast kinetics of the proton reduction remains a concern for  $CO_2RR$  in acidic media, it is noteworthy that the interfacial pH near the catalyst depends on specific reaction conditions. Liu et al. have shown a potentially high alkaline interfacial pH at a Au disk electrode during  $CO_2RR$  in pH 3 electrolytes.<sup>31</sup> The increased interfacial pH at electrodes with negative-going applied potential suggests water reduction over a broad potential window as the competitive reaction with  $CO_2RR$ .

When probing the effect of cation concentration on HER kinetics, one needs to consider the effect that cations may have on the migration current. Therefore, in this study, we have systematically investigated the influence of cation concentration and identity on the HER activity on a polycrystalline Pt electrode in pH 3 electrolytes using a background electrolyte mixture of two alkali cations,  $Li^+$  and  $K^+$ . In particular, we show that cations in the electrolyte do not influence proton reduction kinetically. However, with the increasing metal cation

concentration, the water reduction current significantly improves while the diffusion limited current due to proton reduction decreases. This proton migration current is effectively suppressed with excess supporting electrolyte. From the mixed cation electrolyte, we show a promotion effect of strongly hydrated cations ( $\text{Li}^+$ ) on the onset potential of water reduction. We also measure interfacial pH at the polycrystalline electrode during linear sweep voltammetry, revealing pH changes correlating with current density and reaction process. Overall, our study thereby provides valuable insights into the intricate interplay of cation effects on HER in mild acidic media.

## 4.2 Experimental Section

**Chemicals and cell preparation.** In this work, all electrolytes were prepared from  $\text{HClO}_4$  (Sigma-Aldrich, Ultrapure, 70%),  $\text{LiClO}_4$  (Sigma-Aldrich,  $\geq 99.99\%$  trace metal basis),  $\text{KClO}_4$  (Sigma-Aldrich,  $\geq 99.99\%$  trace metal basis),  $\text{H}_2\text{SO}_4$  (Merck, Suprapur, 96%) and ultrapure water (resistivity  $> 18.2 \text{ M}\Omega\cdot\text{cm}$ , Millipore Milli-Q). Prior to each experiment, all cell compartments were cleaned by storing them in an acidic potassium permanganate solution ( $1 \text{ g}\cdot\text{L}^{-1} \text{ KMnO}_4$  (Fluka, ACS reagent) in  $0.5 \text{ M H}_2\text{SO}_4$  (Fluka, ACS reagent)) overnight. The solution was subsequently drained and the cell compartments were rinsed with a dilute piranha solution (1:3 v/v of  $\text{H}_2\text{O}_2$  (Merck, Emprove exp) /  $\text{H}_2\text{SO}_4$ ) to remove residual  $\text{KMnO}_4$  and  $\text{MnOx}$ . Afterwards, the cell compartments were cleaned by repetitive rinsing and boiling with Milli-Q water to remove all inorganic contaminants.

**Preparation of polycrystalline platinum (Pt) disk electrode.** A polycrystalline platinum (Pt) disk electrode in E6/E5 ChangeDisk tips embedded with a PEEK shroud (Pine Research) was used as working electrode. Prior to the electrochemical experiments, the polycrystalline Pt disk electrode was mechanically polished on a microcloth (Buehler) for 2 min with 1, 0.25 and  $0.05 \text{ }\mu\text{m}$  diamond suspension (MetaDi, Buehler), respectively. After mechanical polishing, the obtained working electrode was sonicated in Milli-Q water for 15 min and rinsed with Milli-Q water. The obtained polycrystalline Pt disk electrode was then mounted on the rotating disk electrode (RDE) tip for electrochemical experiments.

**Electrochemical measurements.** All electrochemical experiments were carried out with a BioLogic potentiostat (SP-300) and a modulated speed rotator (Pine Research) in a standard three-electrode electrochemical cell. A Pt wire (0.5 mm diameter, MaTecK, 99.9%) was used as the counter electrode, a leakless Ag/AgCl (EDAQ) was used as the reference electrode. All reported potentials were converted to the reversible hydrogen electrode scale. Prior to each experiment, argon (Linde, 6.0) was purged through the electrolyte for at least 20 min. Next, the polycrystalline Pt disk electrode was electrochemically polished in 0.1 M H<sub>2</sub>SO<sub>4</sub> between 0.06 and 1.65 V vs RHE for 200 cycles at 0.5 V s<sup>-1</sup>. Thereafter, blank cyclic voltammograms were then taken at a scan rate of 50 mV s<sup>-1</sup> in the same potential window to characterize the surface, as shown in Figure C.1. For calculating the current densities for the HER activity, the electrochemical active surface area (ECSA) was determined from the integral of the hydrogen region (0.06 to 0.6 V, 230  $\mu\text{C cm}^{-2}$ ).<sup>32</sup> The obtained working electrode was then used for subsequent hydrogen evolution experiments. The experiment in the absence of metal cations was performed in 1 mM HClO<sub>4</sub> (pH 3). In case of different cation concentration electrolytes, the calculated amounts of salt (LiClO<sub>4</sub> or KClO<sub>4</sub>) were added to the prepared solution of 1 mM HClO<sub>4</sub>. For all hydrogen evolution experiments, the solution resistance was determined by carrying out electrochemical impedance spectroscopy (EIS). The electrode potential was compensated for 100% of ohmic drop for the electrolytes with cation concentration less than 10 mM and 85% of the ohmic drop for all other electrolytes.

**RRDE pH measurements.** A ring-disk electrode (Au ring and Pt disk, E6/E5 ChangeDisk, Pine Research), a Pt wire (0.5 mm diameter, MaTecK, 99.9%) and a Ag/AgCl electrode were used as working electrode, counter electrode and reference electrode respectively. The Au ring and Pt disk electrodes were mechanically polished separately in the same manner as the Pt rotating disk electrode and then assembled. Afterward, the Pt disk was electrochemically polished and characterized in the same manner with Pt rotating disk electrode. In the meantime, the Au ring was prepared according to previous reported work.<sup>31, 33</sup> Specifically, the Au ring was characterized in argon-saturated 0.1 M H<sub>2</sub>SO<sub>4</sub> by cyclic voltammetry at 100 mV s<sup>-1</sup> between 0 to 1.75 V vs RHE. Next, the Pt disk was changed into a Teflon counterpart and the RRDE tip was dipped into a 1 mM 4-nitrothiophenol (4-NTP, Merck, 80%) dissolved

in ethanol (96%, absolute, VWR) solution for 20 min, during which the nitro compound self-assembles as a monolayer on the Au ring. The obtained modified Au ring was then rinsed with ethanol and water respectively, and dried in a N<sub>2</sub> flow. The Pt disk was reassembled carefully and the 4-NTP on the Au ring was further converted to the pH sensing redox couple 4-nitrosothiophenol (4-NSTP)/hydroxylaminothiophenol (4-HATP) via cyclic voltammetry in 0.1 M H<sub>2</sub>SO<sub>4</sub> from 0.68 to 0.11 vs RHE at 100 mV s<sup>-1</sup>. A lower vertex potential of 0.11 V vs RHE was set to maximize the conversion efficiency.

The cyclic voltammograms of the 4-NSTP/4-HATP pH sensing couple were continuously recorded at a scan rate of 200 mV s<sup>-1</sup> while the linear sweep voltammetry was performed on Pt disk. The potential window for cyclic voltammetry on the 4-NSTP/4-HATP pH sensing couple modified Au ring was adjusted positively with the increase of the interfacial pH. Details of the calculations of the interfacial pH are identical as listed in the Electronic Supplementary Material of a previously reported work from our group.<sup>31</sup>

### 4.3 Results and Discussion

#### 4.3.1 Results

First, we examine the cation concentration effect on HER activity on a polycrystalline Pt electrode. Figure 4.1 shows HER current on a Pt polycrystalline electrode at 2400 rpm in pH 3 electrolytes in the presence of 5, 10, 50, 80 and 130 mM LiClO<sub>4</sub> respectively, and the corresponding Tafel slope derived therefrom (see also Figure C.2 in the Supporting Information). Due to the low hydronium ion (H<sub>3</sub>O<sup>+</sup>) concentration in pH 3 electrolytes, the proton donor for HER shifts from hydronium ions (H<sub>3</sub>O<sup>+</sup>) at low overpotentials to water (H<sub>2</sub>O) at high overpotentials, which is reflected in the linear sweep voltammograms in Figure 4.1. As shown in Figures 4.1a, b, the proton reduction current and Tafel slopes of ca. 39 mV/dec are the same in all electrolytes at low overpotentials, which implies the same mechanism and shows that the cation concentration does not affect the proton reduction in kinetically limited regime. At intermediate potentials (~-0.2 - -0.7 V), there is a mass transport limited plateau, which is due to the limited mass transfer of hydronium ions (H<sub>3</sub>O<sup>+</sup>) to the surface of the

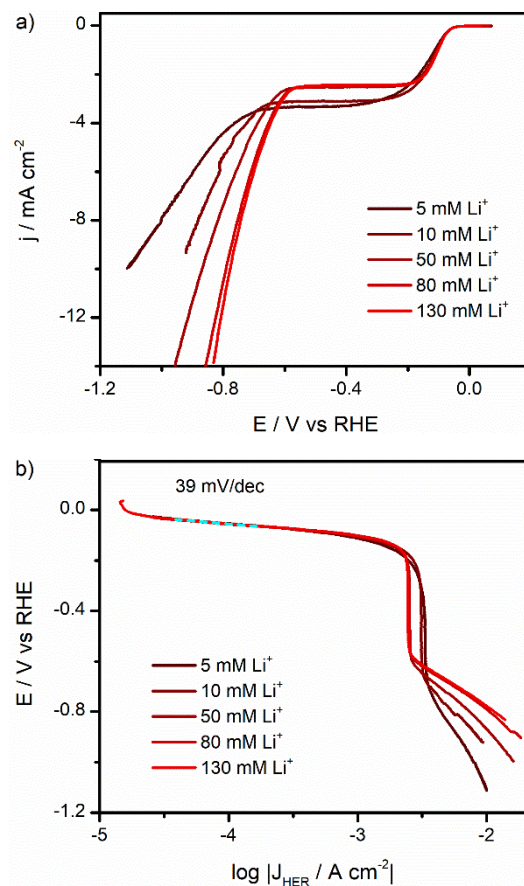


**Figure 4.1** Cation ( $\text{Li}^+$ ) concentration effect on HER. a) Linear sweep voltammograms obtained on a polycrystalline Pt electrode at 2400 rpm in pH 3  $\text{HClO}_4$  electrolyte in the presence of 5, 10, 50, 80 and 130 mM  $\text{LiClO}_4$  respectively. Scan rate:  $10 \text{ mV s}^{-1}$ . b) Tafel slope analysis derived from the linear sweep voltammograms shown in a), the range used for fitting is indicated in all plots with a dotted line in blue. A Tafel slope plot of Figure 4.1a is given in the Supporting Information, Figure C.2.<sup>34</sup>

electrode. At further negative potentials, the water reduction reaction sets in. Notably, with the increase of  $\text{Li}^+$  cation concentration, the water reduction current is enhanced significantly with the increasing  $\text{Li}^+$  cation concentration in these electrolytes. As shown in Figure C.2b, the obtained Tafel slopes for water reduction are high ( $> 120 \text{ mV/dec}$ ), but become lower with increasing concentration of  $\text{Li}^+$  (from ca 800 to ca.300  $\text{mV/dec}$ ), suggesting strong non-potential dependent contributions to the current. On the other hand, the diffusion limited current decreases with increasing  $\text{Li}^+$  cation concentration in the electrolyte. The same trend

has also been observed in pH 3 electrolytes with the presence of 1, 2, 5, 10, 50 and 80 mM  $\text{KClO}_4$ , as shown in Figure C.3. Additionally, no clear diffusion limited plateau was observed in pH 3 electrolytes in the presence of 1 and 2 mM  $\text{KClO}_4$ . This result suggests that the mass transport limited current is strongly distorted in electrolytes with low cation concentrations. Despite the fact that other factors, such as cation hydrolysis and cation-modified diffusion coefficient of protons,<sup>35-36</sup> may contribute to the decreased mass transport limited current, our result suggests the non-negligible  $\text{H}_3\text{O}^+$  migration current in pH 3 electrolytes with a low cation concentration.<sup>37</sup> This migration component adds further complexity in understanding the cation effect on HER in pH 3 electrolytes.

However, the migration current near the electrode can be greatly suppressed by introducing a excess supporting electrolyte.<sup>38</sup> Figure 4.1 shows a (relatively) stable mass transport limited current in the presence of at least 50 mM  $\text{LiClO}_4$ . Therefore, to minimize the migration current, we select 80 mM perchlorate as the supporting electrolyte, in which the diffusion limited current is identical to that calculated by the Levich equation ( $2.59 \text{ mA cm}^{-2}$  under our working conditions).

Figure 4.2 shows the HER activity on a polycrystalline Pt electrode in pH 3 electrolytes with 80 mM  $\text{KClO}_4$  or  $\text{LiClO}_4$  as the supporting electrolyte. While the proton reduction current remains constant at low overpotentials in all electrolytes, the water reduction is notably influenced by the cations present in the electrolytes. Specifically, an onset potential of ca. -0.70 V vs RHE for water reduction is observed in pH 3 electrolyte in the presence of 80 mM  $\text{K}^+$ . Under the same conditions, the onset potential for water reduction in pH 3 electrolyte with 80 mM  $\text{Li}^+$  is approximately -0.57 V vs RHE. Moreover, the onset potential of water reduction shifts positively with increasing  $\text{Li}^+$  concentration in pH 3 electrolyte with 80 mM  $\text{K}^+$  as the supporting electrolyte. On the other hand, the water reduction current (both onset potential and activity) remains constant despite the increased  $\text{K}^+$  concentrations in pH 3 electrolyte with 80 mM  $\text{Li}^+$  as the supporting electrolyte (Figure 4.2b).



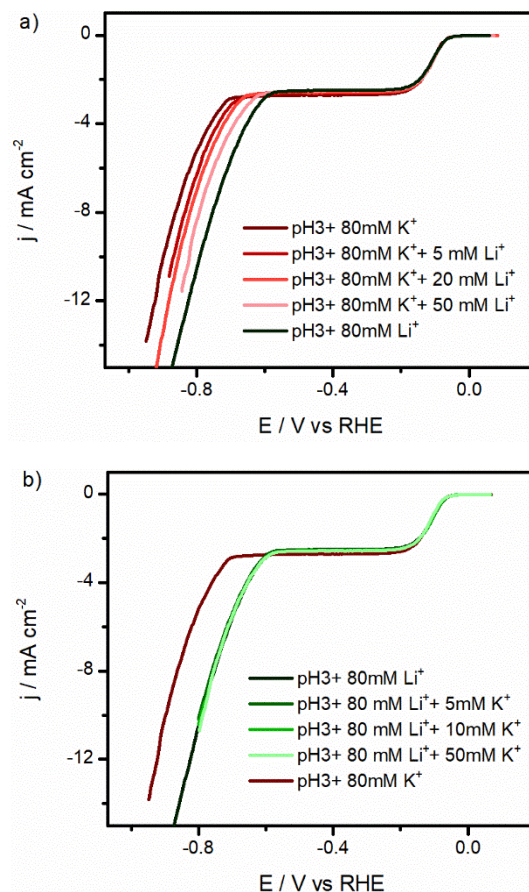


**Figure 4.2** Linear sweep voltammograms obtained for the HER on a polycrystalline Pt electrode at 2400 rpm in pH 3 electrolytes. a) In the presence of 80 mM  $\text{KClO}_4$  + x mM  $\text{LiClO}_4$  and 80 mM  $\text{LiClO}_4$ . b) In the presence of 80 mM  $\text{LiClO}_4$  + x mM  $\text{KClO}_4$  and 80 mM  $\text{KClO}_4$ , where x represents 0, 5, 10, 20 or 50 respectively. Scan rate:  $10 \text{ mV s}^{-1}$ . A cation concentration reaction order plot for the HER current in Fig.4.2a is shown in Figure C.4 in the Supporting Information.

Tafel slopes for water reduction derived from linear sweep voltammograms in Figure 4.2 are given in Figure C.5. The obtained Tafel slopes for water reduction remains constant in all electrolytes, which suggest the same (or similar) kinetics of water reduction in all electrolytes. Simultaneously, the obtained cation concentration reaction order plot shown in Figure C.4 indicates the promoting effect of  $\text{Li}^+$  in water reduction. This promotional effect of strongly hydrated cations ( $\text{Li}^+$ ) on the activity of water reduction on polycrystalline Pt has been observed previously; we note the inhibition effect of  $\text{K}^+$  on water reduction reported in that work was observed under strongly (bulk) alkaline conditions.<sup>10, 12, 19</sup>

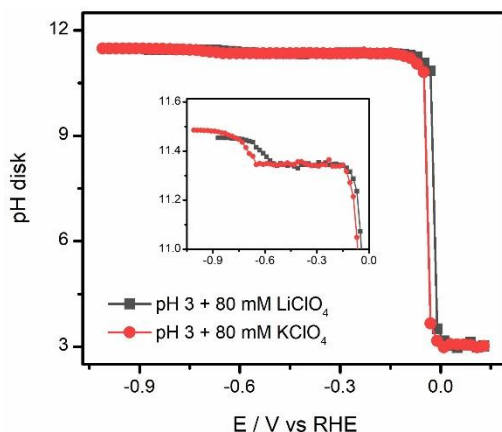


**Figure 4.3** The interfacial pH at the Pt disk electrode as a function of potential during linear sweep voltammetry at 2400 rpm and  $10 \text{ mV s}^{-1}$  in pH 3 electrolytes in the presence of 80 mM  $\text{LiClO}_4$  and  $\text{KClO}_4$  respectively, as measured using RRDE voltammetry.

To gain additional insights into the mechanism underlying the observed cation effect, the interfacial pH of the Pt disk electrode during LSV is measured with RRDE using a voltammetric pH sensor on the ring.<sup>31, 33</sup> Figure 4.3 shows the measured interfacial pH at the Pt disk electrode during linear sweep voltammetry in pH 3 electrolytes in the presence of 80 mM  $\text{LiClO}_4$  and  $\text{KClO}_4$  respectively. The increase in current density during the negative going sweep leads to a continuous consumption of  $\text{H}_3\text{O}^+$  or an increasing generation of  $\text{OH}^-$  near the surface of the Pt disk electrode. As a result, the interfacial pH rises simultaneously with the current density. As shown in Figure 4.3, the interfacial pH increases at the potential where proton reduction and water reduction occur. However, the same interfacial pH is observed at the mass transport limited plateau irrespective of the cations present in the electrolytes.

#### 4.3.2 Discussion

In the present work, we show a decreased diffusion limited current with increasing cation concentration in the electrolyte at pH 3. We assume the decreased diffusion limited current was due to the non-negligible migration current in electrolytes with low cation concentrations, given that the diffusion limited current is relatively stable and nearly the value as defined in the Levich equation in the presence of at least 50 mM perchlorate in the electrolyte. Although

previous work suggests a suppressed proton diffusion kinetics in presence of a high concentration of cations,<sup>36</sup> we believe that the decreased diffusion limited current observed here is mainly from the suppressed migration current under our working conditions, namely in electrolytes with cation concentration of ca. 100 mM.<sup>37</sup>

In the presence of 80 mM KClO<sub>4</sub> or LiClO<sub>4</sub> as the supporting electrolyte, the improved onset potential for water reduction with increasing Li<sup>+</sup> concentration indicates the essential role of cations for water reduction at pH 3 and the superior effect of Li<sup>+</sup> cation in promoting water reduction on Pt electrode. Although previous work suggests an inhibition of HER by weakly hydrated cations on Pt, the unchanged water reduction current with increasing K<sup>+</sup> concentration in pH 3 with 80 mM LiClO<sub>4</sub> as the supporting electrolyte indicates the inability of K<sup>+</sup> in promoting water reduction at -0.57 V vs RHE. Further, interfacial pH measurements show a similar interfacial pH at Pt surface under diffusion limited conditions, which excludes the role of interfacial pH effect caused by cation hydrolysis near the electrode.<sup>35, 39</sup> Consequently, neither a migration effect nor the local pH effect could explain the difference of 0.13 V in the onset of water reduction between Li<sup>+</sup> and K<sup>+</sup> containing electrolyte. Instead, our result suggests strongly hydrated cations (Li<sup>+</sup>) promote water dissociation more favorably compared to weakly hydrated cations (K<sup>+</sup>), under the conditions of the experiment.

The activity for CO<sub>2</sub>RR products has been reported to increase in the order Cs<sup>+</sup> > K<sup>+</sup> > Na<sup>+</sup> > Li<sup>+</sup> on various electrodes in mild acidic media.<sup>40-41</sup> Although a different pathway has been reported for formic acid production, it has been proposed that weakly hydrated cations stabilize CO<sub>2</sub>RR intermediates through local electrostatic interactions within the electrical double layer better than strongly hydrated cations.<sup>40-41</sup> Our results provide new insights into the competition between HER and CO<sub>2</sub>RR on Pt based catalysts, a slower water reduction currents are expected with a weakly hydrated cation present in neutral or alkaline electrolyte. This could also add additional insights into the Faraday efficiency (FE) of 99% for HCOOH production at -0.1 V vs RHE on Pd catalysts in 2.8 M KHCO<sub>3</sub>,<sup>42</sup> where low HER activity are expected. Although further experiments are needed to prove this assumption, our results at least suggest that it is beneficial to employ weakly hydrated cations in mild acidic electrolyte

when the goal is to suppress HER on Pt-based catalysts.

#### 4.4 Conclusions

We have investigated the cation concentration and identity effect in tuning the activity of HER on Pt electrode in mildly acidic electrolyte across a wide potential range. Our findings indicate that cations exhibit no discernible effect on proton reduction at low overpotentials. However, we identify a non-negligible migration current during proton reduction in electrolytes with low cation concentration, a current component which can be effectively suppressed by introducing adequate supporting electrolyte. Furthermore, our study delves into the essential role of cations, particularly  $\text{Li}^+$ , in promoting water reduction on Pt electrodes. The promoting role of  $\text{Li}^+$  is not related to migration effects or local pH effects, as  $\text{K}^+$  does not promote water reduction, but still generates the same local pH. Our work hints at the potential benefits of utilizing weakly hydrated cations on Pt based catalysts if the goal is to suppress HER.

## References

1. Sheng, W.; Gasteiger, H. A.; Shao-Horn, Y., Hydrogen Oxidation and Evolution Reaction Kinetics on Platinum: Acid vs Alkaline Electrolytes. *J. Electrochem. Soc.* **2010**, *157* (11), B1529.
2. Subbaraman, R.; Tripkovic, D.; Strmcnik, D.; Chang, K. C.; Uchimura, M.; Paulikas, A. P.; Stamenkovic, V.; Markovic, N. M., Enhancing hydrogen evolution activity in water splitting by tailoring Li(+)-Ni(OH)(2)-Pt interfaces. *Science* **2011**, *334* (6060), 1256-60.
3. Stamenkovic, V. R.; Strmcnik, D.; Lopes, P. P.; Markovic, N. M., Energy and fuels from electrochemical interfaces. *Nat Mater* **2016**, *16* (1), 57-69.
4. Strmcnik, D.; Lopes, P. P.; Genorio, B.; Stamenkovic, V. R.; Markovic, N. M., Design principles for hydrogen evolution reaction catalyst materials. *Nano Energy* **2016**, *29*, 29-36.
5. Ledezma-Yanez, I.; Wallace, W. D. Z.; Sebastián-Pascual, P.; Climent, V.; Feliu, J. M.; Koper, M. T. M., Interfacial water reorganization as a pH-dependent descriptor of the hydrogen evolution rate on platinum electrodes. *Nature Energy* **2017**, *2* (4).
6. Lamoureux, P. S.; Singh, A. R.; Chan, K., pH Effects on Hydrogen Evolution and Oxidation over Pt(111): Insights from First-Principles. *ACS Catal.* **2019**, *9* (7), 6194-6201.
7. Waagele, M. M.; Gunathunge, C. M.; Li, J.; Li, X., How cations affect the electric double layer and the rates and selectivity of electrocatalytic processes. *J. Chem. Phys.* **2019**, *151* (16), 160902.
8. McCrum, I. T.; Koper, M. T. M., The role of adsorbed hydroxide in hydrogen evolution reaction kinetics on modified platinum. *Nature Energy* **2020**, *5* (11), 891-899.
9. Goyal, A.; Koper, M. T. M., The Interrelated Effect of Cations and Electrolyte pH on the Hydrogen Evolution Reaction on Gold Electrodes in Alkaline Media. *Angew. Chem. Int. Ed. Engl.* **2021**, *60* (24), 13452-13462.
10. Goyal, A.; Koper, M. T. M., Understanding the role of mass transport in tuning the hydrogen evolution kinetics on gold in alkaline media. *J. Chem. Phys.* **2021**, *155* (13), 134705.
11. Huang, B.; Rao, R. R.; You, S.; Hpone Myint, K.; Song, Y.; Wang, Y.; Ding, W.; Giordano, L.; Zhang, Y.; Wang, T.; Muy, S.; Katayama, Y.; Grossman, J. C.; Willard, A. P.; Xu, K.; Jiang, Y.; Shao-Horn, Y., Cation- and pH-Dependent Hydrogen Evolution and Oxidation Reaction Kinetics. *JACS Au* **2021**, *1* (10), 1674-1687.
12. Monteiro, M. C. O.; Goyal, A.; Moerland, P.; Koper, M. T. M., Understanding Cation Trends for Hydrogen Evolution on Platinum and Gold Electrodes in Alkaline Media. *ACS Catal.* **2021**, *11* (23), 14328-14335.
13. Monteiro, M. C. O.; Dattila, F.; Lopez, N.; Koper, M. T. M., The Role of Cation Acidity on the Competition between Hydrogen Evolution and CO<sub>2</sub> Reduction on Gold Electrodes. *J. Am. Chem. Soc.* **2022**, *144* (4), 1589-1602.
14. Pentland, N.; Bockris, J. O. M.; Sheldon, E., Hydrogen Evolution Reaction on Copper, Gold, Molybdenum, Palladium, Rhodium, and Iron: Mechanism and Measurement Technique under High Purity Conditions. *J. Electrochem. Soc.* **1957**, *104* (3), 182.
15. Nørskov, J. K.; Bligaard, T.; Logadottir, A.; Kitchin, J. R.; Chen, J. G.; Pandelov, S.; Stimming, U., Trends in the Exchange Current for Hydrogen Evolution. *J. Electrochem. Soc.* **2005**, *152* (3), J23.
16. Rebollar, L.; Intikhab, S.; Oliveira, N. J.; Yan, Y.; Xu, B.; McCrum, I. T.; Snyder, J. D.; Tang, M. H., "Beyond Adsorption" Descriptors in Hydrogen Electrocatalysis. *ACS Catal.* **2020**, *10* (24), 14747-14762.

17. Rebollar, L.; Intikhab, S.; Snyder, J. D.; Tang, M. H., Kinetic Isotope Effects Quantify pH-Sensitive Water Dynamics at the Pt Electrode Interface. *J. Phys. Chem. Lett.* **2020**, *11* (6), 2308-2313.
18. Subbaraman, R.; Tripkovic, D.; Chang, K. C.; Strmcnik, D.; Paulikas, A. P.; Hirunsit, P.; Chan, M.; Greeley, J.; Stamenkovic, V.; Markovic, N. M., Trends in activity for the water electrolyser reactions on 3d M(Ni,Co,Fe,Mn) hydr(oxy)oxide catalysts. *Nat Mater* **2012**, *11* (6), 550-7.
19. Strmcnik, D.; Kodama, K.; van der Vliet, D.; Greeley, J.; Stamenkovic, V. R.; Markovic, N. M., The role of non-covalent interactions in electrocatalytic fuel-cell reactions on platinum. *Nat Chem* **2009**, *1* (6), 466-72.
20. Strmcnik, D.; Uchimura, M.; Wang, C.; Subbaraman, R.; Danilovic, N.; van der Vliet, D.; Paulikas, A. P.; Stamenkovic, V. R.; Markovic, N. M., Improving the hydrogen oxidation reaction rate by promotion of hydroxyl adsorption. *Nat Chem* **2013**, *5* (4), 300-6.
21. Liu, E.; Li, J.; Jiao, L.; Doan, H. T. T.; Liu, Z.; Zhao, Z.; Huang, Y.; Abraham, K. M.; Mukerjee, S.; Jia, Q., Unifying the Hydrogen Evolution and Oxidation Reactions Kinetics in Base by Identifying the Catalytic Roles of Hydroxyl-Water-Cation Adducts. *J. Am. Chem. Soc.* **2019**, *141* (7), 3232-3239.
22. Xue, S.; Garlyyev, B.; Watzele, S.; Liang, Y.; Fichtner, J.; Pohl, M. D.; Bandarenka, A. S., Influence of Alkali Metal Cations on the Hydrogen Evolution Reaction Activity of Pt, Ir, Au, and Ag Electrodes in Alkaline Electrolytes. *ChemElectroChem* **2018**, *5* (17), 2326-2329.
23. Kuhl, K. P.; Cave, E. R.; Abram, D. N.; Jaramillo, T. F., New insights into the electrochemical reduction of carbon dioxide on metallic copper surfaces. *Energy Environ. Sci.* **2012**, *5* (5), 7050-7059.
24. Cave, E. R.; Montoya, J. H.; Kuhl, K. P.; Abram, D. N.; Hatsukade, T.; Shi, C.; Hahn, C.; Nørskov, J. K.; Jaramillo, T. F., Electrochemical CO<sub>2</sub> reduction on Au surfaces: mechanistic aspects regarding the formation of major and minor products. *Phys. Chem. Chem. Phys.* **2017**, *19* (24), 15856-15863.
25. Gao, D.; Zhou, H.; Wang, J.; Miao, S.; Yang, F.; Wang, G.; Wang, J.; Bao, X., Size-dependent electrocatalytic reduction of CO<sub>2</sub> over Pd nanoparticles. *J. Am. Chem. Soc.* **2015**, *137* (13), 4288-91.
26. Ooka, H.; Figueiredo, M. C.; Koper, M. T. M., Competition between Hydrogen Evolution and Carbon Dioxide Reduction on Copper Electrodes in Mildly Acidic Media. *Langmuir* **2017**, *33* (37), 9307-9313.
27. Bondue, C. J.; Graf, M.; Goyal, A.; Koper, M. T. M., Suppression of Hydrogen Evolution in Acidic Electrolytes by Electrochemical CO<sub>2</sub> Reduction. *J. Am. Chem. Soc.* **2021**, *143* (1), 279-285.
28. Huang, J. E.; Li, F.; Ozden, A.; Sedighian Rasouli, A.; Garcia de Arquer, F. P.; Liu, S.; Zhang, S.; Luo, M.; Wang, X.; Lum, Y.; Xu, Y.; Bertens, K.; Miao, R. K.; Dinh, C. T.; Sinton, D.; Sargent, E. H., CO<sub>2</sub> electrolysis to multicarbon products in strong acid. *Science* **2021**, *372* (6546), 1074-1078.
29. Gu, J.; Liu, S.; Ni, W.; Ren, W.; Haussener, S.; Hu, X., Modulating electric field distribution by alkali cations for CO<sub>2</sub> electroreduction in strongly acidic medium. *Nat. Catal.* **2022**, *5* (4), 268-276.
30. Ma, Z.; Yang, Z.; Lai, W.; Wang, Q.; Qiao, Y.; Tao, H.; Lian, C.; Liu, M.; Ma, C.; Pan, A.; Huang, H., CO<sub>2</sub> electroreduction to multicarbon products in strongly acidic electrolyte via synergistically modulating the local microenvironment. *Nat. Commun.* **2022**, *13* (1), 7596.
31. Liu, X.; Monteiro, M. C. O.; Koper, M. T. M., Interfacial pH measurements during CO<sub>2</sub> reduction on gold using a rotating ring-disk electrode. *Phys. Chem. Chem. Phys.* **2023**, *25* (4), 2897-2906.
32. Chen, Q.-S.; Solla-Gullón, J.; Sun, S.-G.; Feliu, J. M., The potential of zero total charge of Pt nanoparticles and polycrystalline electrodes with different surface structure: The role of anion adsorption in fundamental electrocatalysis. *Electrochim. Acta* **2010**, *55* (27), 7982-7994.

33. Monteiro, M. C. O.; Liu, X.; Hagedoorn, B. J. L.; Snabilić, D. D.; Koper, M. T. M., Interfacial pH Measurements Using a Rotating Ring-Disc Electrode with a Voltammetric pH Sensor. *ChemElectroChem* **2021**, 9 (1).
34. van der Heijden, O.; Park, S.; Vos, R. E.; Eggebeen, J. J. J.; Koper, M. T. M., Tafel Slope Plot as a Tool to Analyze Electrocatalytic Reactions. *ACS Energy Lett.* **2024**, 9 (4), 1871-1879.
35. Singh, M. R.; Kwon, Y.; Lum, Y.; Ager, J. W., 3rd; Bell, A. T., Hydrolysis of Electrolyte Cations Enhances the Electrochemical Reduction of CO<sub>2</sub> over Ag and Cu. *J. Am. Chem. Soc.* **2016**, 138 (39), 13006-13012.
36. Li, X. Y.; Wang, T.; Cai, Y. C.; Meng, Z. D.; Nan, J. W.; Ye, J. Y.; Yi, J.; Zhan, D. P.; Tian, N.; Zhou, Z. Y.; Sun, S. G., Mechanism of Cations Suppressing Proton Diffusion Kinetics for Electrocatalysis. *Angew. Chem. Int. Ed. Engl.* **2023**, 62 (14), e202218669.
37. Amatore, C.; Fosset, B.; Bartelt, J.; Deakin, M. R.; Wightman, R. M., Electrochemical kinetics at microelectrodes: Part V. Migrational effects on steady or quasi-steady-state voltammograms. *J. Electroanal. Chem. Interfacial Electrochem.* **1988**, 256 (2), 255-268.
38. Bard, A. J.; Faulkner, L. R., *Electrochemical Methods: Fundamentals and Applications*. 2nd ed.; John Wiley & Sons 2001.
39. Ayemoba, O.; Cuesta, A., Spectroscopic Evidence of Size-Dependent Buffering of Interfacial pH by Cation Hydrolysis during CO<sub>2</sub> Electroreduction. *ACS Appl. Mater. Interfaces* **2017**, 9 (33), 27377-27382.
40. Monteiro, M. C.; Dattila, F.; Hagedoorn, B.; García-Muelas, R.; López, N.; Koper, M., Absence of CO<sub>2</sub> electroreduction on copper, gold and silver electrodes without metal cations in solution. *Nat. Catal.* **2021**, 4 (8), 654-662.
41. Ye, C.; Dattila, F.; Chen, X.; Lopez, N.; Koper, M. T. M., Influence of Cations on HCOOH and CO Formation during CO<sub>2</sub> Reduction on a Pd(ML)Pt(111) Electrode. *J. Am. Chem. Soc.* **2023**, 145 (36), 19601-19610.
42. Min, X.; Kanan, M. W., Pd-catalyzed electrohydrogenation of carbon dioxide to formate: high mass activity at low overpotential and identification of the deactivation pathway. *J. Am. Chem. Soc.* **2015**, 137 (14), 4701-8.

## **Chapter 5**

### **Electrolyte Effect on the Electrochemical CO<sub>2</sub> Reduction on Copper Gas Diffusion Electrodes**



**Abstract:** The electrochemical reduction of CO<sub>2</sub> (CO<sub>2</sub>RR) to multicarbon products at high current density over long electrolysis times remains an important challenge for implementation of this technology. In addition to neutral and alkaline media, recent works has shown that CO<sub>2</sub>RR to multicarbon products can also be achieved in highly acidic media (pH < 1). In this work, we investigate the influence of bulk electrolyte pH on CO<sub>2</sub>RR product distribution by studying the CO<sub>2</sub>RR product distribution on a copper gas diffusion electrode (Cu GDE) in a traditional bicarbonate electrolyte and a mildly acidic electrolyte in the presence of the same concentration of cations as in the bicarbonate electrolyte. We show that different CO<sub>2</sub>RR product distributions were only observed at low total applied current densities. Our results indicate that the selectivity of CO<sub>2</sub>RR on the copper GDE is independent of bulk pH and anions of the electrolyte at high total applied current densities. SEM images, along with EDX elemental mapping, indicate a less stable catalyst layer of the Cu GDE, resulting in electrode degradation over long electrolysis in acidic media compared to that in the bicarbonate electrolyte. Our work thereby confirms the importance of local environment on CO<sub>2</sub>RR and offers a more comprehensive understanding of CO<sub>2</sub>RR on Cu GDE in acidic media.

## 5.1 Introduction

The electrochemical carbon dioxide reduction reaction (CO<sub>2</sub>RR) has gained substantial interest in the last few decades for the sustainable production of chemicals and fuels by utilizing an abundant carbon feedstock and renewable electricity. The CO<sub>2</sub>RR can generate various products in aqueous media, including formic acid (HCOOH), carbon monoxide (CO), hydrocarbons, and alcohols, depending on the catalyst and the microenvironment.<sup>1-4</sup> Copper-based catalysts are the only catalysts which produce significant amounts of high-value multicarbon products such as ethylene and ethanol during CO<sub>2</sub>RR.<sup>5</sup> Despite extensive effort of the scientific community, reducing CO<sub>2</sub> toward multicarbon products with high activity and selectivity at low overpotentials remains challenging, which hinders the further industrial application of CO<sub>2</sub>RR.<sup>6</sup>

In recent years, flow cells and gas diffusion electrodes (GDEs) have been employed to CO<sub>2</sub>RR electrolyzers. The porous structure of the GDE allows continuous CO<sub>2</sub> supply to the catalyst-electrolyte interface and therefore greatly improves local CO<sub>2</sub> concentration near the electrode during CO<sub>2</sub>RR, enabling high current densities even at ambient conditions.<sup>6-11</sup>

In addition to the cell and GDE design, the nature of the catalysts as well as the electrolyte composition have been shown to play important roles in the CO<sub>2</sub>RR. Highly alkaline potassium hydroxide electrolyte was found to improve the rate of C-C bond formation and facilitate production of C<sub>2</sub>H<sub>4</sub>.<sup>12</sup> However, rapid electrode degradation was observed in highly alkaline electrolyte,<sup>9, 13</sup> with one of the degradation mechanisms being KHCO<sub>3</sub> precipitation resulting from the reaction between CO<sub>2</sub> and KOH.<sup>13-15</sup> Other than the carbonate precipitation, such a reaction also leads to substantial CO<sub>2</sub> loss in the alkaline electrolyte and therefore greatly limits the carbon efficiency of the system.<sup>7, 9-11</sup>

To overcome these shortcomings, recently acidic electrolytes have been employed in CO<sub>2</sub>RR electrolyzers using flow cells and GDEs.<sup>7, 9-11</sup> Previous work has shown a CO faradaic efficiency of 80-90% on a gold GDE in pH 3 and 4 sulfate electrolyte.<sup>7</sup> In addition to a mildly acid electrolyte, strong acidic electrolyte (pH around 1) was employed with a Cu GDE

in flow cells.<sup>10-11, 16</sup> Although less CO<sub>2</sub> loss is expected in acidic electrolyte, different product distributions have been observed on Cu GDE.<sup>10-11, 16</sup> For example, FE of about 40% for hydrogen (H<sub>2</sub>) and a total C<sub>2+</sub> FE of 40% were observed on a Cu GDE modified with a cation-augmenting layer,<sup>10</sup> CO and HCOOH were observed on Cu/C as main products at low overpotentials and FE with about 50% for H<sub>2</sub> at high overpotentials,<sup>11</sup> while a total FE of 83.7% for C<sub>2+</sub> products was observed on electrochemically reduced porous Cu nanosheets.<sup>16</sup> The observed different product distribution may result from various aspects, for example, gas electrode preparation method, electrode composition, CO<sub>2</sub> flow rate or cell configuration. Therefore, it is difficult to assign the stable electrolysis demonstrated in these works to the acidic electrolytes. To elucidate this, more systematic work is needed to exclude factors other than the pH of the electrolyte.

In this work, we investigate the influence of electrolytes with different bulk pH on both the CO<sub>2</sub>RR product distribution and long-term electrode durability. We show the different product distributions at low total applied current densities, i.e. H<sub>2</sub> and HCOOH as main products in a CO<sub>2</sub> saturated 0.5 M KHCO<sub>3</sub> electrolyte and HCOOH and CO as main products in a CO<sub>2</sub> saturated pH 3 electrolyte with a presence of 0.25 M K<sub>2</sub>SO<sub>4</sub> at the total applied current densities of 10 and 50 mA cm<sup>-2</sup>, and similar product distributions at high current densities. In addition, we observed continuous decay after 5 hours electrolysis in both electrolytes. SEM images and EDX elemental mapping of Cu GDEs after long term electrolysis suggests that, in addition to the carbonate precipitation and Fe poisoning, the unstable catalyst layer in acidic media contributes to the electrode degradation during long term electrolysis.

## 5.2 Experimental Section

**Materials and chemicals.** KHCO<sub>3</sub> (99.5%), K<sub>2</sub>SO<sub>4</sub>(>99%) and H<sub>2</sub>SO<sub>4</sub> (95% in water) were purchased from Acros Organics. Cu nanoparticles (25 nm), Nafion (5 wt % in lower aliphatic alcohols and water) and Chelex were purchased from Sigma-Aldrich. Milli-Q water (resistivity >18.2 MΩ·cm, TOC < 5 ppb) was used for all experiments in this work.

**GDE preparation.** The gas diffusion layer (GDL) was prepared using a previously reported method.<sup>7</sup> The catalyst ink was prepared by suspending Cu nanoparticles in isopropanol and adding 380  $\mu\text{L}$  of Nafion solution (final 15 wt % of the catalysts). The mixture was then sonicated for 0.5 h to obtain a well dispersed suspension. Finally, the suspension was under continuous stirring to keep the suspension well dispersed. In the meantime, the suspension was airbrushed on a 17  $\text{cm}^2$  GDL. The final GDE was obtained after air drying. A catalyst loading of 1  $\text{mg}/\text{cm}^2$  was calculated from the weight difference before and after airbrushing.

**Electrode characterization.** Scanning electron microscopy (SEM) was performed on an Apreo SEM equipped with an energy-dispersive X-ray (EDX) analyzer to characterize the GDEs. SEM images were obtained with an acceleration voltage of 10 kV and an electron beam current of 0.8 nA. EDX (Instruments X-MaxN 150 Silicon Drift detector) was used for elemental analysis. The quantification was performed in automatic mode, without providing external standards. The data is displayed in atomic percentage for easier visualization.

**Flow cell electrolysis.** The bulk electrolysis experiments were carried out with a commercial two-compartment flow cell with 10  $\text{cm}^2$  GDE (ElectroCell, Micro Flow Cell). A reinforced Nafion membrane N234 was used to separate the anode and the cathode. 0.5M  $\text{H}_2\text{SO}_4$  solution was used as anolyte and a dimensionally stable anode (DSA®, ElectroCell) was used as anode for all measurements. pH of the electrolyte was adjusted with  $\text{H}_2\text{SO}_4$  and a pH meter when necessary. The catholyte was  $\text{CO}_2$  saturated 0.5M  $\text{KHCO}_3$  or pH 3 0.25M  $\text{K}_2\text{SO}_4$  electrolyte. The electrolytes were circulated in the compartments at a flow rate of 30  $\text{mL}/\text{min}$  with a peristaltic pump,  $\text{CO}_2$  was fed through the GDE in the cathodic compartment at a flow rate of 30  $\text{mL}/\text{min}$ . Before each experiment,  $\text{CO}_2$  was purged through electrolyte for 1 h to obtain a stable electrolyte prior to each  $\text{CO}_2\text{RR}$  experiment. The cell was controlled by an Autolab PGSTAT100N potentiostat and each current density was applied for an hour. The gas product analysis was performed with a gas chromatograph (Varian 4900 micro GC) equipped with four modules:  $\text{CO}_x$  module, MS5 (mol. sieve) module, PPQ (poraplotQ) module and 52C WAX module. Gaseous samples were taken from gas outlet every 3 minutes. The current efficiencies shown throughout this work represent the average values obtained at 36, 48 and

60 mins during 1 h of electrolysis, with the corresponding standard deviation. Liquid products were analyzed with High Performance Liquid Chromatograph (HPLC) with an Aminex HPX-87H (BioRad) and a RID detector (Shimadzu). For stability performance, a total applied current density of  $200 \text{ mA cm}^{-2}$  was applied to the cell, with only gas products analyzed as an indicator of  $\text{CO}_2\text{RR}$  performance.

## 5.3 Results and Discussion

### 5.3.1 Results

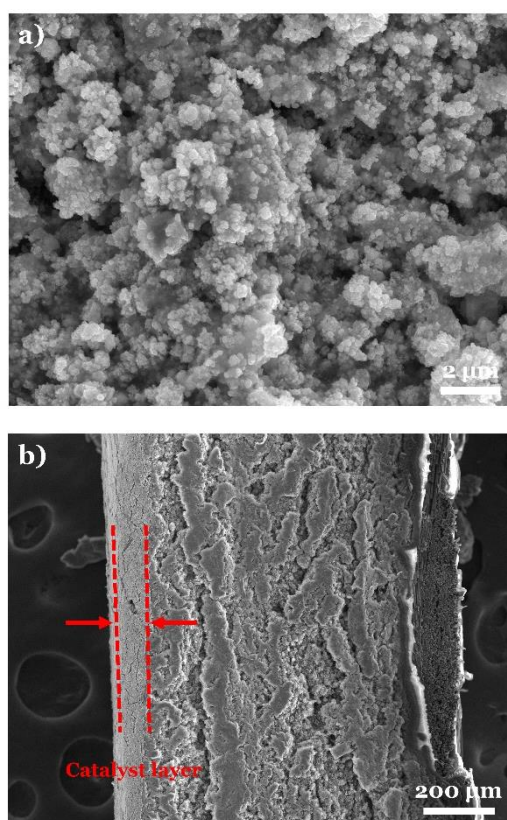


**Figure 5.1** SEM images of a) the surface catalyst and b) cross section of the Cu GDE before  $\text{CO}_2\text{RR}$  experiments.

Scanning electron microscopy was used to characterize the morphology of the Cu GDEs. Figures 5.1a and 1b show SEM images of the surface catalyst and a cross section of the Cu GDEs, respectively, prior to  $\text{CO}_2\text{RR}$  experiments. The Cu nanocatalysts are well dispersed on the surface of the GDE with a layer thickness of about  $100 \text{ μm}$  (the thickness of the catalyst

layer was confirmed with elemental analysis).

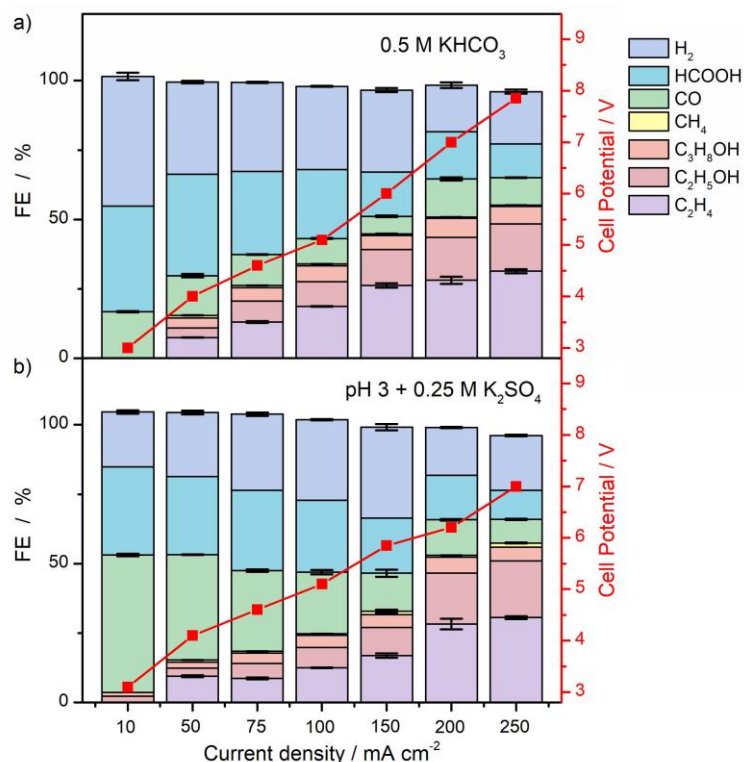


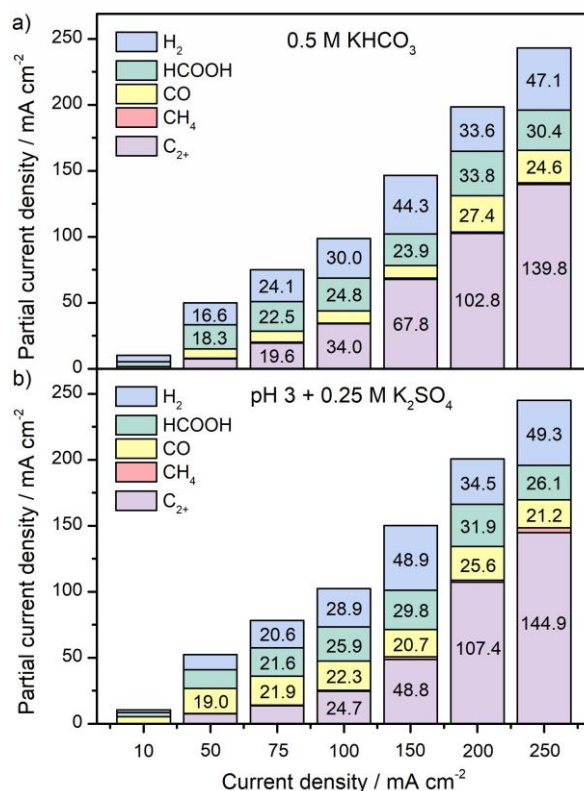
**Figure 5.2** Effect of bulk pH on CO<sub>2</sub>RR performance. FEs of H<sub>2</sub>, HCOOH, CO, CH<sub>4</sub>, C<sub>3</sub>H<sub>8</sub>OH, C<sub>2</sub>H<sub>5</sub>OH and C<sub>2</sub>H<sub>4</sub> (left axis) as well as cell potential (right axis) as a function of total applied current density on Cu GDE in CO<sub>2</sub> saturated a) 0.5M KHCO<sub>3</sub> (pH 7.2) and b) pH 3 electrolyte with the presence of 0.25 M K<sub>2</sub>SO<sub>4</sub> (pH 3.0).

To study the effect of bulk pH on CO<sub>2</sub>RR, experiments were carried out in 0.5M KHCO<sub>3</sub> (bulk pH of 7.2 before electrolysis) and CO<sub>2</sub> saturated 0.25M K<sub>2</sub>SO<sub>4</sub> (adjusted with H<sub>2</sub>SO<sub>4</sub> to a bulk pH of 3 before electrolysis), respectively, where the cation concentrations were deliberately kept the same to exclude a bulk cation concentration effect on CO<sub>2</sub>RR. Figure 5.2 shows the Faradaic efficiencies (FEs) for CO<sub>2</sub>RR products as well as the cell potential in the two electrolytes as a function of total applied current density. As shown in Figure 5.2a, in 0.5M KHCO<sub>3</sub>, H<sub>2</sub> and HCOOH are major products obtained during CO<sub>2</sub>RR at low total applied current densities. Specifically, at 10 mA cm<sup>-2</sup>, the FEs of H<sub>2</sub>, HCOOH and CO are 46.6%, 38.1%, and 16.7% respectively. With increasing total applied current density, the FEs of H<sub>2</sub> and HCOOH decrease, while the total FE of CO and its further reduced products

increase. At the highest total applied current density of  $250 \text{ mA cm}^{-2}$ , the FEs of  $\text{H}_2$  and  $\text{HCOOH}$  have reduced to 18.9% and 12.2% respectively, while the FEs of  $\text{CO}$ ,  $\text{C}_2\text{H}_4$ ,  $\text{C}_2\text{H}_5\text{OH}$  and  $\text{C}_3\text{H}_8\text{OH}$  are 9.9%, 31.4%, 17.3% and 6.3% respectively. These results agree well with previously reported findings for Cu nanoparticle-based GDEs in bicarbonate electrolyte.<sup>17</sup>

Figure 5.2b shows the  $\text{CO}_2\text{RR}$  performance in the pH 3 sulfate electrolyte. At low total applied current densities (below  $100 \text{ mA cm}^{-2}$ ), the primary products are  $\text{HCOOH}$  and  $\text{CO}$ . FEs of  $\text{H}_2$ ,  $\text{HCOOH}$  and  $\text{CO}$  are 19.7%, 31.7%, and 49.6% respectively at  $10 \text{ mA cm}^{-2}$ . These results suggest that  $\text{H}_2$  formation is inhibited at low total applied current densities under these working conditions. This might be explained with the model recently proposed by Bondue et. al.<sup>18</sup> According to their model,  $\text{OH}^-$  generated from  $\text{CO}_2\text{RR}$  could neutralize protons diffusing from bulk electrolyte to the catalyst surface to generate  $\text{H}_2\text{O}$  in pH 3 electrolyte and thereby inhibits  $\text{H}_2$  formation during  $\text{CO}_2\text{RR}$ .<sup>18</sup> This is in contrast with the  $\text{H}_2$  production observed in 0.5M  $\text{KHCO}_3$  at low current densities, where  $\text{HCO}_3^-$  acts as proton donor and is readily reduced to produce  $\text{H}_2$ . Additionally, minor amounts of  $\text{C}_2\text{H}_5\text{OH}$  and  $\text{C}_3\text{H}_8\text{OH}$  are detected in the pH 3 electrolyte already at  $10 \text{ mA cm}^{-2}$ . With increasing total applied current density, the product distribution in the pH 3 electrolyte becomes similar to the one in 0.5 M  $\text{KHCO}_3$ , especially at 200 and  $250 \text{ mA cm}^{-2}$ . These results suggest that the selectivity of  $\text{CO}_2\text{RR}$  on the Cu GDE remains consistent regardless of variations in pH or the composition of the bulk electrolyte at high total applied current densities.

The right axis of Figure 5.2 shows the cell potential obtained during  $\text{CO}_2\text{RR}$  in the 0.5 M  $\text{KHCO}_3$  and pH 3 sulfate electrolytes, respectively. As expected, the cell potential increases in both electrolytes with the increasing total applied current density. Furthermore, the cell potential in pH 3 sulfate electrolyte remains lower than the cell potential in 0.5 M  $\text{KHCO}_3$ . This is likely due to the higher ionic conductivity of the pH 3 electrolyte. (Specifically, the ionic conductivity of  $1.167 \times 10^{-1} \text{ S cm}^{-1}$  in pH 3 with the presence of 0.25M  $\text{K}_2\text{SO}_4$  is higher than the ionic conductivity of  $5.895 \times 10^{-2} \text{ S cm}^{-1}$  in 0.5 M  $\text{KHCO}_3$  despite the subtle electrolyte component change which occurs after  $\text{CO}_2$  saturation.)



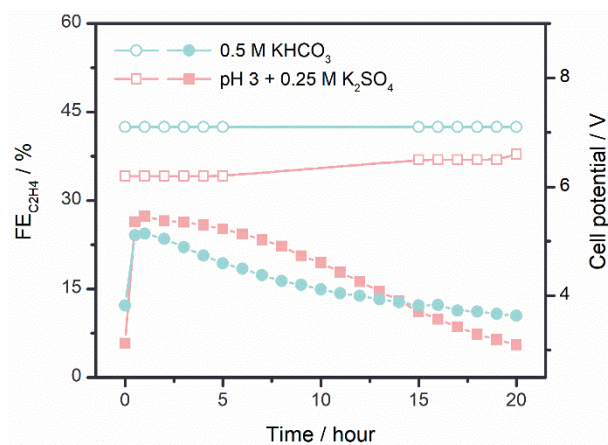
**Figure 5.3** Partial current densities of H<sub>2</sub>, HCOOH, CO, CH<sub>4</sub> and C<sub>2+</sub> products (C<sub>3</sub>H<sub>8</sub>OH, C<sub>2</sub>H<sub>5</sub>OH and C<sub>2</sub>H<sub>4</sub>) as a function of total applied current density on Cu GDE in CO<sub>2</sub> saturated a) 0.5M KHCO<sub>3</sub> (pH 7.2) and b) 0.25M K<sub>2</sub>SO<sub>4</sub> (pH 3.0).

Figure 5.3 shows the partial current densities of each CO<sub>2</sub>RR product in both electrolytes. It clearly shows higher CO production in pH 3 electrolyte for lower total applied current densities, and similar product distributions in both electrolytes at higher total applied current densities. We ascribe this to the local pH regulation which is different between these two electrolytes at these lower current densities.

To study the stability of both electrolysis systems, long term electrolysis of CO<sub>2</sub>RR at a total applied current density of 200 mA cm<sup>-2</sup> was performed on the Cu GDE in both electrolytes. The FE of C<sub>2</sub>H<sub>4</sub> and the cell potential were chosen as indicators of CO<sub>2</sub>RR performance. Left and right axis of Figure 5.4 shows FE of C<sub>2</sub>H<sub>4</sub> (solid symbols) and cell potential (hollow symbols), respectively, as a function of time, in 0.5 KHCO<sub>3</sub> (green) and pH 3 electrolyte with presence of 0.25 M K<sub>2</sub>SO<sub>4</sub> (pink). The results show that the cell potential in 0.5M KHCO<sub>3</sub> is more stable than in the pH 3 electrolyte. On the other hand, the FE of C<sub>2</sub>H<sub>4</sub> in pH 3



electrolyte remains higher than in 0.5 M  $\text{KHCO}_3$  for 14 hours (and especially for the first 8 hours).



**Figure 5.4** Comparison of  $\text{CO}_2\text{RR}$  performance at a total applied current density of  $200 \text{ mA cm}^{-2}$  on a Cu GDE in neutral and acidic bulk electrolyte: solid symbols representing FE of  $\text{C}_2\text{H}_4$  corresponding to left axis and hollow symbols representing cell potential corresponding to right axis. Electrolytes: 0.5  $\text{KHCO}_3$  (green) and pH 3 electrolyte with presence of 0.25M  $\text{K}_2\text{SO}_4$  (pink).

These results suggest that although less  $\text{KHCO}_3$  precipitation is expected in pH 3 electrolyte, it does not necessarily lead to stable  $\text{CO}_2\text{RR}$  performance during long term electrolysis. Considering the fact that bulk pH before and after  $\text{CO}_2\text{RR}$  electrolysis remain relatively stable (see Table S1) and  $\text{CO}_2\text{RR}$  performance derived from long term electrolysis slowly went down over time, we assume that the loss of  $\text{CO}_2\text{RR}$  activity likely stems from electrode degradation during long term electrolysis.

To test our hypothesis, copper GDEs were characterized after long term electrolysis. The copper GDEs were rinsed with Milli-Q water at least three times and dried in the air immediately after long term electrolysis. Next, they were kept in sealed sample bags prior to SEM characterization. Figure 5.5 shows the characterization of copper GDEs after 20 hours electrolysis at a total applied current density of  $200 \text{ mA cm}^{-2}$  in 0.5M  $\text{KHCO}_3$  and pH 3 sulfate electrolytes, respectively. Figure 5.5a, b show that surface catalysts remain as nanoparticles after long term  $\text{CO}_2\text{RR}$  experiments in both electrolytes. Figures 5.5c, d show

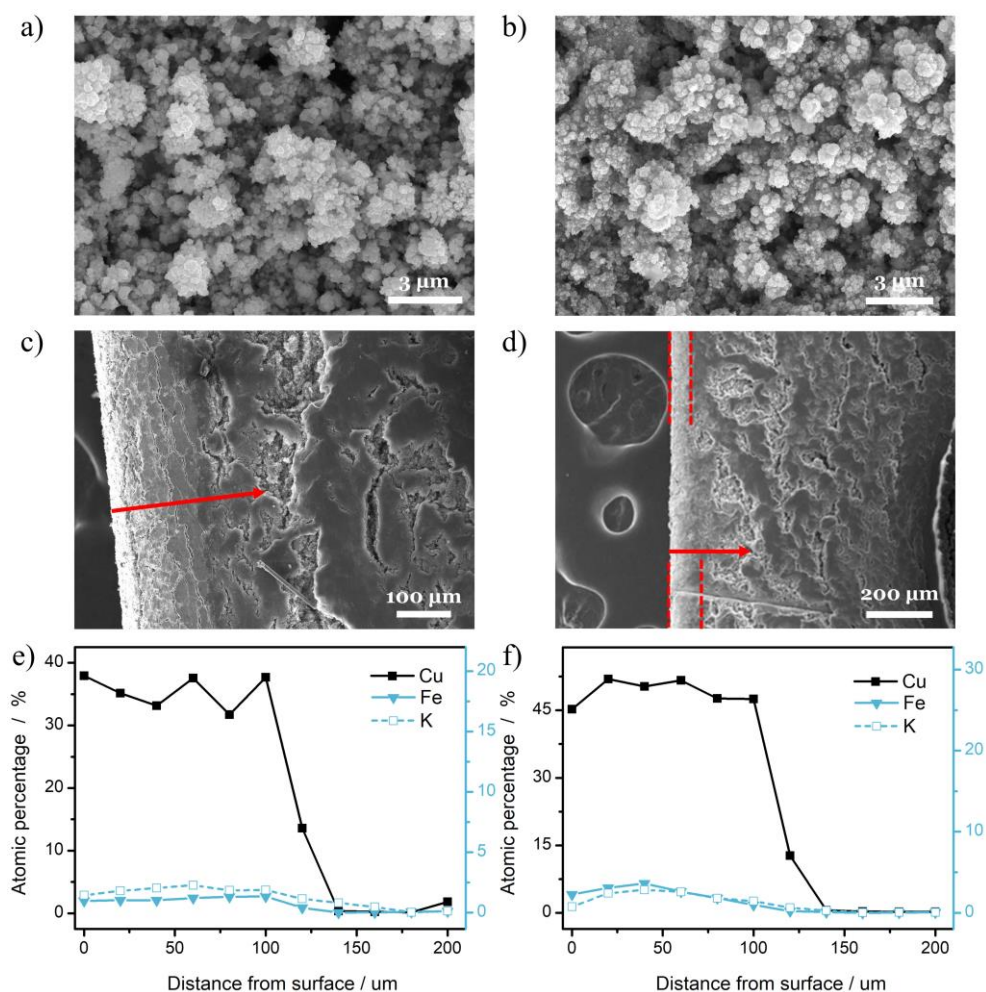


**Figure 5.5** Characterization of copper GDEs after 20 hours long term electrolysis at a total applied current density of  $200 \text{ mA cm}^{-2}$ . a) Surface catalyst morphology, c) cross section and e) atomic percentages of Cu, K, Fe as a function of distance from top surface of catalyst layer obtained from EDX elemental mapping of a copper GDE after long term electrolysis in  $\text{CO}_2$  saturated  $0.5 \text{ M KHCO}_3$ ; b) Surface catalyst morphology, d) cross section and f) atomic percentages of element Cu, K, Fe as a function of distance from top surface of catalyst layer obtained from EDX elemental mapping of a copper GDE after long term electrolysis in  $\text{CO}_2$  saturated pH 3 electrolyte with presence of  $0.25 \text{ M K}_2\text{SO}_4$ .

the cross section of the Cu GDEs after long term electrolysis in  $0.5 \text{ M KHCO}_3$  and  $0.25 \text{ M K}_2\text{SO}_4$  electrolytes, respectively. Figure 5.5c shows a well-preserved catalyst layer (around  $100 \text{ μm}$ ) on GDE after long term electrolysis in  $0.5 \text{ M KHCO}_3$ . On the other hand, it appears that the catalyst layer on copper GDE after long term electrolysis in pH 3  $\text{K}_2\text{SO}_4$  electrolyte was less intact, as shown by different distances between dashed lines in Figure 5.5d, which is

obtained from EDX mapping and indicates different thickness of the catalyst layer at different locations of the GDE. Supporting Figures D.1 and D.2 show further SEM images of the Cu GDE with catalyst layers of less than 50  $\mu\text{m}$  and images of copper GDEs with a black deposit on the current collector respectively, which suggests a redeposition of Cu nanoparticles on the current collector during  $\text{CO}_2\text{RR}$  in the pH 3 electrolyte. In addition to the loss of Cu nanoparticles, the presence of  $\text{KHCO}_3$  precipitation and Fe deposition originally from current collector (steel) in the catalyst layer are often considered as common reasons for causing loss of  $\text{CO}_2\text{RR}$  activity. Therefore, the atomic percentages of Cu (left axis), Fe (right axis) and K (right axis) obtained from EDX mapping along the arrow indicated in Figures 5.5c, d were obtained and are shown in Figure 5.5e, f respectively, with the positions chosen to have similar thicknesses of the catalyst layer. Figure 5.5e shows the presence of K throughout the catalyst layer as well as traces of Fe. In contrast, Figure 5.5f shows the presence of elements K and Fe in the top part of the catalyst layer. Additionally, it is worth noting that element Fe is higher on copper GDE after electrolysis in pH 3 sulfate electrolyte than on copper GDE after electrolysis in 0.5 M  $\text{KHCO}_3$  in view of the ratio of atomic level of Fe and Cu in each GDE, which suggests more Fe deposition on the catalyst layer in pH 3 sulfate electrolyte under our working conditions.

### 5.3.2 Discussion

Our work shows that operating in acidic media is a promising method to decrease the  $\text{CO}_2$  consumption caused by electrolyte without harming other important figures of merit such as the product distribution and electrode stability. Specifically, total FEs of  $\text{CO}_2\text{RR}$  products reach 80% on Cu GDE at total applied current densities of 200 and 250  $\text{mA cm}^{-2}$  in both electrolytes. In the meantime, similar  $\text{CO}_2\text{RR}$  product distributions were observed under these conditions. However, electrolytes with different bulk pH affect the  $\text{CO}_2\text{RR}$  product distribution at low total applied current densities. In pH 3 electrolyte, CO and HCOOH are the main products, while  $\text{H}_2$  and HCOOH are more pronounced in 0.5 M  $\text{KHCO}_3$ , at the total applied current densities of 10 and 50  $\text{mA cm}^{-2}$ . Additionally, minor  $\text{C}_2^+$  products were observed in pH 3 electrolyte at a total applied current density of 10  $\text{mA cm}^{-2}$ .

Previous work has shown that the selectivity and activity of a catalyst is highly sensitive to local pH<sup>19-23</sup> and cations<sup>24-27</sup>. Numerous experimental studies have shown that higher local pH conditions promote CO and multi-carbon products while suppressing H<sub>2</sub> and CH<sub>4</sub> on Cu catalysts.<sup>12, 20-23</sup> In addition to the pH of the bulk electrolyte, buffer capacity of the electrolyte also plays an import role on the local pH during CO<sub>2</sub>RR.<sup>8, 22-23, 28</sup> Liu et al shows dramatic change of local pH in low buffered electrolytes with a rotating ring-disk electrode.<sup>28</sup> Burdyny et al investigated the pH near the GDE as a function of total applied current density during CO<sub>2</sub>RR in commonly-used electrolytes, namely 0.1M KHCO<sub>3</sub>, 1M KHCO<sub>3</sub> and 1M KCl, with a 1D reaction-diffusion model.<sup>8</sup> The modelling shows a sudden increase of the local pH in the electrolytes with low buffer capacities at low current densities, which thereby leads to a high local pH in the low buffered electrolyte, and a similar ultimate alkaline local pH in all electrolytes (except a high local pH in high alkaline electrolyte) at high total applied current densities.<sup>8</sup>

These observations are in line with our experimental results. Considering the same cation concentration in both electrolytes and electrodes with the same preparation method in the present work, the observed different product distribution at low total applied current densities must be due to different local environment at the interface resulting from electrolyte. At low total applied current densities, HCO<sub>3</sub><sup>-</sup> acts as a buffer species and a proton donor contributing to the H<sub>2</sub> production in 0.5 M KHCO<sub>3</sub>. On the other hand, the rapidly increased local pH at the interface in low buffered pH 3 electrolyte leads to an inhibition of H<sub>2</sub> production because of the sluggish kinetics for water reduction in alkaline conditions. Under high total applied current densities, highly alkaline local environments at the interface are achieved, where HCO<sub>3</sub><sup>-</sup> is consumed by excess OH<sup>-</sup> formed during CO<sub>2</sub>RR and no long acts as buffer at the interface. Consequently, a similar local environment at the interface is expected in both electrolytes. Therefore, a similar products distribution in both electrolytes are observed.

Although alkaline local environments at the interface are unavoidable in both electrolytes, less carbonate/bicarbonate are expected during the reaction as the bulk protons can to some extent neutralize the OH<sup>-</sup> produced upon CO<sub>2</sub>RR while in alkaline media both OH<sup>-</sup> originated

from bulk electrolyte and generated from CO<sub>2</sub>RR will be neutralized by CO<sub>2</sub>. Our results shows that K<sup>+</sup>, which corresponds to carbonate/bicarbonate formation, is present in the catalysts layer after long term electrolysis in 0.5M KHCO<sub>3</sub> at a slightly higher level than in pH 3 electrolyte. In addition to K<sup>+</sup>, a higher content of Fe element, which is considered as metal impurity,<sup>15, 29</sup> was observed on copper GDE after long term electrolysis in pH 3 electrolyte compared to 0.5M KHCO<sub>3</sub> electrolyte. This may be related to the higher instability of the current collector under acid conditions. However, the observed elemental difference does not seem high enough to explain CO<sub>2</sub>RR performance over long term, as shown in Figure 5.4.

SEM characterization and EDX elemental mapping suggests a less stable catalyst layer in pH 3 electrolyte, which may be another factor contributing to the drop in CO<sub>2</sub>RR performance in pH 3 electrolyte. It is known that Cu can be easily oxidized at open circuit potential. The formed Cu oxide dissolves in the acidic media and may be subsequently reduced back to Cu during electrolysis, which thereby leads to a less stable catalyst layer over long term electrolysis in pH 3 electrolyte. Further, this could also explain the black deposition on current collector after electrolysis. Therefore, we show the unavoidable interactions between the acidic reagent and the commonly used compartments, e.g. GDE, may result in inherently unstable CO<sub>2</sub>RR electrolyzers.

## 5.4 Conclusions

In summary, we show that operating CO<sub>2</sub>RR in acidic media is a promising approach to lower the CO<sub>2</sub> consumption and improve the energy efficiency without compromising the selectivity toward C<sub>2+</sub> products. Compared with commonly used bicarbonate electrolytes, our results in mild acidic electrolyte show an inhibition of H<sub>2</sub> production at low total applied current densities and similar CO<sub>2</sub>RR product distribution at high total applied current densities. The similar CO<sub>2</sub>RR product distributions at high total applied current densities in both electrolytes indicate a similar local pH at the interface under these conditions. In addition, our result shows the unavoidable interaction between the acidic electrolyte and Cu oxide may result in inherently unstable Cu catalyst layer on GDE. Our work thereby offers

new insights of CO<sub>2</sub>RR in acidic media and points out the new challenge of employing acidic media in CO<sub>2</sub>RR electrolyzers.

## References

1. Kuhl, K. P.; Cave, E. R.; Abram, D. N.; Jaramillo, T. F., New insights into the electrochemical reduction of carbon dioxide on metallic copper surfaces. *Energy Environ. Sci.* **2012**, *5* (5), 7050-7059.
2. Hatsukade, T.; Kuhl, K. P.; Cave, E. R.; Abram, D. N.; Jaramillo, T. F., Insights into the electrocatalytic reduction of CO<sub>2</sub> on metallic silver surfaces. *Phys. Chem. Chem. Phys.* **2014**, *16* (27), 13814-9.
3. Min, X.; Kanan, M. W., Pd-catalyzed electrohydrogenation of carbon dioxide to formate: high mass activity at low overpotential and identification of the deactivation pathway. *J. Am. Chem. Soc.* **2015**, *137* (14), 4701-8.
4. Cave, E. R.; Montoya, J. H.; Kuhl, K. P.; Abram, D. N.; Hatsukade, T.; Shi, C.; Hahn, C.; Nørskov, J. K.; Jaramillo, T. F., Electrochemical CO<sub>2</sub> reduction on Au surfaces: mechanistic aspects regarding the formation of major and minor products. *Phys. Chem. Chem. Phys.* **2017**, *19* (24), 15856-15863.
5. De Luna, P.; Hahn, C.; Higgins, D.; Jaffer, S. A.; Jaramillo, T. F.; Sargent, E. H., What would it take for renewably powered electrosynthesis to displace petrochemical processes? *Science* **2019**, *364* (6438).
6. Philips, M. F.; Gruter, G.-J. M.; Koper, M. T. M.; Schouten, K. J. P., Optimizing the Electrochemical Reduction of CO<sub>2</sub> to Formate: A State-of-the-Art Analysis. *ACS Sustainable Chemistry & Engineering* **2020**, *8* (41), 15430-15444.
7. Monteiro, M. C. O.; Philips, M. F.; Schouten, K. J. P.; Koper, M. T. M., Efficiency and selectivity of CO<sub>2</sub> reduction to CO on gold gas diffusion electrodes in acidic media. *Nat. Commun.* **2021**, *12* (1), 1-7.
8. Burdyny, T.; Smith, W. A., CO<sub>2</sub> reduction on gas-diffusion electrodes and why catalytic performance must be assessed at commercially-relevant conditions. *Energy Environ. Sci.* **2019**, *12* (5), 1442-1453.
9. Zhang, X.; Li, J.; Li, Y. Y.; Jung, Y.; Kuang, Y.; Zhu, G.; Liang, Y.; Dai, H., Selective and High Current CO<sub>2</sub> Electro-Reduction to Multicarbon Products in Near-Neutral KCl Electrolytes. *J. Am. Chem. Soc.* **2021**, *143* (8), 3245-3255.
10. Huang, J. E.; Li, F.; Ozden, A.; Sedighian Rasouli, A.; Garcia de Arquer, F. P.; Liu, S.; Zhang, S.; Luo, M.; Wang, X.; Lum, Y.; Xu, Y.; Bertens, K.; Miao, R. K.; Dinh, C. T.; Sinton, D.; Sargent, E. H., CO<sub>2</sub> electrolysis to multicarbon products in strong acid. *Science* **2021**, *372* (6546), 1074-1078.
11. Gu, J.; Liu, S.; Ni, W.; Ren, W.; Haussener, S.; Hu, X., Modulating electric field distribution by alkali cations for CO<sub>2</sub> electroreduction in strongly acidic medium. *Nat. Catal.* **2022**, *5* (4), 268-276.
12. Dinh, C. T.; Burdyny, T.; Kibria, M. G.; Seifitokaldani, A.; Gabardo, C. M.; Garcia de Arquer, F. P.; Kiani, A.; Edwards, J. P.; De Luna, P.; Bushuyev, O. S.; Zou, C.; Quintero-Bermudez, R.; Pang, Y.; Sinton, D.; Sargent, E. H., CO<sub>2</sub> electroreduction to ethylene via hydroxide-mediated copper catalysis at an abrupt interface. *Science* **2018**, *360* (6390), 783-787.
13. Popović, S.; Smiljanić, M.; Jovanović, P.; Vavra, J.; Buonsanti, R.; Hodnik, N., Stability and degradation mechanisms of copper-based catalysts for electrochemical CO<sub>2</sub> reduction. *Angew. Chem.* **2020**, *132* (35), 14844-14854.
14. Rabinowitz, J. A.; Kanan, M. W., The future of low-temperature carbon dioxide electrolysis depends on solving one basic problem. *Nat. Commun.* **2020**, *11* (1), 5231.
15. Nwabara, U. O.; Cofell, E. R.; Verma, S.; Negro, E.; Kenis, P. J. A., Durable Cathodes and

Electrolyzers for the Efficient Aqueous Electrochemical Reduction of CO<sub>2</sub>. *ChemSusChem* **2020**, *13* (5), 855-875.

16. Ma, Z.; Yang, Z.; Lai, W.; Wang, Q.; Qiao, Y.; Tao, H.; Lian, C.; Liu, M.; Ma, C.; Pan, A.; Huang, H., CO<sub>2</sub> electroreduction to multicarbon products in strongly acidic electrolyte via synergistically modulating the local microenvironment. *Nat. Commun.* **2022**, *13* (1), 7596.
17. Ma, M.; Clark, E. L.; Therkildsen, K. T.; Dalsgaard, S.; Chorkendorff, I.; Seger, B., Insights into the carbon balance for CO<sub>2</sub> electroreduction on Cu using gas diffusion electrode reactor designs. *Energy Environ. Sci.* **2020**, *13* (3), 977-985.
18. Bondue, C. J.; Graf, M.; Goyal, A.; Koper, M. T. M., Suppression of Hydrogen Evolution in Acidic Electrolytes by Electrochemical CO<sub>2</sub> Reduction. *J. Am. Chem. Soc.* **2021**, *143* (1), 279-285.
19. Schouten, K. J. P.; Pérez Gallent, E.; Koper, M. T. M., The influence of pH on the reduction of CO and CO<sub>2</sub> to hydrocarbons on copper electrodes. *J. Electroanal. Chem.* **2014**, *716*, 53-57.
20. Lim, C. F. C.; Harrington, D. A.; Marshall, A. T., Effects of mass transfer on the electrocatalytic CO<sub>2</sub> reduction on Cu. *Electrochim. Acta* **2017**, *238*, 56-63.
21. Pander, J. E.; Ren, D.; Huang, Y.; Loo, N. W. X.; Hong, S. H. L.; Yeo, B. S., Understanding the Heterogeneous Electrocatalytic Reduction of Carbon Dioxide on Oxide - Derived Catalysts. *ChemElectroChem* **2017**, *5* (2), 219-237.
22. Kas, R.; Kortlever, R.; Yılmaz, H.; Koper, M. T. M.; Mul, G., Manipulating the Hydrocarbon Selectivity of Copper Nanoparticles in CO<sub>2</sub> Electroreduction by Process Conditions. *ChemElectroChem* **2014**, *2* (3), 354-358.
23. Varela, A. S.; Kroschel, M.; Reier, T.; Strasser, P., Controlling the selectivity of CO<sub>2</sub> electroreduction on copper: The effect of the electrolyte concentration and the importance of the local pH. *Catal. Today* **2016**, *260*, 8-13.
24. Resasco, J.; Chen, L. D.; Clark, E.; Tsai, C.; Hahn, C.; Jaramillo, T. F.; Chan, K.; Bell, A. T., Promoter Effects of Alkali Metal Cations on the Electrochemical Reduction of Carbon Dioxide. *J. Am. Chem. Soc.* **2017**, *139* (32), 11277-11287.
25. Singh, M. R.; Kwon, Y.; Lum, Y.; Ager, J. W., 3rd; Bell, A. T., Hydrolysis of Electrolyte Cations Enhances the Electrochemical Reduction of CO<sub>2</sub> over Ag and Cu. *J. Am. Chem. Soc.* **2016**, *138* (39), 13006-13012.
26. Perez-Gallent, E.; Marcandalli, G.; Figueiredo, M. C.; Calle-Vallejo, F.; Koper, M. T. M., Structure- and Potential-Dependent Cation Effects on CO Reduction at Copper Single-Crystal Electrodes. *J. Am. Chem. Soc.* **2017**, *139* (45), 16412-16419.
27. Ayemoba, O.; Cuesta, A., Spectroscopic Evidence of Size-Dependent Buffering of Interfacial pH by Cation Hydrolysis during CO<sub>2</sub> Electroreduction. *ACS Appl. Mater. Interfaces* **2017**, *9* (33), 27377-27382.
28. Liu, X.; Monteiro, M. C. O.; Koper, M. T. M., Interfacial pH measurements during CO<sub>2</sub> reduction on gold using a rotating ring-disk electrode. *Phys. Chem. Chem. Phys.* **2023**, *25* (4), 2897-2906.
29. Wuttig, A.; Surendranath, Y., Impurity Ion Complexation Enhances Carbon Dioxide Reduction Catalysis. *ACS Catal.* **2015**, *5* (7), 4479-4484.





# **A**

## **Supplementary Information for Chapter 2**

## A.1 The morphology of working electrodes before electrochemical experiments

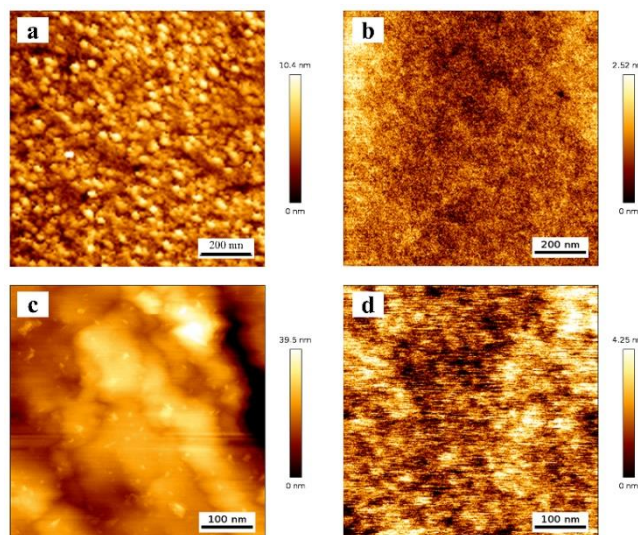


**Figure A.1** AFM images of (a) poly Cu, (b) P4VP-modified Cu, (c) poly Au and (d) P4VP-modified Au in the air before all experiments.

## A.2 Blank voltammetry and chronoamperometry experiments on unmodified and P4VP-modified pyrolytic graphite disk electrodes

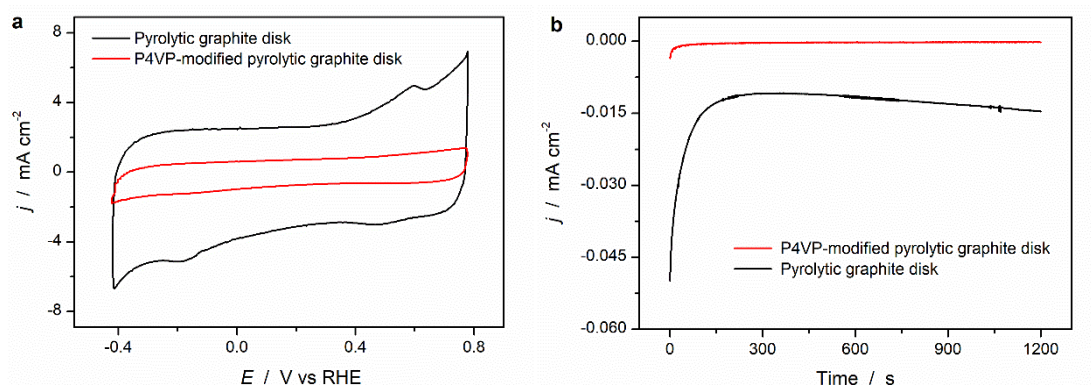


**Figure A.2** (a) Cyclic voltammograms with scan rate 50 mV/s, and (b) total current density of CO<sub>2</sub> reduction on P4VP modified pyrolytic graphite (red curve) and unmodified pyrolytic graphite electrodes (black curve) at -0.6 V vs RHE in CO<sub>2</sub> saturated 0.1 M KHCO<sub>3</sub> solution. With reversible hydrogen electrode as reference electrode. All potentials were IR corrected.

### A.3 Summary of vibrational bands assignments with different infrared spectroscopy

**Table A.1** Vibrational Assignments of the ATR-SEIRAS bands

Surface	Band center / $\text{cm}^{-1}$	Species	Method	assignment
1	2343	solution $\text{CO}_2$	IR	$\nu_{\text{COO}}$
Cu (110) <sup>2-3</sup>	2070	adsorbed CO on (100) or (111) step site	SNIFTIRS	
Cu (100) <sup>4</sup>	2050	adsorbed CO on (100) terrace	SNIFTIRS	
Cu single crystals, <sup>5</sup> poly Cu <sup>6</sup>	2001-1933	adsorbed CO on bridge site	SNIFTIRS	
7	1650	$\text{H}_2\text{O}$	IR	$\delta_{\text{HOH}}$
poly Au <sup>8</sup> and poly Cu <sup>9</sup>	1620	solution $\text{HCO}_3^-$	ATR-SEIRAS	$\nu_{\text{COO}}$ , asym
poly Cu <sup>9</sup>	1616-1608	adsorbed $\text{HCOO}^-$	ATR-SEIRAS	$\nu_{\text{COO}}$ , asym
poly Cu, <sup>9</sup> Cu(100), <sup>4</sup> Au(111) <sup>10</sup>	1533-1508	adsorbed $\text{CO}_3^{2-}$	FTIR, IRAS	$\nu_{\text{COO}}$ , asym
	1410	solution $\text{CO}_3^{2-}$	ATR	$\nu_{\text{COO}}$ , asym
Poly Cu, <sup>9</sup> Au(111) <sup>10</sup> and poly Au <sup>11</sup>	1365	solution $\text{HCO}_3^-$	ATR	$\nu_{\text{COO}}$ , sym
	1330	solution $\text{HCO}_3^-$	ATR-SEIRAS	

#### A.4 ATR-SEIRAS on poly Cu before adding P4VP layer

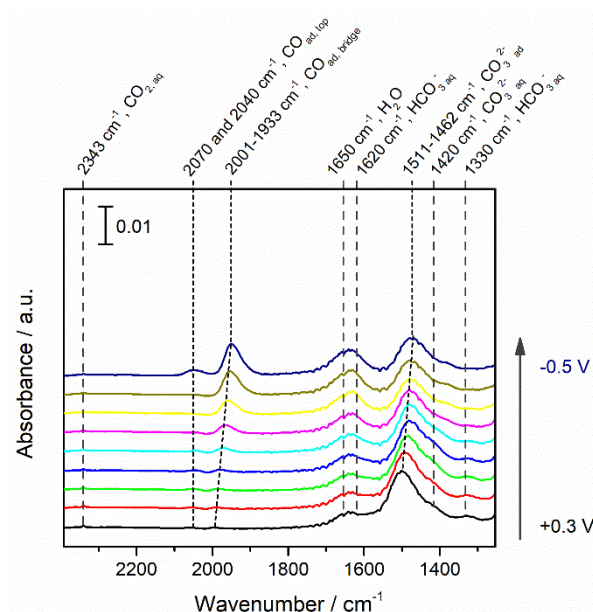


**Figure A.3** ATR-SEIRA spectra of CO<sub>2</sub>RR on poly Cu during linear sweep voltammetry at 1 mV/s from 0.3 V to -0.5 V vs RHE in CO<sub>2</sub> saturated 0.1M KHCO<sub>3</sub> aqueous solution. The background spectrum was taken at OCP in H<sub>2</sub>O before experiments. The potential interval between spectra is 0.1 V.

## A.5 ATR-SEIRAS on poly Au and P4VP-modified Au during CO<sub>2</sub>RR

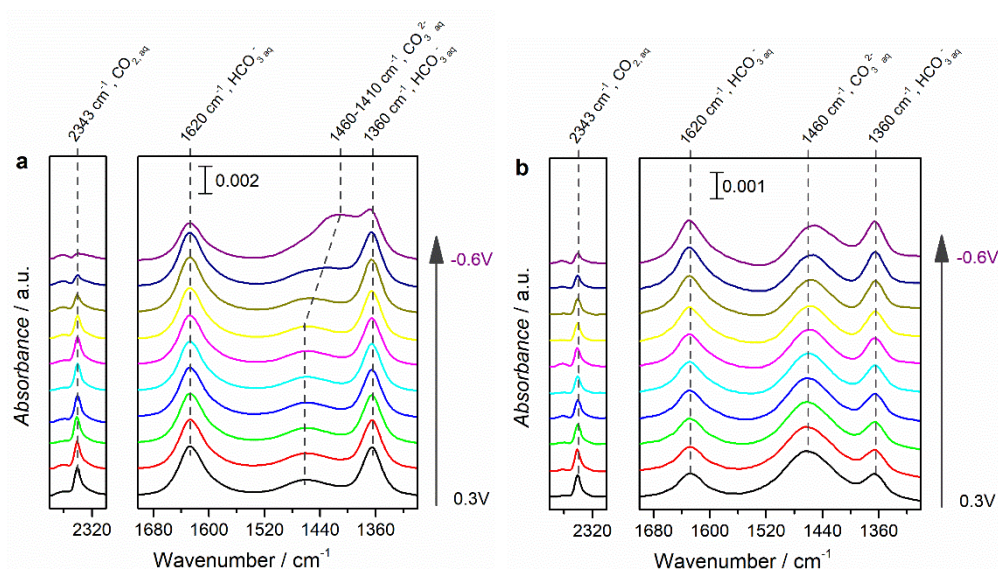


**Figure A.4** ATR-SEIRAS spectra of CO<sub>2</sub>RR on the poly Au (a) and P4VP-modified Au (b) during linear sweep voltammetry at 1 mV/s from 0.3 V to -0.6 V vs RHE in CO<sub>2</sub> saturated 0.05M K<sub>2</sub>CO<sub>3</sub> dissolved in D<sub>2</sub>O. The background spectrum was taken at OCP in D<sub>2</sub>O before experiments. The potential interval between spectra is 0.1 V.

The ratio of the integrals of the bands related to dissolved CO<sub>2</sub> and solution HCO<sub>3</sub><sup>-</sup> (2343 and 1620 cm<sup>-1</sup>, respectively;  $I_{\text{CO}_2} / I_{\text{HCO}_3^-}$ ) was calculated as an indicator of local environment. To avoid the influence of H<sub>2</sub>O bending band at 1650 cm<sup>-1</sup>, D<sub>2</sub>O was used to prepare the electrolyte. Bands related with dissolved CO<sub>2</sub>, solution HCO<sub>3</sub><sup>-</sup>, and solution CO<sub>3</sub><sup>2-</sup> on unmodified and P4VP-modified Au electrodes are shown in Figures A.4 a and b respectively. Additionally, the bands related with solution HCO<sub>3</sub><sup>-</sup> and solution CO<sub>3</sub><sup>2-</sup> (at 1360 and 1460 cm<sup>-1</sup>) show the same information of the different local environment changes on unmodified and P4VP-modified Au electrodes. When the potential went to -0.6 V vs RHE, the intensity of the band related with solution HCO<sub>3</sub><sup>-</sup> decreases, while the intensity of the band related with solution CO<sub>3</sub><sup>2-</sup> increases (compared with the bands intensity at 0.3 V vs RHE). Due to the growth of the broad band related with solution CO<sub>3</sub><sup>2-</sup>, bands at 1360 and 1460 cm<sup>-1</sup> overlap,

which slightly shifts the band center of solution  $\text{CO}_3^{2-}$ . However, this observation does not have any effect on bands assignment nor on the calculated value of  $I_{\text{CO}_2} / I_{\text{HCO}_3^-}$ .

## A.6 Contact angle measurements on the working electrodes before electrochemical experiments

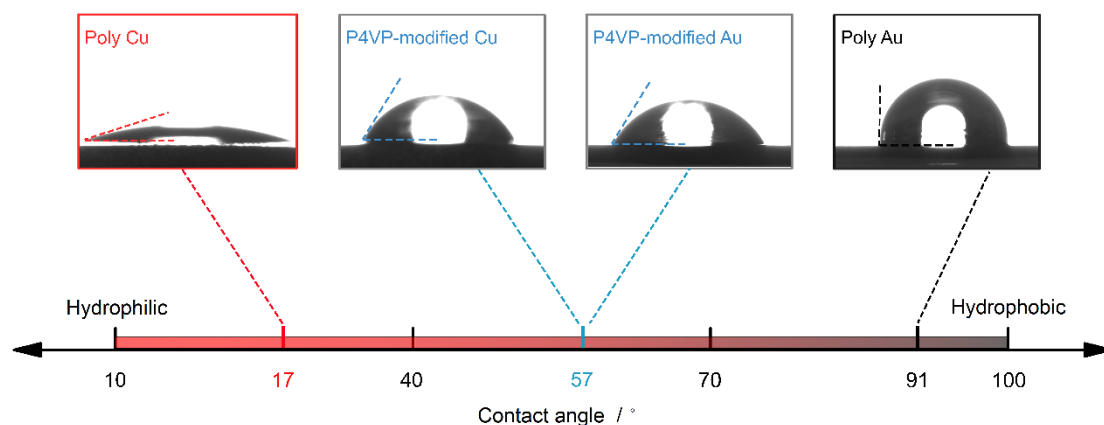


**Figure A.5** Water contact angles on poly Cu, P4VP-modified Cu, poly Au and P4VP-modified Au surfaces.

## A.7 Cyclic Voltammetry on P4VP-modified Cu and Au electrodes after CO<sub>2</sub>RR

Cyclic Voltammetry was employed to characterize the electrodes after CO<sub>2</sub>RR experiments. Although CO oxidation peak was observed on P4VP-modified Au electrode after CO<sub>2</sub>RR at -0.5 V vs RHE,<sup>12</sup> the cyclic voltammograms on both P4VP-modified Cu and Au electrodes exhibit minor changes after applying negative potentials, as shown in the following cyclic voltammograms of P4VP-modified Cu and Au electrodes. This result indicates the intactness of the P4VP layer on poly Cu and Au surfaces after CO<sub>2</sub>RR.

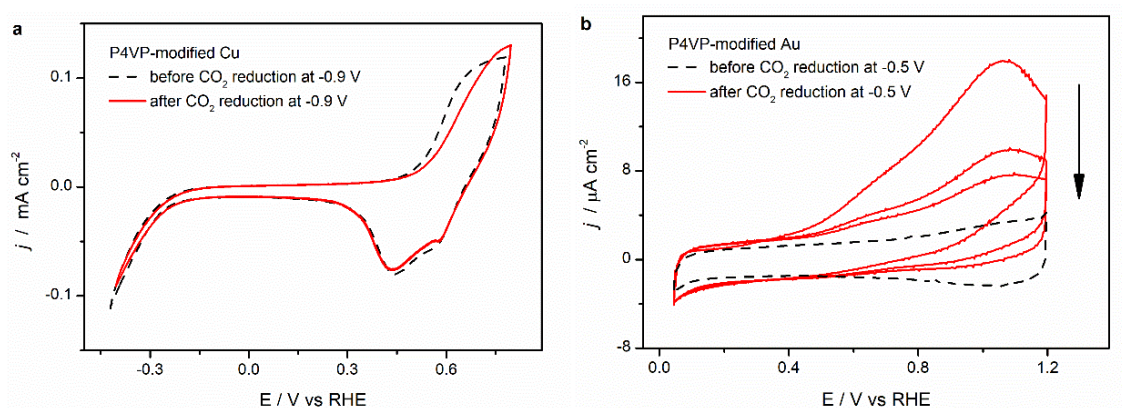


**Figure A.6** Cyclic voltammograms of (a) P4VP-modified Cu after CO<sub>2</sub>RR at -0.9 V vs RHE and (b) P4VP-modified Au after CO<sub>2</sub>RR at -0.5 V vs RHE, measured at 50 mV/s in CO<sub>2</sub> saturated 0.1 M KHCO<sub>3</sub> solution.



## References

1. Falk, M.; Miller, A. G., Infrared spectrum of carbon dioxide in aqueous solution. *Vib. Spectrosc* **1992**, *4*, 105-108.
2. Koga, O.; Teruya, S.; Matsuda, K.; Minami, M.; Hoshi, N.; Hori, Y., Infrared spectroscopic and voltammetric study of adsorbed CO on stepped surfaces of copper monocrystalline electrodes. *Electrochim. Acta* **2005**, *50* (12), 2475-2485.
3. Gunathunge, C. M.; Li, X.; Li, J.; Hicks, R. P.; Ovalle, V. J.; Waagele, M. M., Spectroscopic Observation of Reversible Surface Reconstruction of Copper Electrodes under CO<sub>2</sub> Reduction. *J. Phys. Chem. C* **2017**, *121* (22), 12337-12344.
4. Hori, Y.; Koga, O.; Watanabe, Y.; Matsuo, T., FTIR measurements of charge displacement adsorption of CO, on poly- and single crystal (100) of Cu electrodes. *Electrochim. Acta* **1998**, *44* (8-9), 1389-1395.
5. Shaw, S. K.; Berna, A.; Feliu, J. M.; Nichols, R. J.; Jacob, T.; Schiffrin, D. J., Role of axially coordinated surface sites for electrochemically controlled carbon monoxide adsorption on single crystal copper electrodes. *Phys. Chem. Chem. Phys.* **2011**, *13* (12), 5242-51.
6. Gunathunge, C. M.; Ovalle, V. J.; Li, Y.; Janik, M. J.; Waagele, M. M., Existence of an Electrochemically Inert CO Population on Cu Electrodes in Alkaline pH. *ACS Catal.* **2018**, *8* (8), 7507-7516.
7. Larsen, O. F.; Woutersen, S., Vibrational relaxation of the H<sub>2</sub>O bending mode in liquid water. *J. Chem. Phys.* **2004**, *121* (24), 12143-5.
8. Ayemoba, O.; Cuesta, A., Spectroscopic Evidence of Size-Dependent Buffering of Interfacial pH by Cation Hydrolysis during CO<sub>2</sub> Electroreduction. *ACS Appl. Mater. Interfaces* **2017**, *9* (33), 27377-27382.
9. Moradzaman, M.; Mul, G., Infrared Analysis of Interfacial Phenomena during Electrochemical Reduction of CO<sub>2</sub> over Polycrystalline Copper Electrodes. *ACS Catal.* **2020**, *10* (15), 8049-8057.
10. Arihara, K.; Kitamura, F.; Ohsaka, T.; Tokuda, K., Characterization of the adsorption state of carbonate ions at the Au(111) electrode surface using in situ IRAS. *J. Electroanal. Chem.* **2001**, *510*, 128-135.
11. Dunwell, M.; Yang, X.; Setzler, B. P.; Anibal, J.; Yan, Y.; Xu, B., Examination of Near-Electrode Concentration Gradients and Kinetic Impacts on the Electrochemical Reduction of CO<sub>2</sub> using Surface-Enhanced Infrared Spectroscopy. *ACS Catal.* **2018**, *8* (5), 3999-4008.
12. Marcandalli, G.; Villalba, M.; Koper, M. T. M., The Importance of Acid-Base Equilibria in Bicarbonate Electrolytes for CO<sub>2</sub> Electrochemical Reduction and CO Reoxidation Studied on Au(hkl) Electrodes. *Langmuir* **2021**, *37* (18), 5707-5716.

# **B**

## **Supplementary Information for Chapter 3**

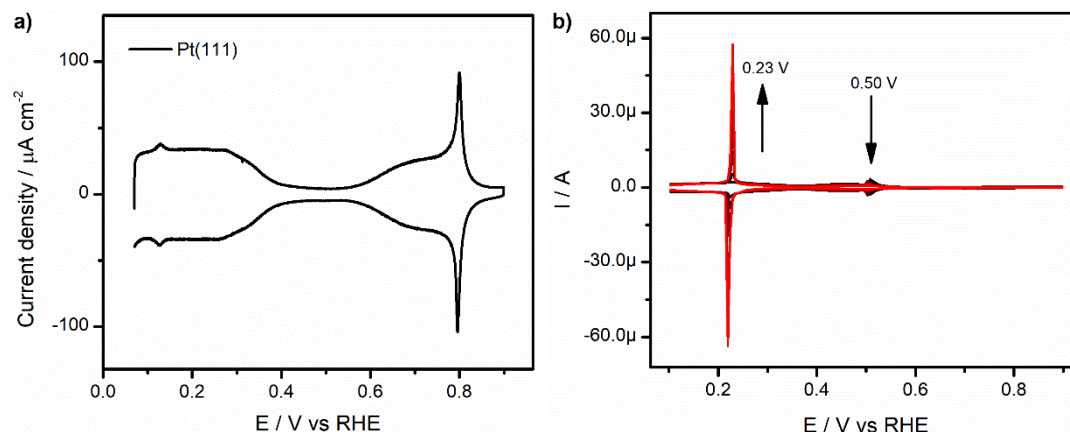


**Figure B.1** (a). Cyclic voltammogram of Pt(111) in 0.1 M HClO<sub>4</sub>. Scan rate: 50 mV s<sup>-1</sup>. (b). Cyclic voltammograms for Pt(111) in 0.1 M H<sub>2</sub>SO<sub>4</sub> + 0.1 mM PdSO<sub>4</sub>, recorded in successive stages during Pd deposition experiment. Scan rate: 50 mV s<sup>-1</sup>. Arrows indicate the evolution with time.

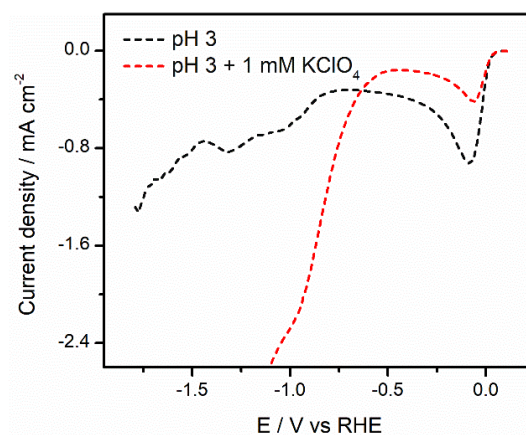


**Figure B.2** Linear Sweep Voltammetry of Pd<sub>ML</sub>Pt(111) in argon-purged pH 3 electrolytes in the absence (black) and presence of 1 mM KClO<sub>4</sub> (red). Scan rate: 10 mV/s.

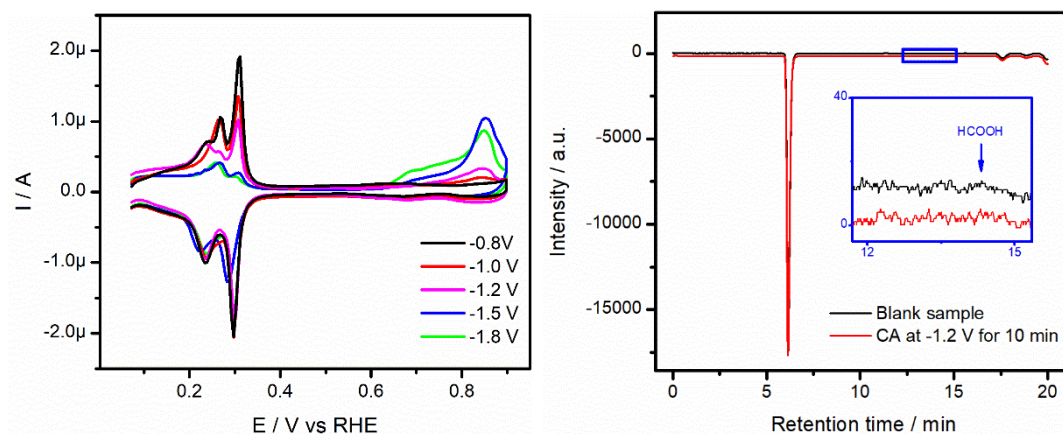


**Figure B.3** (a). CO stripping voltammograms on Pd<sub>ML</sub>Pt(111) after CO<sub>2</sub> reduction at different vertex potentials in CO<sub>2</sub>-saturated pH 3 electrolyte without metal cations, measured at 10 mV s<sup>-1</sup>. (b). HPLC data before and after chronoamperometry at -1.2 V<sub>RHE</sub> for 10 min in CO<sub>2</sub>-saturated pH 3 electrolyte without metal cations.

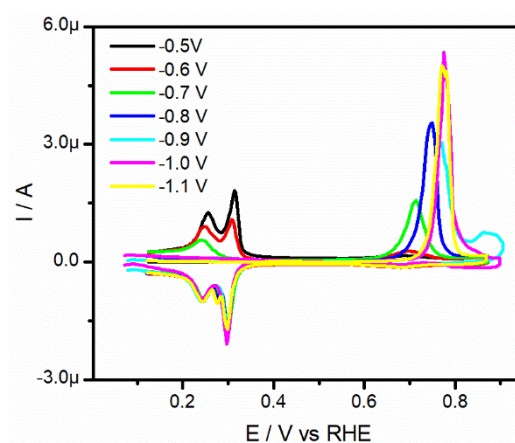


**Figure B.4** CO stripping voltammograms on Pd<sub>ML</sub>Pt(111) after CO<sub>2</sub> reduction at different vertex potentials in CO<sub>2</sub>-saturated pH 3 with 1 mM KClO<sub>4</sub> electrolyte, measured at 10 mV s<sup>-1</sup>.

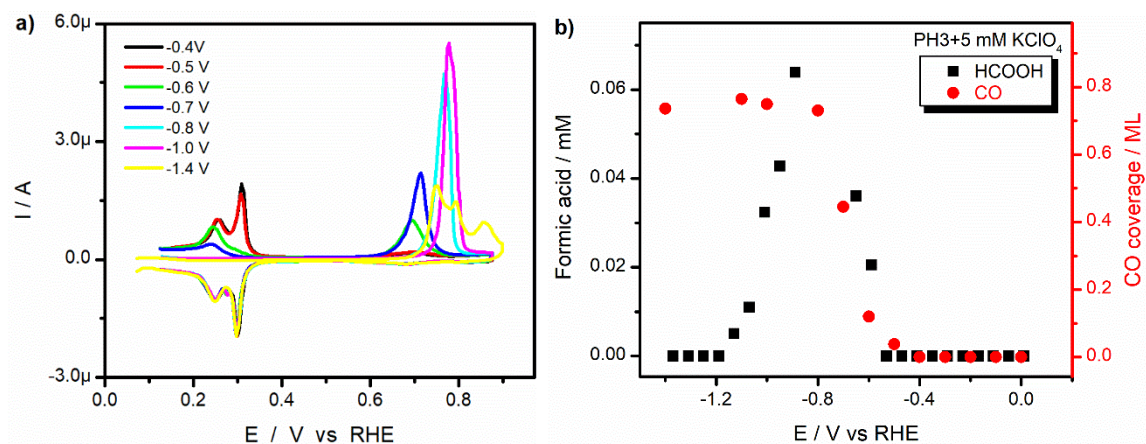


**Figure B.5** (a). CO stripping voltammograms on Pd<sub>ML</sub>Pt(111) after CO<sub>2</sub> reduction at different vertex potentials in CO<sub>2</sub>-saturated pH 3 with 5 mM KClO<sub>4</sub> electrolyte, measured at 10 mV s<sup>-1</sup>. (b). HCOOH formation and the calculated CO coverage as a function of potential.

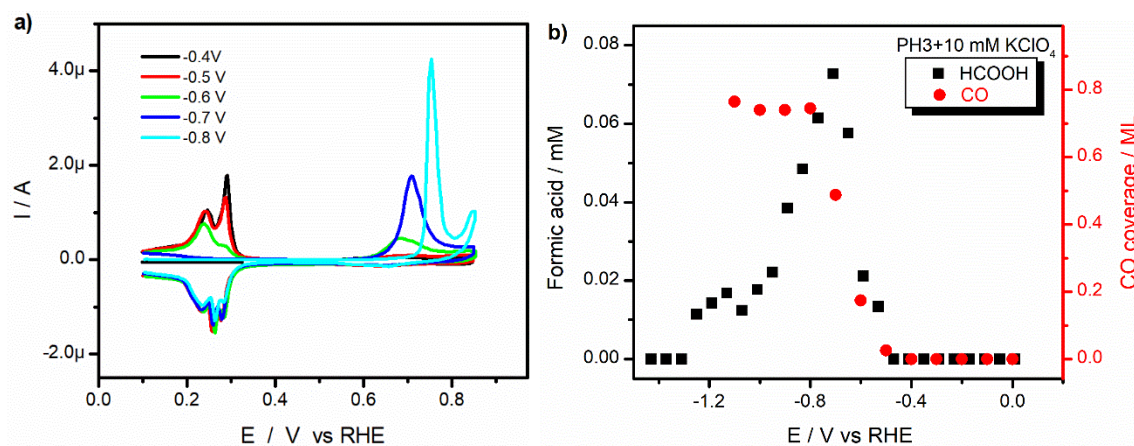


**Figure B.6** (a). CO stripping voltammograms on Pd<sub>ML</sub>Pt(111) after CO<sub>2</sub> reduction at different vertex potentials in CO<sub>2</sub>-saturated pH 3 with 10 mM KClO<sub>4</sub> electrolyte, measured at 10 mV s<sup>-1</sup>. (b). HCOOH formation and the calculated CO coverage as a function of potential.

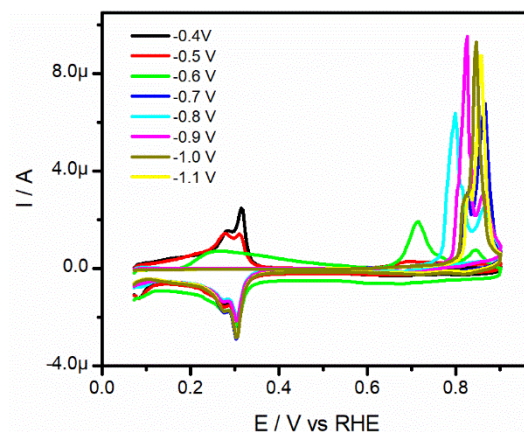


**Figure B.7** CO stripping voltammograms on Pd<sub>ML</sub>Pt(111) after CO<sub>2</sub> reduction at different vertex potentials in CO<sub>2</sub>-saturated pH 3 with 99 mM KClO<sub>4</sub> electrolyte, measured at 10 mV s<sup>-1</sup>.

Figures B.3a, B.4, B.5a, B.6a and B.7 show oxidative stripping voltammograms of adsorbed CO obtained during CO<sub>2</sub>RR by increasing the vertex potential in steps of 0.1 V from -0.4 V<sub>RHE</sub>. With the positive going scan, decreasing peaks (peak at 0.31 V<sub>RHE</sub> decreasing first) in the potential region between +0.05 and +0.35 V<sub>RHE</sub> suggest adsorbed CO. CO<sub>ads</sub> oxidation peaks are observed in the potential region between +0.65 and +0.9 V<sub>RHE</sub>, the peaks varying under different conditions. These different CO oxidation peaks may result from different \*CO coverage or changes of local electrolyte after CO<sub>2</sub>RR. After oxidation of \*CO, the typical CV features in pH 3 electrolyte are again observed in the negative going scan. In some voltammograms, CV features of Pd<sub>ML</sub>Pt(111) slightly deviate from the standard, which might be due to minor loss of Pd atoms during CO<sub>2</sub>RR. Moreover, peaks in the potential region between +0.05 and +0.35 V<sub>RHE</sub> decreases with increasing of \*CO obtained from CO<sub>2</sub>RR, which leads to more CO oxidation current in potential region between +0.65 and +0.9 V<sub>RHE</sub> and corresponding higher CO coverage.



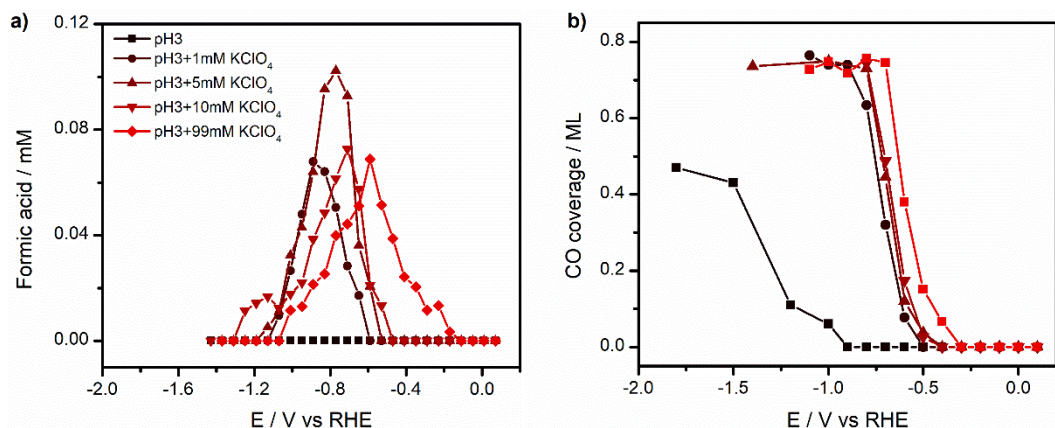


**Figure B.8** A summary of (a) formic acid and (b) CO generation during CO<sub>2</sub>RR in CO<sub>2</sub> saturated pH 3 electrolytes in the presence of 0, 1, 5, 10, 99 mM KClO<sub>4</sub>.

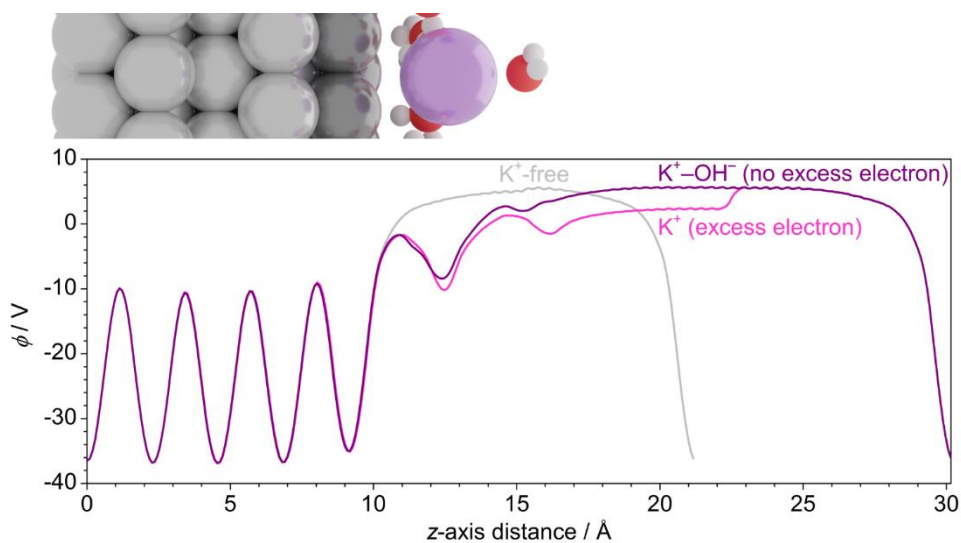


**Figure B.9** Electrostatic potential ( $\Phi$ ) profile across the simulation cell ( $z$ -direction, reported on top) for the cation-free (gray line) and near-cation ( $d_{K^+-surf} = 4 \text{ \AA}$ ) systems with and without excess electron (magenta and purple line respectively).

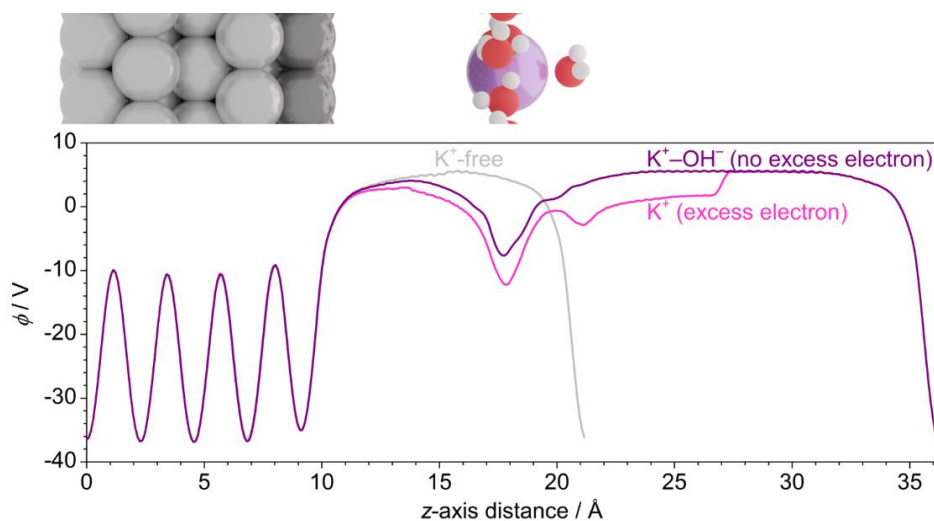


**Figure B.10** Electrostatic potential ( $\Phi$ ) profile across the simulation cell ( $z$ -direction, reported on top) for the cation-free (gray line) and far-cation ( $d_{\text{K}^+-\text{surf}} = 9 \text{ \AA}$ ) systems with and without excess electron (magenta and purple line respectively).

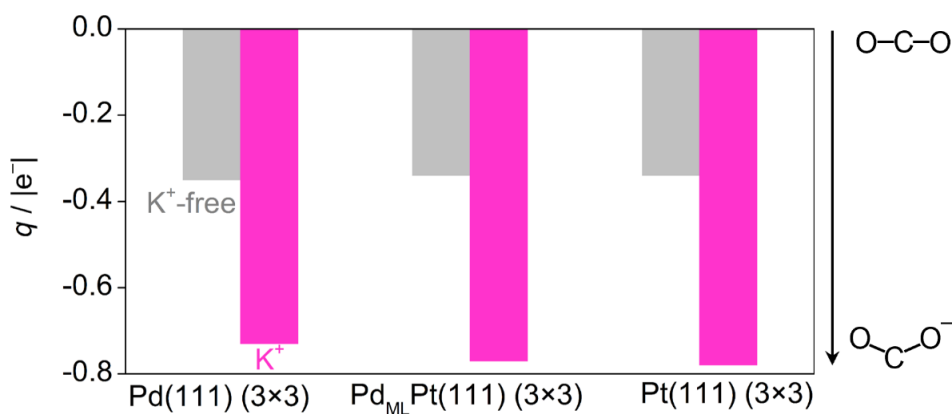


**Figure B.11** Bader charges for adsorbed  $\text{CO}_2^-$  on Pd(111) (3 $\times$ 3), Pd<sub>ML</sub>Pt(111) (3 $\times$ 3), and Pt(111) (3 $\times$ 3). The gray column reports the baseline case for the adsorbate without  $\text{K}^+$ , while the near- $\text{K}^+$  system (with excess electron) is indicated in magenta. Solvated  $\text{K}^+$  was here simulated with three water molecules within its coordination shell.



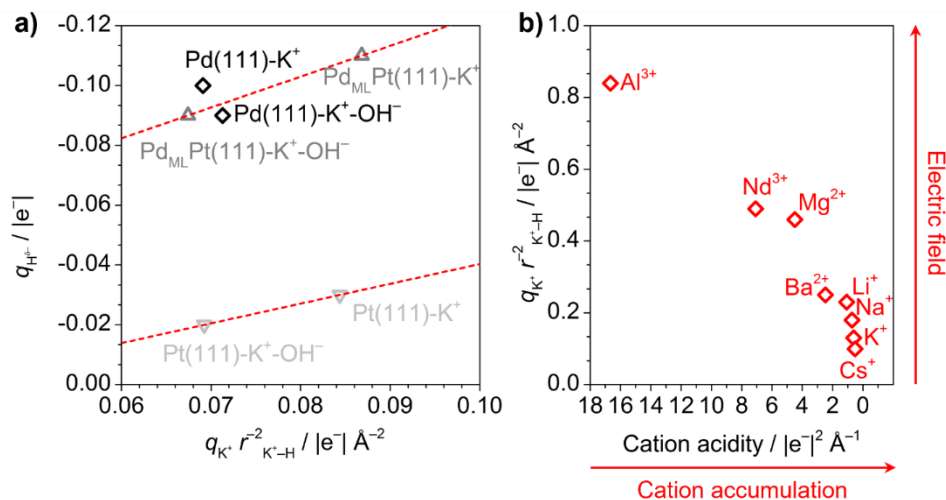


**Figure B.12** (a). Correlation between  $\text{H}^{\delta-}$  Bader charges and cation-induced electric field, proportional to  $q^{\text{K}^+}/r_{\text{K}^+-\text{H}}^2$ . (b). Cation-induced electric field vs cation acidity for alkali, bi-valent, and tri-valent cations. Cation acidity affects cation accumulation, while electric field favors the formation of hydrides on the surface. The distance between cation and hydrogen is here taken as the state-of-the-art cation-water distance reported for solvated cations (see Table B.3).<sup>5-6</sup>

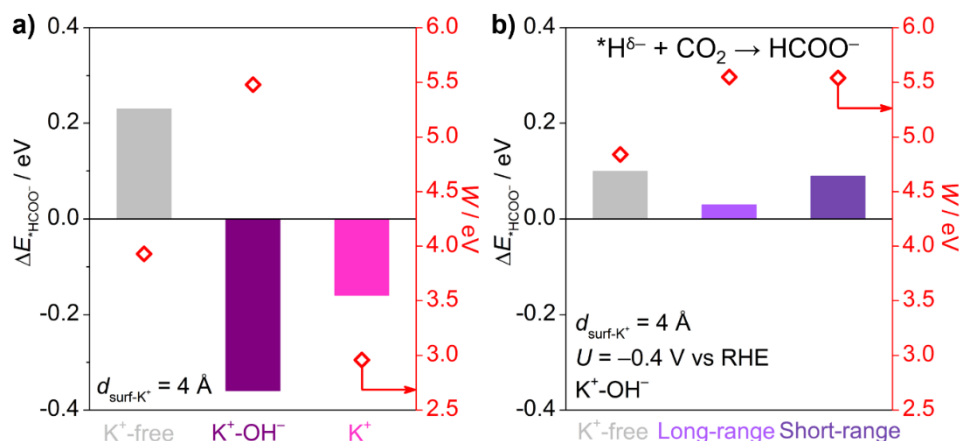


**Figure B.13** (a). DFT energy on Pd<sub>ML</sub>Pt(111) (3×3) relative to cation-induced outer-sphere CO<sub>2</sub> activation to HCOO<sup>-</sup> for the K<sup>+</sup>-free (gray) and near-K<sup>+</sup> with and without balancing OH<sup>-</sup> (purple and magenta) for different values of metal work functions (right y-axis). (b). DFT energy relative to the HCOO<sup>-</sup> formation step on Pd<sub>ML</sub>Pt(111) (3×3) supercell for cation-free (gray), far-K<sup>+</sup> (light purple), and near-K<sup>+</sup> (dark purple) cases at  $U = -0.4 \text{ V vs RHE}$ . Values of metal work function for clean surfaces are given at the right y-axis. For details on the model, see Figure 3.5a-b and Computational Details.

**Table B.1** Calculated work function for the Pd<sub>ML</sub>Pt(111) (3×3) surface for clean surface and \*CO<sub>2</sub> for the K<sup>+</sup>-free, the near-K<sup>+</sup> ( $d_{K^+-surf} = 4 \text{ \AA}$ ), and far-K<sup>+</sup> ( $d_{K^+-surf} = 9 \text{ \AA}$ ) cases, with and without balancing OH<sup>-</sup>. Cation and H<sub>2</sub>O molecules (within bracket) were absent in the K<sup>+</sup>-free case.

System	$W / \text{eV}$				
	K <sup>+</sup> -free	Near K <sup>+</sup>	Near K <sup>+</sup> + OH <sup>-</sup>	Far K <sup>+</sup>	Near K <sup>+</sup> + OH <sup>-</sup>
Clean surface	+4.84	+2.35	+5.54	+1.74	+5.55
*CO <sub>2</sub> <sup>-</sup> (+ K <sup>+</sup> + 5H <sub>2</sub> O)	+5.05	+5.09	+5.59	+5.14	+5.41

**Table B.2** Calculated Bader charges of the Pd<sub>ML</sub>Pt(111) (3×3) surface for clean surface and \*CO<sub>2</sub> for the K<sup>+</sup>-free, the near-K<sup>+</sup> ( $d_{K^+-surf} = 4 \text{ \AA}$ ), and far-K<sup>+</sup> ( $d_{K^+-surf} = 9 \text{ \AA}$ ) cases, with and without balancing OH<sup>-</sup>. Cation and H<sub>2</sub>O molecules (within brackets) were absent in the K<sup>+</sup>-free case.

System	$q_{surf} /  e^- $				
	K <sup>+</sup> -free	Near-K <sup>+</sup>	Near K <sup>+</sup> + OH <sup>-</sup>	Far K <sup>+</sup>	Near K <sup>+</sup> + OH <sup>-</sup>
Clean surface	+0.00	-0.62	-0.24	-0.05	-0.05
*CO <sub>2</sub> <sup>-</sup> (+ K <sup>+</sup> + 5H <sub>2</sub> O)	+0.35	-0.07	+0.29	+0.30	+0.30

**Table B.3** Properties of alkali, bi-valent, and tri-valent cations, taken from Refs. <sup>5-8</sup>.

Cation	$q_{cat} /  e^- $	ionic radius / $\text{\AA}$	$d_{cat-O} / \text{\AA}$	Acidity / $ e^- ^2 \text{\AA}^{-1}$	$q_{cat} / r_{cat-O}^2 /  e^-  \text{\AA}^{-2}$
Li <sup>+</sup>	1	0.92	2.08	1.09	0.23
Na <sup>+</sup>	1	1.39	2.36	0.72	0.18
K <sup>+</sup>	1	1.64	2.80	0.61	0.13
Cs <sup>+</sup>	1	1.88	3.14	0.53	0.10
Mg <sup>2+</sup>	2	0.89	2.09	4.49	0.46
Ba <sup>2+</sup>	2	1.61	2.81	2.48	0.25
Al <sup>3+</sup>	3	0.54	1.89	16.67	0.84
Nd <sup>3+</sup>	3	1.27	2.47	7.09	0.49

## References

1. McCrum, I. T.; Koper, M. T. M., The role of adsorbed hydroxide in hydrogen evolution reaction kinetics on modified platinum. *Nature Energy* **2020**, 5 (11), 891-899.
2. Monteiro, M. C.; Dattila, F.; Hagedoorn, B.; García-Muelas, R.; López, N.; Koper, M., Absence of CO<sub>2</sub> electroreduction on copper, gold and silver electrodes without metal cations in solution. *Nat. Catal.* **2021**, 4 (8), 654-662.
3. Chan, K.; Nørskov, J. K., Potential Dependence of Electrochemical Barriers from ab Initio Calculations. *J. Phys. Chem. Lett.* **2016**, 7 (9), 1686-1690.
4. Chan, K.; Nørskov, J. K., Electrochemical Barriers Made Simple. *J. Phys. Chem. Lett.* **2015**, 6 (14), 2663-2668.
5. Monteiro, M. C. O.; Dattila, F.; Lopez, N.; Koper, M. T. M., The Role of Cation Acidity on the Competition between Hydrogen Evolution and CO<sub>2</sub> Reduction on Gold Electrodes. *J. Am. Chem. Soc.* **2022**, 144 (4), 1589-1602.
6. Marcus, Y., Ionic radii in aqueous solutions. *Chem. Rev.* **1988**, 88 (8), 1475-1498.
7. Haynes, W. M., *CRC handbook of chemistry and physics*. CRC press: 2016.
8. Waagele, M. M.; Gunathunge, C. M.; Li, J.; Li, X., How cations affect the electric double layer and the rates and selectivity of electrocatalytic processes. *J. Chem. Phys.* **2019**, 151 (16), 160902.



# C

## **Supplementary Information for Chapter 4**

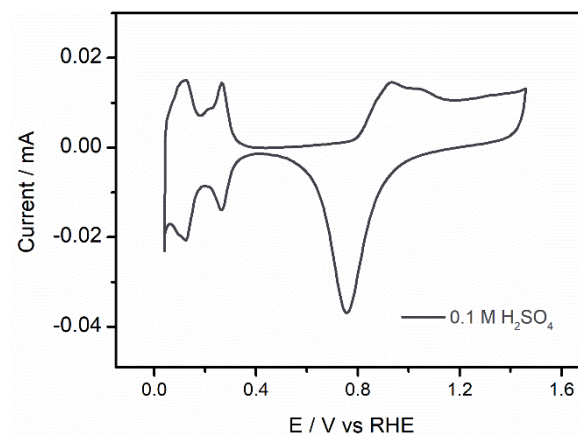


**Figure C.1** Cyclic voltammetry of the polycrystalline Pt rotation disk electrode after electrochemical polishing in 0.1 M  $\text{H}_2\text{SO}_4$ , scan rate:  $50 \text{ mV s}^{-1}$ .

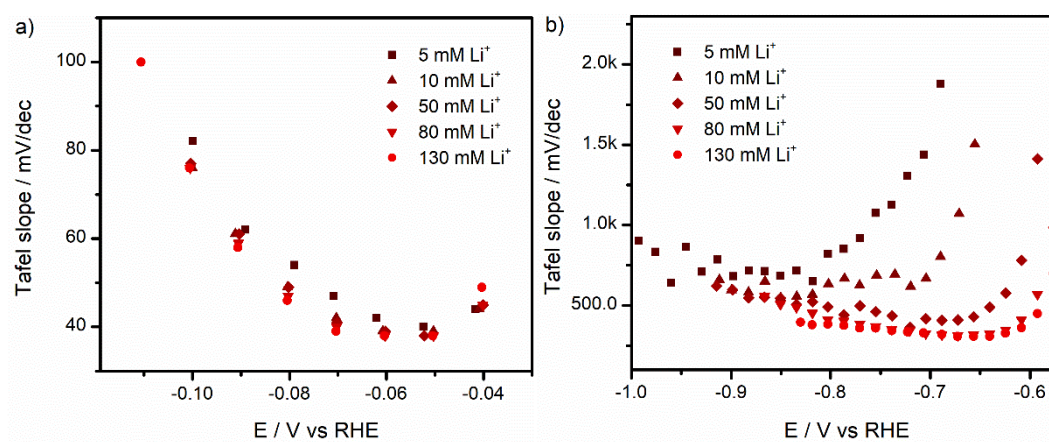


**Figure C.2** Tafel slope plots for a) proton reduction and b) water reduction reaction derived from the linear sweep voltammograms of Figure 4.1a.

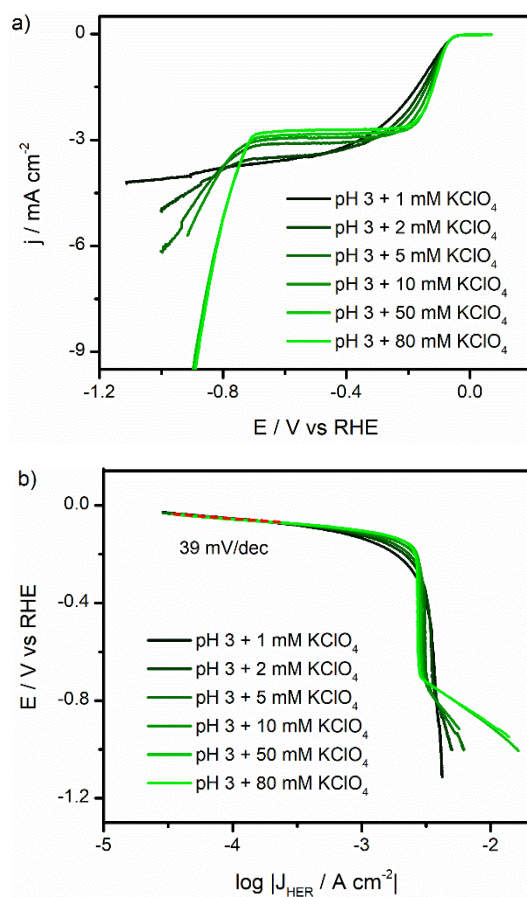


**Figure C.3** (a) Linear sweep voltammograms obtained for HER on Pt polycrystalline surface at 2400 rpm in pH 3 electrolytes with the presence of 1, 2, 5, 10, 50 and 80 mM  $\text{KClO}_4$ . The voltammograms were recorded at  $10 \text{ mV s}^{-1}$ . (b) Tafel slope analysis derived from the linear sweep voltammograms in (a), the range used for fitting is indicated in all plots with a dotted line in red.



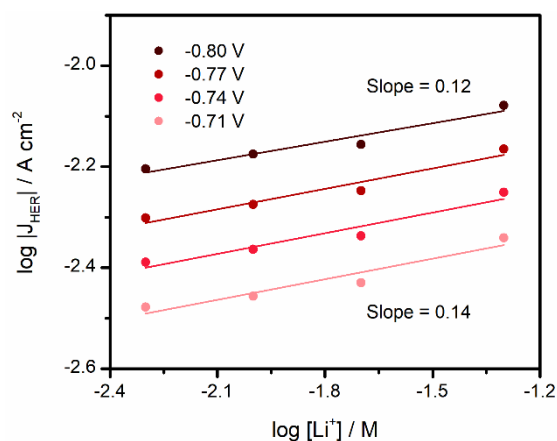


**Figure C.4** A cation concentration reaction order plot for HER on a polycrystalline Pt electrode at 2400 rpm in pH 3 + 80 mM  $\text{KClO}_4$  + x mM  $\text{LiClO}_4$ , at 30 mV potential steps (vs RHE) plotted as a function of the logarithm of the current density on the y-axis and logarithm of  $\text{Li}^+$  concentration on the x-axis. The corresponding slopes (reaction orders) at applied potentials of -0.80 V and -0.71 V (vs RHE) are respectively indicated next to the plots.

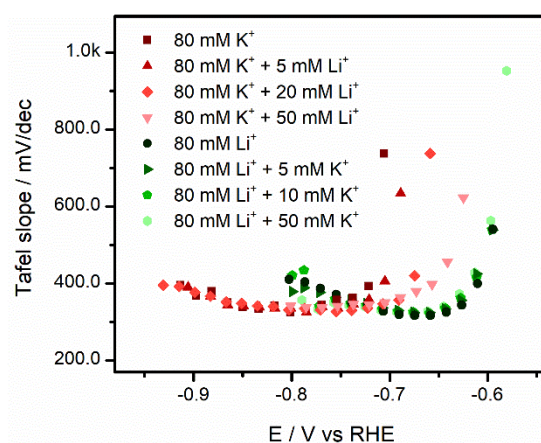


**Figure C.5** Tafel slopes for water reduction reaction on polycrystalline Pt in pH 3 electrolytes at a rotation rate of 2400 rpm at a scan rate of  $10 \text{ mV s}^{-1}$ .

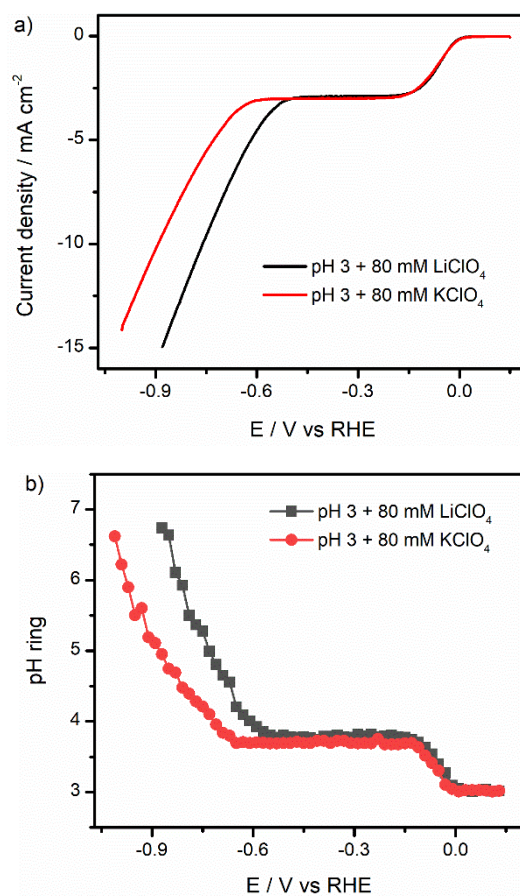


**Figure C.6** (a) Linear sweep voltammograms of the Pt disk electrode at 2400 rpm and 10 mV s<sup>-1</sup> in pH 3 electrolytes in the presence of 80 mM LiClO<sub>4</sub> and KClO<sub>4</sub> respectively. (b) The interfacial pH at the Au ring electrode during the linear sweep voltammetry on the Pt disk electrode.



# **D**

## **Supplementary Information for Chapter 5**

**Energy efficiency calculation:**

$$\varepsilon_{energy} = \frac{(E_{CO_2}^0 + E_{O_2}^0) * FE_{CO_2RR\ product}}{E_{cell}} \quad \text{Supplementary Equation 1}$$

Where  $E^0$  are the standard potentials of the cathode to desired products and anode reactions, FE is the current efficiency as percentage, and  $E_{cell}$  is the cell potential in V.

**Table D.1** Bulk pH of the electrolytes before the electrolysis (after CO<sub>2</sub> saturation), after 5h electrolysis (1 h electrolysis at a total current density of 10 mA cm<sup>-2</sup>, 1 h electrolysis at a total current density of 50 mA cm<sup>-2</sup>, 1 h electrolysis at a total current density of 75 mA cm<sup>-2</sup>, 1 h electrolysis at a total current density of 100 mA cm<sup>-2</sup> and 1 h electrolysis at a total current density of 150 mA cm<sup>-2</sup>), and after 20h electrolysis at a total applied current density of 200 mA cm<sup>-2</sup>.

Solutions	pH before electrolysis (after CO <sub>2</sub> saturation)	pH after 5h electrolysis	pH after 20h electrolysis
0.5 M KHCO <sub>3</sub>	7.23 <sup>1</sup>	7.47	7.8
pH 3+0.25 M K <sub>2</sub> SO <sub>4</sub>	3.01	2.96	2.46

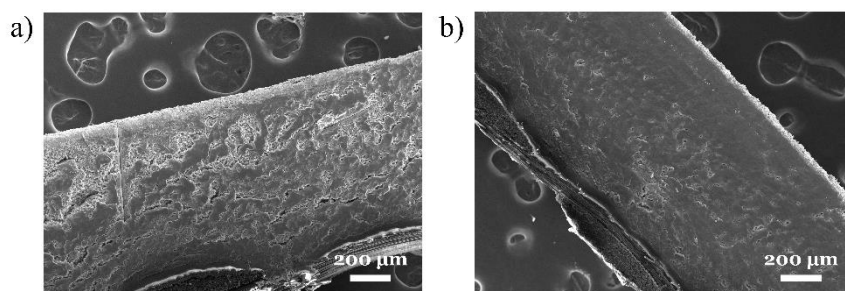


**Figure D.1** SEM images of cross sections of Copper GDE after 20 hours long term electrolysis at a total applied current density of  $200 \text{ mA cm}^{-2}$  in pH 3 electrolyte with presence of  $0.25\text{M K}_2\text{SO}_4$ .

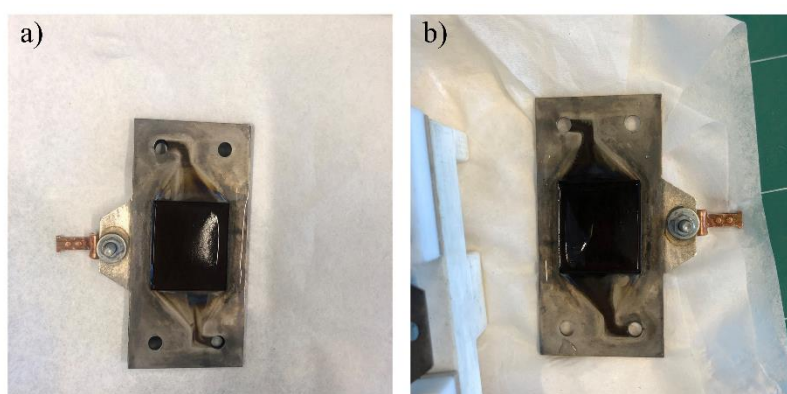


**Figure D.2** Images of copper GDEs after 20 hours long term electrolysis at a total applied current density of  $200 \text{ mA cm}^{-2}$  in a)  $0.5\text{M KHCO}_3$  and b) pH 3 electrolyte with presence of  $0.25\text{M K}_2\text{SO}_4$  respectively.

## Reference

1. Chen, C.; Zhang, B.; Zhong, J.; Cheng, Z., Selective electrochemical  $\text{CO}_2$  reduction over highly porous gold films. *Journal of Materials Chemistry A* **2017**, 5 (41), 21955-21964.



## Summary and Outlook

### Summary

Electrochemistry is a branch of chemistry focused on the interaction between electrical energy and chemical changes, playing a vital role in modern energy storage and conversion technologies. Since the early 21st century, it has gained substantial attention due to the growing concerns over climate change and the urgent need to transition away from fossil fuels. The increasing availability of low-cost electricity from renewable energy sources, such as solar and wind, has further underscored the need for efficient systems that can store and convert electrical energy into chemical bonds.

Over the past few decades, the electrochemical CO<sub>2</sub> reduction reaction (CO<sub>2</sub>RR) has been extensively studied for its potential to convert CO<sub>2</sub>, a major contributor to global warming, into valuable chemicals and fuels like formic acid, carbon monoxide, and hydrocarbons, using renewable energy. This process presents a promising solution for mitigating industrial CO<sub>2</sub> emissions while contributing to the global shift toward green energy and carbon neutrality. However, despite significant achievements made so far, CO<sub>2</sub>RR still faces significant challenges, including low activity and selectivity, catalyst degradation, and low overall energy efficiency, all of which limit its scalability for industrial applications.

This thesis will focus on these challenges and explores strategies to optimize CO<sub>2</sub>RR performance from different aspects. The first part (Chapter 2) investigates the influence of organic additives on CO<sub>2</sub>RR activity and selectivity, as well as their effects on the interfacial environment during CO<sub>2</sub>RR. The focus then shifts to a well-defined surface in Chapter 3, where we closely examine the role of metal cations on CO<sub>2</sub>RR using a palladium monolayer modified Pt(111) surface (Pd<sub>ML</sub>Pt(111)) in a pH 3 electrolyte. In Chapter 4, we further investigate the influence of metal cations on the competing hydrogen evolution reaction (HER) in mildly acidic media, which is relevant for optimizing CO<sub>2</sub>RR performance. Finally, in chapter 5, we expand the scope to industrially relevant conditions by studying the



influence of bulk electrolyte pH on CO<sub>2</sub>RR product distribution using a copper gas diffusion electrode (Cu GDE).

The thesis starts in chapter 2 with a study on CO<sub>2</sub>RR using poly(4-vinylpyridine) (P4VP) modified copper (Cu) and gold (Au) electrodes. We show that modifying Cu and Au electrodes with P4VP enhances formic acid formation during CO<sub>2</sub>RR, especially at low overpotentials. With in situ ATR-SEIRAS and contact angle measurements, we attribute the improved selectivity towards formic acid to the hydrophobic nature of the P4VP layer, which limits the transport of proton donors, i.e. bicarbonate (HCO<sub>3</sub><sup>-</sup>) and water, from the bulk electrolyte to the reaction interface, effectively suppressing HER.

Chapter 3 investigates the influence of cations on formic acid and CO formation during CO<sub>2</sub>RR using a palladium monolayer modified platinum (Pd<sub>ML</sub>Pt(111)) electrode. We observe that the onset potentials for formic acid and CO formation shift positively with increasing cations concentration, with a pronounced effect on formic acid formation. Theoretical simulations suggest that cations facilitate both hydride formation and CO<sub>2</sub> activation by polarizing the electronic density at the surface and stabilizing \*CO<sub>2</sub><sup>-</sup>. In addition, the simulations indicate that high CO coverage inhibits hydride formation, leading to a rapid decrease of formic acid selectivity at higher applied potentials.

In Chapter 4, we study the role of metal cations in the HER on a polycrystalline platinum electrode in mildly acidic media. We show that increasing cation concentration significantly enhances water reduction but does not kinetically influence proton reduction at lower potentials. In addition, we identify a non-negligible migration current under mass transport limited conditions in electrolytes with low cation concentration, highlighting the importance of sufficient supporting electrolyte in minimizing this migration current. We further show that, adding strongly hydrated cations, e.g. Li<sup>+</sup>, to a K<sup>+</sup> containing electrolyte, shifts the onset potential for water reduction positively, suggesting that strongly hydrated cations (Li<sup>+</sup>) promote water dissociation more effectively compared to weakly hydrated cations (K<sup>+</sup>).

In Chapter 5, we investigate the effect of bulk electrolyte pH on CO<sub>2</sub>RR product distribution using Cu GDE. We show an inhibited hydrogen formation at low current densities in a mildly acidic electrolyte compared with a traditional bicarbonate electrolyte, and similar CO<sub>2</sub>RR product distributions in both electrolytes at higher current densities. Additionally, we highlight that, despite the promising prospects of acidic media for CO<sub>2</sub>RR, electrode degradation remains a challenge for long-term electrolysis, particularly in acidic bulk electrolytes.

## **Outlook**

The future of electrochemical CO<sub>2</sub> reduction lies in overcoming key challenges such as improving selectivity, enhancing catalyst stability, and ensuring scalability for industrial applications. Significant progress has been made in catalyst design, particularly through nanostructuring and the use of organic additives, which have shown potential in improving reaction efficiency. In addition, optimizing the electrolyte composition and engineering the reaction environment at the electrode-electrolyte interface are critical to improving CO<sub>2</sub>RR performance. The development of more robust electrolyzer systems, such as GDE systems, is another essential aspect for practical implementation of CO<sub>2</sub>RR technologies. Despite the considerable achievements thus far, continued research into reaction mechanisms and electrode-electrolyte engineering as well as electrolyzer system engineering will be necessary to unlock the full potential of CO<sub>2</sub>RR in industrial applications.

## **Samenvatting en vooruitzicht**

### **Samenvatting**

Elektrochemie is een tak van de scheikunde die zich richt op de interactie tussen elektrische energie en chemische veranderingen, en speelt een cruciale rol in moderne technologieën voor energieopslag en -omzetting. Sinds het begin van de 21e eeuw heeft het veel aandacht gekregen vanwege de toenemende zorgen over klimaatverandering en de dringende noodzaak om over te schakelen van fossiele brandstoffen. De toenemende beschikbaarheid van goedkope elektriciteit uit hernieuwbare energiebronnen, zoals zon en wind, heeft de noodzaak verder onderstreept voor efficiënte systemen die elektrische energie kunnen opslaan en omzetten in chemische bindingen.

De afgelopen decennia is de elektrochemische CO<sub>2</sub>-reductiereactie (CO<sub>2</sub>RR) uitgebreid bestudeerd vanwege het potentieel om CO<sub>2</sub>, een belangrijke veroorzaker van de opwarming van de aarde, om te zetten in waardevolle chemicaliën en brandstoffen zoals mierenzuur, koolmonoxide en koolwaterstoffen met behulp van hernieuwbare energie. Dit proces biedt een veelbelovende oplossing om industriële CO<sub>2</sub>-emissies te verminderen en tegelijkertijd bij te dragen aan de wereldwijde overgang naar groene energie en koolstofneutraliteit. Echter, ondanks de aanzienlijke vooruitgang, ondervindt CO<sub>2</sub>RR nog steeds belangrijke uitdagingen, zoals lage activiteit en selectiviteit, katalysatordegradatie en een lage energie-efficiëntie, die de schaalbaarheid voor industriële toepassingen beperken.

Dit proefschrift richt zich op deze uitdagingen en verkent strategieën om de prestaties van CO<sub>2</sub>RR te optimaliseren vanuit verschillende invalshoeken. Het eerste deel (Hoofdstuk 2) onderzoekt de invloed van organische additieven op de CO<sub>2</sub>RR-activiteit en -selectiviteit, evenals hun effecten op de grensvlakomgeving tijdens CO<sub>2</sub>RR. Vervolgens verschuift de focus in Hoofdstuk 3 naar een goed gedefinieerd oppervlak, waar we de rol van metaalkationen op CO<sub>2</sub>RR nauwkeurig onderzoeken met behulp van een palladium-monolaag-gemodificeerd Pt(111)-oppervlak (Pd<sub>ML</sub>Pt(111)) in een pH 3-elektrolyt. In

Hoofdstuk 4 onderzoeken we verder de invloed van metaalkationen op de concurrerende waterstofevolutiereactie (HER) in licht zure media, wat relevant is voor het optimaliseren van de CO<sub>2</sub>RR-prestaties. Tot slot breiden we in Hoofdstuk 5 de studie uit naar industrieel relevante omstandigheden door de invloed van de bulk-elektrolyt pH op de CO<sub>2</sub>RR-productverdeling te bestuderen met behulp van een koper gasdiffusie-elektrode (Cu GDE).

Het proefschrift begint in Hoofdstuk 2 met een studie naar CO<sub>2</sub>RR met behulp van poly(4-vinylpyridine) (P4VP) gemodificeerde koper (Cu) en goud (Au) elektroden. We tonen aan dat de modificatie van Cu en Au elektroden met P4VP de vorming van mierenzuur tijdens CO<sub>2</sub>RR verbetert, vooral bij lage overpotentialen. Met behulp van in situ ATR-SEIRAS en contacthoekmetingen schrijven we de verbeterde selectiviteit voor mierenzuur toe aan de hydrofobe aard van de P4VP-laag, die het transport van protondonoren, d.w.z. bicarbonaat (HCO<sub>3</sub><sup>-</sup>) en water, van de bulk elektrolyt naar het reactiegrensvlak beperkt, waardoor HER effectief wordt onderdrukt.

Hoofdstuk 3 onderzoekt de invloed van kationen op de vorming van mierenzuur en CO tijdens CO<sub>2</sub>RR met behulp van een palladium-monolaag-gemodificeerde platina (PdMLPt(111)) elektrode. We observeren dat de aanvangspotentialen voor de vorming van mierenzuur en CO positief verschuiven met toenemende kationconcentraties, met een uitgesproken effect op de vorming van mierenzuur. Theoretische simulaties suggereren dat kationen zowel de vorming van hydride als de activering van CO<sub>2</sub> vergemakkelijken door de elektronische dichtheid aan het oppervlak te polariseren en \*CO<sub>2</sub><sup>-</sup> te stabiliseren. Bovendien geven de simulaties aan dat een hoge CO-bedekking de vorming van hydride remt, wat leidt tot een snelle afname van de selectiviteit voor mierenzuur bij hogere toegepaste potentialen.

In Hoofdstuk 4 bestuderen we de rol van metaalkationen in de HER op een polykristallijne platina-elektrode in licht zure media. We tonen aan dat toenemende kationconcentraties de waterreductie significant verbeteren, maar de protonreductie bij lagere potentialen niet kinetisch beïnvloeden. Daarnaast identificeren we een niet-verwaarloosbare migratiestroom onder massatransport-beperkte omstandigheden in elektrolyten met een lage kationconcentratie, wat het belang van voldoende ondersteunende elektrolyten benadrukt om

deze migratiestroom te minimaliseren. We laten verder zien dat het toevoegen van sterk gehydrateerde kationen, zoals  $\text{Li}^+$ , aan een  $\text{K}^+$ -bevattend elektrolyt de aanvangspotentiaal voor waterreductie positief verschuift, wat suggereert dat sterk gehydrateerde kationen ( $\text{Li}^+$ ) de waterdissociatie effectiever bevorderen dan zwak gehydrateerde kationen ( $\text{K}^+$ ).

In Hoofdstuk 5 onderzoeken we het effect van de bulk-elektrolyt pH op de  $\text{CO}_2\text{RR}$ -productverdeling met behulp van Cu GDE. We tonen aan dat de vorming van waterstof wordt geremd bij lage stroomdichtheden in een licht zuur elektrolyt vergeleken met een traditioneel bicarbonaat-elektrolyt, en dat de  $\text{CO}_2\text{RR}$ -productverdeling in beide elektrolyten vergelijkbaar is bij hogere stroomdichtheden. Bovendien benadrukken we dat, ondanks de veelbelovende vooruitzichten van zure media voor  $\text{CO}_2\text{RR}$ , de degradatie van de elektrode een uitdaging blijft bij langdurige elektrolyse, vooral in zure bulk-elektrolyten.

## **Vooruitzicht**

De toekomst van elektrochemische  $\text{CO}_2$ -reductie ligt in het overwinnen van belangrijke uitdagingen, zoals het verbeteren van de selectiviteit, het vergroten van de stabiliteit van de katalysator en het waarborgen van de schaalbaarheid voor industriële toepassingen. Er zijn al aanzienlijke vorderingen gemaakt in het ontwerp van katalysatoren, met name door nanostructurering en het gebruik van organische additieven, die potentieel hebben getoond in het verbeteren van de reactiesnelheid. Daarnaast is het optimaliseren van de samenstelling van het elektrolyt en het ontwerpen van de reactieomgeving op het elektrode-elektrolytgrensvlak van cruciaal belang voor het verbeteren van de  $\text{CO}_2\text{RR}$ -prestaties. De ontwikkeling van robuustere elektrolyse systemen, zoals GDE-systemen, is een ander essentieel aspect voor de praktische implementatie van  $\text{CO}_2\text{RR}$ -technologieën. Ondanks de aanzienlijke prestaties tot nu toe, blijft voortgezet onderzoek naar reactiemechanismen, elektrode-elektrolyt engineering en de ontwikkeling van stabiele elektrolyse systemen noodzakelijk om het volledige potentieel van  $\text{CO}_2\text{RR}$  voor industriële toepassingen te benutten.

## List of Publications

**This thesis is based on these publications:**

### Chapter 2

**Ye, C.**; Raaijman, S. J.; Chen, X.; Koper, M. T. M.

Enhanced Electrochemical CO<sub>2</sub> Reduction to Formate on Poly(4-vinylpyridine)-modified Copper and Gold Electrodes

*ACS Appl. Mater. Interfaces* **2022**, 14 (40), 45263-45271

### Chapter 3

**Ye, C.**; **Dattila, F.**; Chen, X.; Lopez, N.; Koper, M. T. M.

(Both authors contributed equally)

Influence of Cations on HCOOH and CO Formation during CO<sub>2</sub> Reduction on a Pd<sub>ML</sub>Pt(111) Electrode

*J. Am. Chem. Soc.* **2023**, 145 (36), 19601-19610

### Chapter 4

**Ye, C.**; Liu, X.; Koper, M. T. M.

The Role of Cations in Hydrogen Evolution Reaction on a Platinum Electrode in Mildly Acidic Media

*Electrochem. Commun.* **2024**, 166, 107784

### Other publications:

Phan, T. H.; Banjac, K.; Cometto, F. P.; Dattila, F.; García-Muelas, R.; Raaijman, S. J.; **Ye, C.**; Koper, M. T. M.; López, N.; Lingenfelder, M.

Emergence of Potential-Controlled Cu-Nanocuboids and Graphene-Covered Cu-Nanocuboids under *Operando* CO<sub>2</sub> Electroreduction

*Nano Lett.*, **2021**, 21(5), 2059-2065

Hersbach, T. J. P.; **Ye, C.**; Garcia, A. C.; Koper, M. T. M.

Tailoring the electrocatalytic activity and selectivity of Pt(111) through cathodic corrosion

*ACS Catal.* **2020**, 10 (24), 15104-15113

**Ye, C.**; Huang, H.; Zeng, J.

Precisely Controlled Synthesis of Pt-Pd Octahedral Nanoframes as a Superior Catalyst towards Oxygen Reduction Reaction.

*Chinese J Chem Phys.* **2017**, 30, 581

**Ye, C.**, Li, K., Huang, H.; Zeng, J.

Preparation and Application of Ultrathin PtRh Nanowires.

CN106925771A, **2017** (Chinese Patent)

**Ye C.**; Li X.; Huang, H.; Zeng, J.

Preparation and Application of Pd@PdFe Icosahedral Nanocrystals

CN106876732A, **2017** (Chinese patent)

## Curriculum vitae

Chunmiao Ye was born on December 18th, 1992, in Anhui, China. She attended Maotanchang High School from 2008 to 2010. In 2010, she enrolled at the University of Science and Technology of China (USTC) to pursue a Bachelor's degree in Materials Chemistry, graduating in June 2014. Chunmiao continued her academic journey at USTC, where she completed her Master's degree in Chemical Physics in July 2017. Her master's research focused on designing nanostructures with high surface atom exposure for electrocatalytic applications.

In October 2017, Chunmiao began her PhD at Leiden University under the supervision of Prof. Dr. Marc Koper. Her PhD project was part of the Marie Curie ITN ELCOREL, which included collaborations with seven partner institutions, fostering a dynamic and interdisciplinary research environment. Her research primarily investigated the factors affecting the activity and selectivity of the electrochemical CO<sub>2</sub> reduction reaction. Additionally, she had the opportunity to work on large-scale CO<sub>2</sub> electrolysis systems during her time as a visiting researcher at Avantium, a chemical technology company specializing in renewable chemistry solutions, based in Amsterdam. There, she was supervised by Dr. Klaas Jan Schouten and Matthew Philips. The results of Chunmiao's research are presented in this thesis, and parts of her work have been showcased at several national and international conferences. During her PhD, she also contributed to teaching "Organic Chemistry" practical courses.

In 2022, Chunmiao joined Dompotent von Kreisler as a trainee patent attorney. She is currently exploring the field of intellectual property and pursuing her qualification as a European patent attorney.

## Acknowledgements

Completing this PhD journey has been a challenging yet profoundly rewarding experience. I am sincerely grateful to all the people who have guided, supported and accompanied me throughout this remarkable journey.

First and foremost, I would like to express my deepest gratitude to my supervisor, Prof. Dr. Marc Koper for giving me the opportunity to pursue my PhD in Catalysis and Surface Chemistry group in Leiden University. Your expert guidance, insightful advice, and passion for fundamental research kept me motivated and drove me forward. Reflecting on the phrase “broad my horizons”, which I included in my initial motivation letter, I now really appreciate the depth and significance of those words.

I am also deeply thankful to my wonderful friends and colleagues in CASC and the Marie Curie ITN ELCOREL program who contributed to the realization of this thesis. Special thanks to Dr. Stefan Raaijman for teaching me laboratory skills and critical feedback on my papers, Dr. Xiaoting Chen for guiding me into the magic world of single crystals, Dr. Federico Dattila for showing me the fantastic (and puzzling) computational modelling and insights into the PdML project, Dr. Klaas Jan Schouten and Matthew Philips for welcoming me to Avantium and allowing me to explore large-scale CO<sub>2</sub> electrolysis systems during my research stay in Amsterdam, Dr. Giulia Marcandalli and Dr. Matias Villalba for your assistance with ATR-SEIRAS experiments, Xuan Liu for your support with RRDE experiments, Dr. Akansha Goyal and Linfan Shen for refreshing my understanding of HER and CO<sub>2</sub>RR, Rafaël Vos, Onno van der Heijden, Dr. Alisson da Silva, Dr. Mingchuan Luo, Dr. Kasinath Ojha, Dr. David Pavesi, Dr. Amanda Garcia, Dr. Diana Aranzales and all others for the joyful and “productive” hours we shared in the lab.

I would like to thank all my friends for sharing my wonderful PhD journey: Chen, Chengyu, Diyu, Shengxiang, Weizhe, Xuequan, Ye, Yurong, Wanbin, Feng, Yingguang, Stefan, Xiaoting, Professor Fu, Giulia, Matias, Akansha, Xuan, Linfan, Amanda, Diana and all others, for having all the non-sense discussions, all the amazing things we tried together, all the highs, frustrations and every memorable moment—you have all helped me shape me into the person I am today.

Last but not least, I would like to express my deepest gratitude to my family. Special thanks to my cousin Peipei and brother Yixian for the love, care and dedication you have shown to our family. As an older sister, I’m incredibly proud of the individuals you have both become, and I am deeply honored to be part of your journey.



